arXiv:1602.00584v1 [cond-mat.str-el] 1 Feb 2016

Dynamical screening in correlated electron systems – from lattice models to realistic materials

Philipp Werner[1] and Michele Casula[2]

[1]*Department of Physics, University of Fribourg, Chemin du Musée 3, 1700 Fribourg, Switzerland*

[2]*CNRS and Institut de Minéralogie, de Physique des Matériaux et de Cosmochimie, Université Pierre et Marie Curie, 4 place Jussieu, 75252 Paris, France*

(Dated: January 30, 2016)

Abstract

Recent progress in treating the dynamically screened nature of the Coulomb interaction in strongly correlated lattice models and materials is reviewed with a focus on computational schemes based on the dynamical mean field approximation. We discuss approximate and exact methods for the solution of impurity models with retarded interactions, and explain how these models appear as auxiliary problems in various extensions of the dynamical mean field formalism. The current state of the field is illustrated with results from recent applications of these schemes to U-V Hubbard models and correlated materials.

PACS numbers: 71.10.Fd

Contents

I. Introduction 4

II. Downfolding 8

III. Solving low-energy models with dynamically screened $U(\omega)$ 16

A. Dynamical mean field theory 16

1. DMFT approximation 18

2. DMFT self-consistency loop 18

B. Holstein-Hubbard model 19

1. DALA approach 22

2. Lang-Firsov approach 23

3. Continuous-time Monte Carlo approach 26

4. Phase diagram 30

C. General $U(\omega)$ 31

D. Effective static model 34

E. Multiorbital systems 35

IV. Towards a self-consistent description of screening 37

A. U-V Hubbard model 38

1. Extended DMFT 38

2. GW+DMFT 41

3. Dual boson 45

B. Realistic materials 47

1. GW+DMFT 47

2. Frozen polarization: $\mathcal{U}$ replaced by the cRPA $U(\omega)$ 49

3. SEX+DMFT 50

4. DMFT@nonlocal-GW 52

5. QSGW+DMFT 53

6. Concluding remarks on simplified GW+DMFT approaches 54

V. Analytical continuation 54

A. Fermionic spectral function 55

B. Bosonic spectral function 57

VI. Applications to model systems 58

A. Extended DMFT 58

1. U-V Hubbard model 58

2. Dynamical screening in photo-doped Mott insulators 61

B. GW+DMFT 62

1. U-V Hubbard model 62

2. Adatom systems on semiconductor surfaces 65

VII. Applications to realistic materials 67

A. LDA+DMFT+$U(\omega)$ 67

1. Mass enhancement and satellites in $SrVO_3$ 67

2. Spin-freezing crossover in hole-doped $BaFe_2As_2$ 69

3. Mott gap and -13 eV satellite in La_2CuO_4 72

B. SEX+DMFT results for $BaCo_2As_2$ 73

C. GW+DMFT results for $SrVO_3$ 76

1. Band widening from k-dependent Σ 76

2. Self-consistent calculation of Σ 80

VIII. Conclusions and Outlook 81

Acknowledgements 84

References 84

I. INTRODUCTION

Screening describes the way the electrons rearrange themselves to reduce the inter-particle interaction and total energy of the system, while correlation describes how the electrons move collectively in the system. Both concepts are closely related and connected. In Hartree-Fock theory, the electrons are not correlated except for like-spin particles, which are constrained by the Pauli exclusion principle. A consistent framework to improve upon this theory was proposed by Hedin in his seminal 1965 paper [1]. He expanded the self-energy up to the first-order in the dynamically screened interaction W, and thereby laid the foundation of the GW theory [2–4]. The screened interaction W is the bare interaction reduced by the dielectric function, determined by the charge-charge response function, which in turn is sensitive to electronic correlations. Screening is thus a dynamical process, as it depends on how the electrons respond to a given perturbation. It is obviously sensitive to the nature of the underlying electronic states. One of the fingerprints of screening are the plasmon satellites, collective excitations associated with long-range charge fluctuations, which are seen in electron spectroscopy (such as, for instance, photoelectron spectroscopy (PES) [5] and electron energy loss spectroscopy (EELS) [6]).

In correlated electron systems, where local atomic-like interactions are dominant, screening is also crucial to set the actual value of the Coulomb repulsion, and thus to determine the level of correlation in the system. Describing within the same framework both the long-range nature of screening and its role in tuning the local repulsion U has been a long-standing theoretical challenge. The GW approximation, while neglecting vertex corrections, takes into account reasonably well dynamical long-range screening effects [7, 8], but it usually fails for large and local Coulomb repulsions, which are better described within a Hubbard model. This pushed Hedin to write in his review [3]: "Clearly, the GW approximation describing long-range charge fluctuations, and a Hubbard model focusing on local on-site correlations, are two extremes."

These two extremes can now be merged into a coherent and unified picture, thanks to recent progress in Green's function embedding schemes, which have been developed as extended dynamical mean field theories. In dynamical mean field theory (DMFT) the correspondence between the local lattice Green's function $G_{\rm loc}$ and the solution of an auxiliary Anderson impurity problem is realized through the dynamical Weiss field $\mathcal{G}_0$, which mimics

the effect of the lattice environment on the impurity site. In extended dynamical mean field theory (EDMFT), the embedding is extended to the local screened interaction $W_{\rm loc}$ which matches the impurity screened interaction and determines the dynamical bosonic field $\mathcal{U}$, which represents the effect of non-local interactions on the auxiliary Anderson problem. Thus, the EDMFT embedding procedure maps non-local interaction effects onto a local dynamical screening, and allows to treat these local interactions in a non-perturbative way. Indeed, since the advent of continuous time quantum Monte Carlo (CTQMC) algorithms [9], solving the Anderson impurity problem with retarded - aka frequency dependent - interactions has become feasible. This has been a major advance in the field. However, in the EDMFT framework the resulting self-energy is still local.

A further step forward is represented by the GW+DMFT theory, proposed in 2003 by Biermann and coworkers [10], where the embedding is performed at the Green's function level between the local self-energy coming from the EDMFT solution of the impurity problem and the non-local self-energy, taken from GW. Therefore, non-locality is included at the GW level, and the method can be applied to study first-principles Hamiltonians. Different schemes along these lines have become popular also in other contexts, such as in quantum chemistry [11–13], where the quantum system is divided into two parts, one of which is treated at the perturbative level, e. g. by the self-consistent second-order Green's function method (GF2), while the other is solved at a higher level by the configuration interaction (CI) method [14, 15]. However, what distinguishes GW+DMFT from other approaches is the *double* embedding in both the Green's function G and the dynamically screened interaction W. This has many advantages, as we will see in this review; one of the most important is that it promotes the Hubbard U parameter to the Weiss field $\mathcal{U}$, which is determined self-consistently. Therefore, the underlying Hubbard Hamiltonian with retarded interactions is no longer a model, but is an auxiliary system, making the GW+DMFT scheme a truly *ab initio* approach. At the same time, non-locality is kept in both the self-energy Σ and the electronic polarization P, which are related to G and W, respectively. The GW+DMFT self-consistency in $G_{\rm loc}$ and $W_{\rm loc}$ closes the gap between the two extremes quoted by Hedin.

The general framework sketched above is conceptually appealing but still far from being a black-box machinery capable of solving generic correlated electron systems and first-principles Hamiltonians. However, in the last few years, significant progress has been made toward the final goal of a self-consistent description of dynamical screening effects in strongly

correlated materials. In this review, we are going to introduce the theoretical and numerical tools which made this progress possible, such as, for instance, the CTQMC algorithm for frequency dependent interactions. Moreover, we are going to present the latest applications, both at the model level and from first principles. Model applications are useful to understand the limitations of the approximations underlying the EDMFT or GW+DMFT approaches, while the latest applications to real materials are extremely interesting, as they suggest new promising directions to approximate GW+DMFT schemes, which are computationally more affordable, and can be applied to a wider class of *ab initio* systems.

In our review we will not only explain the general theory, but also focus on practical aspects, with a twofold purpose: First, making tighter theoretical connections between various methods which deal with dynamical screening in *ab initio* correlated electron systems. Second, presenting methodological details, which help the reader implement the methods in a computer program. Throughout the review, we will use eV as energy units in the *ab initio* applications, while the energy units will be set to the bandwidth, or some related hopping scale, in model applications.

The general organization of this review is as follows. In Sec. II we explain how the screening is modeled from first principles in strongly correlated materials. We show that the retarded interactions emerge naturally from a multi-scale approach, where the coupling parameters are dynamically screened by higher-energy degrees of freedom, which are traced out in the derivation of the low-energy Hamiltonian.

In Sec. III, we introduce the main theoretical framework used throughout this review (Sec. III A), namely the DMFT, employed to solve Hubbard-like low-energy Hamiltonians with retarded local interactions U. We describe several solvers capable of tackling the Anderson impurity problem with frequency dependent U, with a particular emphasis on the CTQMC method (Sec. III B 3), which is formally exact and efficient in the case of density-density interactions. Different approximations are proposed for solving the impurity problem, such as the dynamic atomic-limit approximation (DALA) in Sec. III B 1 and the Lang-Firsov approach in Sec. III B 2. These methods are explained first for the solution of the Holstein-Hubbard model (Sec. III B), where the dynamic nature of the local interaction U derives from bosons (plasmons), locally coupled to the correlated electrons. This formalism can be generalized to deal with arbitrary *ab initio* $U(\omega)$ (Sec. III C) and with multi-band/multi-orbital systems typical of realistic materials (Sec. III E), thanks to the

mapping to a continuum of bosonic modes. The physics behind the generalized Holstein-Hubbard model can be made more transparent by the derivation of an effective static model, with renormalized hoppings and interactions due to screening effects, detailed in Sec. III D.

With the tools of Sec. III, one would like to go beyond the local interaction picture, which could be too rough for realistic materials. Dealing with non-local interactions is a prerequisite for treating long-range screening effects, which lead to collective phenomena in solids. In Sec. IV, we present different strategies for treating long-range interactions in strongly correlated systems, both for extended U-V Hubbard models (Sec. IV A) and realistic materials (Sec. IV B). Thse approaches are based on the Green's function embedding theory, where both the local Green's function and the local screened interaction are self-consistently determined by the many-body solution of an auxiliary single-impurity problem, which provides both the local electronic self-energy and local polarization of the physical system. In this way, non-local interactions give rise to additional local screening for the impurity problem with dynamic $\mathcal{U}$. The Green's function embedding can be done at the extended-DMFT level (Sec. IV A 1), or at the GW+DMFT level (Sec. IV A 2). In the latter scheme, the non-local self-energies and non-local polarizations, computed within the GW approximation, are self-consistently added to the corresponding local quantities, evaluated in a non-perturbative way at the DMFT level. Additional approximations are necessary to apply the GW+DMFT framework to realistic materials (Sec. IV B 1), due to the large number of degrees of freedom of *ab initio* Hamiltonians. These approximate schemes are still under active development. In this review, we report the frozen cRPA polarization (Sec. IV B 2), the SEX+DMFT (Sec. IV B 3), and DMFT schemes bases on effective Hamiltonians renormalized by the non-local GW self-energy, such as the DMFT@nonlocal-GW (Sec. IV B 4) and the quasi-particle self-consistent GW (QSGW) + DMFT (Sec. IV B 5). On the model side, we briefly introduce the recently developed dual boson approach in Sec. IV A 3.

As the CTQMC impurity solver works in imaginary time, an analytic continuation to real frequencies is necessary to obtain spectral functions which can be compared to experiment. One needs to take particular care in the case of retarded interactions, in order to resolve features such as satellites arising from screening plasmons. A detailed procedure to incorporate these high-energy structures is explained in Sec. V A for the fermionic spectral function. The properly normalized kernel for the bosonic spectral functions is derived in Sec. V B.

Applications to both model systems and realistic materials are presented in Secs. VI and VII, respectively. On the model side, the U-V Hubbard Hamiltonian (Secs. VI A 1 and VI B 1), photo-doped Mott insulators (Sec. VI A 2), and adatom systems on semi-conductor surfaces (Sec. VI B 2) are discussed. On the *ab initio* side, we present results for the $SrVO_3$ transition metal oxide (Secs. VII A 1 and VII C), for the $BaFe_2As_2$ (Sec. VII A 2) and $BaCo_2As_2$ (Sec. VII B) pnictides, and for the La_2CuO_4 cuprate (Sec. VII A 3).

Conclusions and perspectives are drawn in Sec. VIII.

II. DOWNFOLDING

Computational methods play an important role in the study of strongly correlated systems. Many interesting materials, such as the high-T_c cuprates, have been studied in great detail using a broad range of experimental probes, which results in a detailed quantitative knowledge of the correlated electronic structure. A good theoretical description should be consistent with these experimental findings, and provide insights into the underlying physical mechanism. Ideally, the accuracy of the computational approach will enable quantitative predictions of material properties. However, even the simplest model used to investigate the physics of the cuprates, the two-dimensional (2D) single-band Hubbard model, does not admit a closed-form solution in the most interesting parameter regimes, which are relevant for the experimental situations. For instance, the solution of this model near the Mott transition can be obtained in an approximate yet accurate way only if the most advanced numerical techniques are employed [16–24].

Moreover, the complexity and richness of strongly correlated materials puts limitations on the predictive power of simple models. The link between the model parameters and the experimental conditions, such as doping, pressure, chemical substitution, and temperature, may be difficult to establish. Yet, the validity of a theory is based on its ability to explain unambiguously and quantitatively a variety of situations. Therefore, a systematic procedure for the derivation of the model parameters is essential. Numerical approaches play a crucial role in the calculation of model parameters, which are seamlessly connected to the physics of actual compounds.

The idea is to use a multi-scale *ab initio* scheme [25, 26], which is able to treat and predict material properties at a level of accuracy depending on the target energy. The

common scheme is to first compute the *full* band structure by density functional theory (DFT) [27–29], which takes into account electrons ranging from the deepest core levels to the virtual empty states, and covers an energy range of several tens or hundreds of eV. As it is well know, DFT is not the most accurate theory for strongly correlated materials, but it is able to reproduce general trends starting from the first-principle Hamiltonian, including several degrees of freedom. Its failure is usually related to the description of low-energy states, i.e. the ones near the Fermi level. In the case of strong correlations, they are poorly described by most of the functionals. At the same time, these states are primarily responsible for a material's macroscopic properties. Thus, we would like to improve upon the DFT description, by applying more accurate, but computationally heavier, many-body methods to this low-energy sector. In order to do this, we need to derive a low-energy model by integrating out the high-energy degrees of freedom from the DFT solution. This intermediate, crucial step, is called *downfolding*. The last step is the solution of the resulting model using advanced and hopefully accurate many-body techniques.

In order to *downfold* the DFT Hamiltonian, one needs to find a basis set which spans the low-energy space. Usually, one takes the maximally localized Wannier functions, $\phi_{m\mathbf{R}}$ for the m-th orbital centered in the unit cell $\mathbf{R}$, which give a reliable representation of the correlated orbitals and their low-energy bands [30, 31]. Then, one projects the *ab initio* Hamiltonian onto the basis set elements. The Coulomb matrix elements, which define the bare U, are therefore

$$U^{\text{bare}}_{mn}(\mathbf{R}) = \langle \phi_{m\mathbf{0}} \phi_{n\mathbf{R}} | v | \phi_{m\mathbf{0}} \phi_{n\mathbf{R}} \rangle = \int d\mathbf{r}\; d\mathbf{r}' \frac{|\phi_{m\mathbf{0}}(\mathbf{r})|^2 |\phi_{n\mathbf{R}}(\mathbf{r}')|^2}{|\mathbf{r} - \mathbf{r}'|}, \tag{1}$$

where v is the Coulomb potential. Without loss of generality, we restrict our discussion here to interactions of density-density form.

The above expression neglects the fundamental effect of screening from high-energy electrons on the low-energy manifold. In the random phase approximation (RPA) framework, the fully screened interaction is given by $W = v/(1 - vP)$, where P is the polarization function, defined as $P(\mathbf{r}, \mathbf{r}', t) = -2iG_0(\mathbf{r}, \mathbf{r}', t)G_0(\mathbf{r}', \mathbf{r}, -t)$. In the latter definition, the factor of 2 comes from the spin summation in the spin-degenerate case, and G_0 is the zero temperature DFT Green's function, which reads:

$$G_0(\mathbf{r}, \mathbf{r}', t) = \begin{cases} i \sum_l^{\text{occ}} \Psi_l(\mathbf{r}) \Psi_l^*(\mathbf{r}') e^{-i\epsilon_l t}, & \text{if } t < 0 \\ -i \sum_l^{\text{unocc}} \Psi_l(\mathbf{r}) \Psi_l^*(\mathbf{r}') e^{-i\epsilon_l t}, & \text{if } t > 0 \end{cases} \tag{2}$$

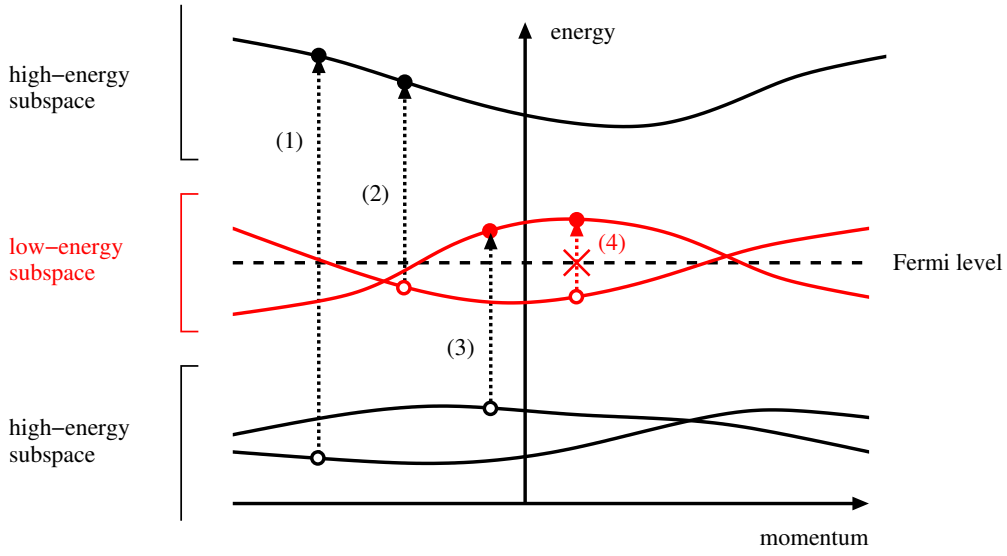


FIG. 1: Schematic illustration of the screening processes in the constrained RPA framework. The black bands are the so-called "screening bands", while the red bands are assumed to be strongly correlated. Only the transitions within the low-energy subspace (excitations of type (4)) contribute to the low-energy polarization P^L, while the "complement" P^H includes excitations of type (1), (2), and (3), i.e., excitations involving the high-energy bands.

where the $\{\psi_l, \epsilon_l\}$ are the one-particle Bloch eigenfunctions and eigenvalues corresponding to the system's band structure. In the frequency domain, and for temperature $T = 0$, the above expression for the polarization becomes

$$P(\mathbf{r}, \mathbf{r}', \omega) = 2 \sum_{i}^{\text{occ}} \sum_{j}^{\text{unocc}} \psi_i(\mathbf{r}) \psi_i^*(\mathbf{r}') \psi_j^*(\mathbf{r}) \psi_j(\mathbf{r}') \left\{ \frac{1}{\omega - \epsilon_j + \epsilon_i + i0^+} - \frac{1}{\omega + \epsilon_j - \epsilon_i - i0^+} \right\}. \tag{3}$$

One can then separate P into the two contributions $P = P^H + P^L$, with P^L defined by polarization channels fully contained in the low-energy (L) window around the Fermi level, and P^H its complement. Note that P^H includes not only particle-hole excitations within the high-energy (H) sector, but also those connecting the high- and the low-energy sector. A schematic illustration of the division between P^H and P^L is reported in Fig. 1.

In the constrained RPA (cRPA) theory [32, 33], the *partially screened* interaction is given by $W^L = v/(1-vP^H)$. The physical interpretation is transparent: W^L is the bare interaction screened by scattering processes leaking from the low-energy sector. If W^L is further screened by the polarization P^L of the low-energy sector, the fully screened interaction is recovered:

$W = W^L/(1 - W^L P^L)$.

W^L yields the matrix elements of the partially screened U:

$$U_{mn}(\mathbf{R}, \omega) = \left\langle \phi_{m\mathbf{0}}\phi_{n\mathbf{R}} \right| \frac{v}{1 - vP^H(\omega)} \left| \phi_{m\mathbf{0}}\phi_{n\mathbf{R}} \right\rangle. \tag{4}$$

The above U defines the electron-electron interaction felt by the low-energy electrons in the *downfolded* model, i.e., after the high-energy degrees of freedom have been integrated out. The important thing to note here is that the partially screened U becomes *frequency dependent*, a direct consequence of the frequency dependence of P^H [34]. In the time-domain, this implies that the effective interaction becomes retarded. This *dynamical screening* is the main focus of our review. We will show that it can be explicitly taken into account in the solution of the low-energy models, and that it will affect the results in nontrivial ways.

It is interesting to remark here that the frequency dependence is particularly strong for monopole-monopole interactions (direct terms of the RPA expansion), while the screening is less effective for multipolar charge distributions ("exchange" terms in RPA), like the ones related to the estimate of the couplings J:

$$J_{mn}(\mathbf{R}, \omega) = \left\langle \phi_{m\mathbf{0}}\phi_{n\mathbf{R}} \right| \frac{v}{1 - vP^H(\omega)} \left| \phi_{n\mathbf{0}}\phi_{m\mathbf{R}} \right\rangle. \tag{5}$$

It turns out that U_{mn} is reduced by an order of magnitude with respect to U^{bare}_{mn}, while J_{mn} is almost unaffected by screening (change of typically less than 20% [35]). As an illustration, we plot the cRPA results for the 3-band model of $SrVO_3$ in Fig. 2.

We would like to stress that the cRPA values of U and J are not adjusted by fitting schemes or empirical arguments. They are evaluated from first-principles [37–44], according to a rigorous procedure, which has been recently extended also to the more involved case of entangled bands [45, 46], where the separation between the low- and high-energy sectors is not sharp, due to the hybridization between correlated orbitals and more extended ones.

Although the cRPA scheme seems plausible, it has some limitations, which originate from two sources: First, it is built on the RPA method which is not exact; second, the underlying DFT band structure is not exact either. While the first limitation can lead to underscreening or overscreening depending on the particular case, the second one is most severe in materials which are close to a Mott transition (which leads to strong modifications in the starting DFT band structure, and rearrangements of the screening bands), or in the case where the ligands are not included in the model (as usually the $p - d$ hybridization is

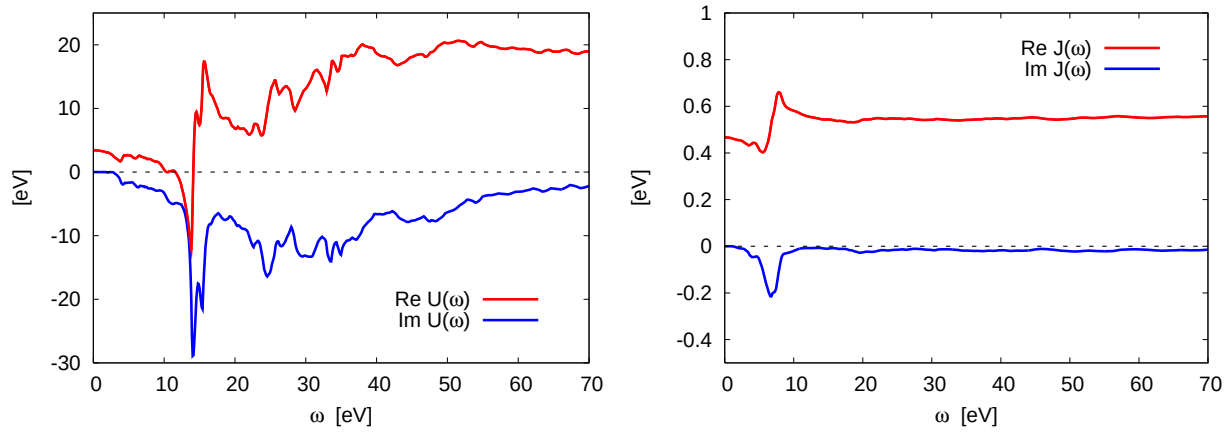


FIG. 2: cRPA $U(\omega) \equiv U_{nn}(\omega)$ and $J(\omega) \equiv J_{nm}(\omega)$ $(n \neq m)$ for the 3-band model of $SrVO_3$. (From Ref. [36].)

not well reproduced by DFT). A way to overcome the latter limitation is to use a better *ab initio* scheme to solve the full Hamiltonian, e. g. by replacing DFT by GW, while the former one can be reduced by improving upon the RPA theory. A possible approach is the recently developed constrained functional renormalization group (cfRG) method [47]. Testing the reliability of the cRPA method is a subject of current research [48].

Besides the cRPA method, other methods have been proposed to evaluate the local electron-electron couplings from *ab initio* calculations, such as the linear response approach [49, 50] and the constrained DFT [51, 52]. They however neglect the explicit frequency dependence of the Hubbard parameters. A slight variation of the cRPA method, which retains its full frequency dependence but is based on orbitals rather than bands, can be found in Ref. [53]. Along the same lines, i.e. working in the maximally localized orbitals space, Nomura *et al.* proposed to evaluate the partially screened U by undressing the fully screened coupling via the *local* polarization (i.e. by also including non-local processes in the low-energy manifold as active screening channels) [54]. This should give a U particularly suited for embedding theories such as DMFT, where only local correlations are taken into account. However, in our review, we will consider an alternative strategy, which is to include non-local processes in an explicit way, using extended-DMFT frameworks.

While the two-body part of the *downfolded* Hamiltonian is provided by the matrix elements of the partially screened interaction, Eqs. (4) and (5), the one-body part is given

by

$$t_{mn}(\mathbf{R}) = \langle \phi_{m\mathbf{0}} | H^{\mathrm{DFT}} | \phi_{n\mathbf{R}} \rangle, \tag{6}$$

where H^{DFT} is the DFT Hamiltonian determined in the first step. This $t_{mn}(\mathbf{R})$ already includes some correlation effects, as described by H^{DFT}. Therefore, one needs to correct the one-body part, i.e., subtract the low-energy correlation effects from the density functional, to avoid their *double counting* (DC). The so-called "double-counting correction" is common to all methods which augment the DFT band structure by explicit electron-electron interaction terms, such as DFT+U [55, 56] or DFT+DMFT [57]. This is the weakest point of the downfolding procedure, as an exact expression for the DC term is hard to derive. This is because the exchange correlation potential V_{xc} in H^{DFT} is a nonlinear functional of the total density, which makes it impossible to separate it into low- and high-energy contributions.

Several forms of approximate DC corrections have been proposed in the literature. One of the most successful for strongly correlated systems has proven to be the fully localized limit (FLL) form [58], which reads

$$\Sigma^{\mathrm{FLL\ DC}}_{mm'\sigma} = \delta_{mm'} \left(U \left(n_d - \frac{1}{2} \right) - J \left(n^{\sigma}_d - \frac{1}{2} \right) \right), \tag{7}$$

where n^{σ}_d is the spin-resolved occupancy of the correlated orbitals, and $n_d = n^{\uparrow}_d + n^{\downarrow}_d$. In the above equation, $U = \frac{1}{N^2} \sum_{mn} U_{mn}(\mathbf{0}, 0)$ is the average local static Coulomb interaction (N is the number of correlated bands), while the Hund's coupling J is related to the couplings in Eq. (5) through the relation $J = U - \frac{1}{N(N-1)} \sum_{m \neq n} \left(U_{mn}(\mathbf{0}, 0) - J_{mn}(\mathbf{0}, 0) \right)$. The form in Eq. (7) has been used in the *ab initio* applications presented in this review, unless otherwise stated.

Very recently, Haule proposed an improved DC scheme, in which a $V^{\mathrm{imp}}_{\mathrm{xc}}$ potential for the impurity system is constructed in terms of the local Green's functions and a local energy functional built on screened interactions [59]. He found that this procedure leads to double counting shifts in good agreement with an approximate DC correction obtained from Eq. (7), by replacing n with its closest integer value $n^0 = [n_d]$ (nominal DFT occupancy [60]), i.e.

$$\Sigma^{\mathrm{nominal\ DC}}_{mm'\sigma} = \delta_{mm'} \left(U \left(n^0 - \frac{1}{2} \right) - \frac{J}{2} \left(n^0 - 1 \right) \right). \tag{8}$$

Another interesting solution of the double counting problem has been proposed recently in Ref. [26]. It is based on the replacement of the exchange-correlation functional V_{xc} by the perturbative expansion of the potential to first order in the fully screened interaction

W, as it is done in the GW approach [1]. In contrast to $V_{\rm xc}$, in the GW framework one can easily separate the low-energy contributions ($\Sigma^L = G^L W$) from the high-energy ones ($\Sigma^H = G^H W$), where G^H (G^L) is the unperturbed Green's function living in the high- (low-) energy subspace. The off-diagonal matrix elements connecting the two subspaces are disregarded in the quasiparticle approximation. This leaves us with the operator $H^{\rm DFT} - V_{\rm xc} + \Sigma^H$, which is well defined in the high-energy space, although being frequency dependent. To get rid of the frequency dependence, the dynamic part included in the Σ^H self-energy is treated as a first-order variation around the Fermi energy, and condensed into a bandwidth renormalization factor $Z^{\rm H} = (1 - \frac{\partial {\rm Re}\Sigma^H}{\partial \omega})^{-1}$. The corresponding DC-free hoppings read

$$t^{\rm eff}_{mn}(\mathbf{R}) = \langle \phi_{m\mathbf{0}} | H^{\rm eff} | \phi_{n\mathbf{R}} \rangle, \tag{9}$$

with $H^{\rm eff} = Z^H \left(H^{\rm DFT} - V_{\rm xc} + {\rm Re}\Sigma^{\rm H}(0) \right)$. It turns out that the effective band structure in Eq. (9) has a larger bandwidth than the one in Eq. (6). Therefore, a proper treatment of the double counting correction leads to a much more complex rearrangement of the low-energy bands than the simple rigid (orbital independent) shift of the correlated manifold implied by Eq. (7). In most of the applications presented in this review, we are however going to use the latter correction, even though it is less accurate. It is simpler to compute, because it does not require a single-shot GW calculation of the full problem.

Usually, in the downfolded model one considers only *local* contributions in the two-body part, i.e. for $\mathbf{R} = \mathbf{0}$ in Eqs. (4) and (5), as the screening reduces the range of the interaction, making $U_{mn}(\mathbf{R}, \omega)$ a localized function in space. Of course the localization of these matrix elements depends on the type of system and on the correlation strength. In fact, the elimination of the low-energy metallic screening (by unscreening W with P^L) makes the partially screened interactions longer-ranged than the fully screened ones. Therefore, Hubbard-type approximations with only on-site interactions could be problematic. In fact, the restriction to Hubbard-like terms in most existing calculations is mainly due to the difficulty of dealing with long-ranged interactions in the solution of the low-energy model. Downfolded extended U-V models have however been taken into account in recent DMFT studies [61], and one of the purposes of this review is to explain the techniques which enable these simulations.

There has also been a vast amount of work focusing on the explicit solution of extended lattice models. These calculations keep the full spatial dependence of the Hamiltonian, both in the one- and two-body parts, but neglect dynamical effects. Successful methods

of this kind are for instance lattice and diagrammatic quantum Monte Carlo (although affected by the sign problem and/or by finite-size effects) [21, 62–66], exact diagonalization (which is limited to very small sizes), and methods based on matrix product states and their variants (most appropriate for low-dimensional systems) [67–69]. For models with purely local interactions, the exact diagonalization approach is also useful within cluster embedding theories [16], such as the variational cluster approximation (VCA) [70], cellular dynamical mean field theory (CDMFT) [71], or the dynamical cluster approximation (DCA) [72]). Here, we focus our attention on Green's function methods, and Green's function embedding approaches, such as the DMFT, where significant progress has been made in the consistent treatment of dynamically screened interaction parameters and the corresponding retardation effects.

From the point of view of including dynamically screened non-local interactions, a very appealing framework is the GW+DMFT theory, which treats the **k**-dependent electron correlations at the GW level, while the local diagrams are summed up to infinite order by the DMFT solver. This is justified by the interaction-range reduction from screening, which makes the U matrix more localized in $\mathbf{R}$. Therefore, a perturbative expansion of the self-energy may be a good approximation for the non-local U terms. However, we recall that a **k**-dependent Σ can also arise from purely local interactions, particularly in low dimensional systems (1D and 2D), where the strength of the resulting **k**-modulation can seriously challenge the validity of the perturbative nature of GW. As it will be explained in Sec. IV A 2, in the GW+DMFT formalism the dynamically screened interaction $U(\omega)$ is replaced by an auxiliary local interaction $\mathcal{U}(\omega)$, which becomes frequency dependent due to screening provided not only by high-energy states (related to *downfolding*) but also by non-local contributions which enter the local polarization function (related to two-particle *embedding*). This double nature of screening is captured by the GW+DMFT self-consistency construction, where the effective hybridization $\mathcal{G}_0$ and effective local interaction $\mathcal{U}$ are fixed by a double constraint imposed on the local Green's function and the local polarization, respectively.

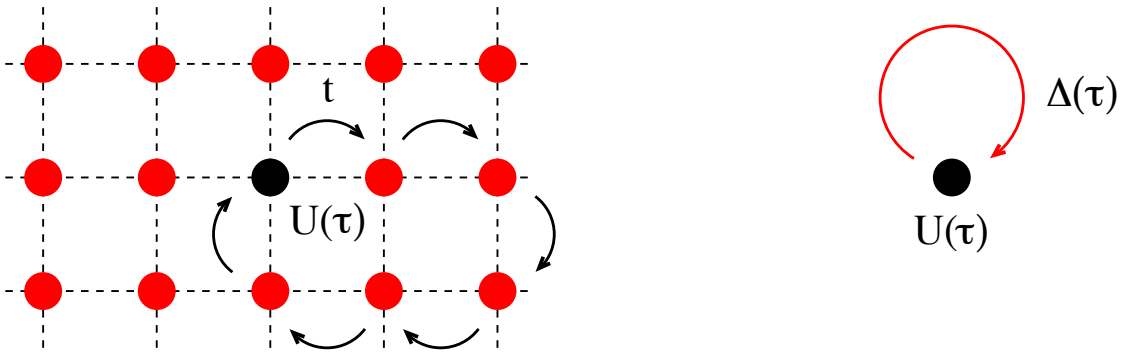


FIG. 3: Mapping of the Hubbard model to an effective single-site model (quantum impurity model).

III. SOLVING LOW-ENERGY MODELS WITH DYNAMICALLY SCREENED $U(\omega)$

Once a low energy lattice model with a few correlated orbitals and a frequency-dependent (retarded) monopole interaction U has been derived, we need a suitable method to solve it. Here, we focus on dynamical mean field based methods, which are adequate for the description of systems with a large coordination number, or systems in the strongly correlated (Mott insulating) regime, where the local physics is dominant. We will start by introducing the dynamical mean field approximation (Sec. III A), and then discuss various strategies for dealing with the retarded interaction originating from the coupling to a single bosonic mode (Sec. III B). These techniques will then be generalized to arbitrary $U(\omega)$, in Sec. III C. We also discuss the proper definition of effective low-energy models with static interactions (Sec. III D).

A. Dynamical mean field theory

For simplicity, we discuss the dynamical mean field approximation [73] for a simple, but fundamentally important model for correlated electron materials, the single-orbital Hubbard model with a retarded on-site interaction $U(\tau)$. Written in terms of fermionic creation and

annihilation operators $d^\dagger$ and d, the action of the lattice model is given by

$$S_{\text{Hubbard}} = -t\sum_{\langle ij\rangle\sigma}\int_0^\beta d\tau\left[d^\dagger_{i\sigma}(\tau)d_{j\sigma}(\tau)+d^\dagger_{j\sigma}(\tau)d_{i\sigma}(\tau)\right]-\mu\sum_{i\sigma}\int_0^\beta d\tau n_{i\sigma}(\tau)$$
$$+\frac{1}{2}\sum_i\int_0^\beta d\tau d\tau' U(\tau-\tau')n_i(\tau)n_i(\tau'), \tag{10}$$

with $n_\sigma = d^\dagger_\sigma d_\sigma$, $n = n_\uparrow + n_\downarrow$, t the hopping amplitude and $\beta = 1/T$ the inverse temperature. The partition function of the lattice model is $Z = \text{Tr}[\mathcal{T}e^{-S_{\text{Hubbard}}}]$, with $\mathcal{T}$ the time-ordering operator. Note that the retarded interaction also couples electrons of the same spin. In the spirit of mean-field approximations, we now focus on one particular site of the lattice (black dot in the left panel of Fig. 3) and replace the remaining degrees of freedom of the model by a hybridization term, which describes the hopping of electrons in and out of the impurity. The effective single-site problem then becomes an Anderson impurity model [74] with retarded interaction,

$$S_{\text{imp}} = \sum_\sigma\int_0^\beta d\tau d\tau' d^\dagger_\sigma(\tau)\Delta_\sigma(\tau-\tau')d_\sigma(\tau') - \mu\sum_\sigma\int_0^\beta d\tau n_\sigma(\tau)$$
$$+\frac{1}{2}\int_0^\beta d\tau d\tau' U(\tau-\tau')n(\tau)n(\tau'). \tag{11}$$

The hybridization function $\Delta(\tau)$ plays the role of the *dynamical mean field*, which is computed self-consistently in such a way that the Anderson impurity model mimics the lattice environment as closely as possible. More precisely, the self-consistent solution is constructed such that the impurity Green's function $G_{\text{imp}}(i\omega_n)$ reproduces the *local* lattice Green's function $G_{\text{loc}}(i\omega_n) \equiv G_{i,i}(i\omega_n)$. If $G(\mathbf{k}, i\omega_n)$ is the momentum-dependent lattice Green's function of the Hubbard model, we thus seek a hybridization function such that

$$\int (d\mathbf{k})G(\mathbf{k}, i\omega_n) \equiv G_{\text{imp}}(i\omega_n), \tag{12}$$

where $\int(d\mathbf{k})$ denotes a normalized integral over the Brillouin zone.

It is also useful to introduce the Green's function of the non-interacting impurity ("Weiss Green's function") $\mathcal{G}_0$, which is related to the hybridization function by

$$[\mathcal{G}_{0\sigma}]^{-1}(i\omega_n) = i\omega_n + \mu - \Delta_\sigma(i\omega_n). \tag{13}$$

Depending on the method used, it is more natural to work with the Weiss Green's function $\mathcal{G}_0$ rather than the hybridization function Δ.

1. DMFT approximation

We obtain the solution of Eq. (12) iteratively. However, it is not immediately clear how we can use this self-consistency condition to update the dynamical mean field. To define a practical procedure, we have to relate the left-hand-side of Eq. (12) to impurity model quantities. This step involves, as the essential approximation of the DMFT method, a simplification of the momentum-dependence of the lattice self-energy.

The self-energy describes the effect of interactions on the propagation of electrons. In the non-interacting model, the lattice Green's function is $G_0(\mathbf{k}, i\omega_n) = [i\omega_n + \mu - \epsilon_\mathbf{k}]^{-1}$, with $\epsilon_\mathbf{k}$ the Fourier transform of the hopping matrix. The Green's function of the interacting model is $G(\mathbf{k}, i\omega_n) = [i\omega_n + \mu - \epsilon_\mathbf{k} - \Sigma(\mathbf{k}, i\omega_n)]^{-1}$ with $\Sigma(\mathbf{k}, i\omega_n)$ the lattice self-energy. Therefore

$$\Sigma(\mathbf{k}, i\omega_n) = G_0^{-1}(\mathbf{k}, i\omega_n) - G^{-1}(\mathbf{k}, i\omega_n). \tag{14}$$

Similarly, we obtain the impurity self-energy as

$$\Sigma_{\mathrm{imp}}(i\omega_n) = \mathcal{G}_0^{-1}(i\omega_n) - G_{\mathrm{imp}}^{-1}(i\omega_n), \tag{15}$$

with $\mathcal{G}_0^{-1}$ defined in Eq. (13). The DMFT approximation is the identification of the lattice self-energy with the momentum-independent impurity self-energy,

$$\Sigma(\mathbf{k}, i\omega_n) \approx \Sigma_{\mathrm{imp}}(i\omega_n). \tag{16}$$

This approximation enables us to rewrite the self-consistency equation (12) as

$$\int (d\mathbf{k})[i\omega_n + \mu - \epsilon_\mathbf{k} - \Sigma_{\mathrm{imp}}(i\omega_n)]^{-1} \equiv G_{\mathrm{imp}}(i\omega_n). \tag{17}$$

Since both $G_{\mathrm{imp}}(i\omega_n)$ and $\Sigma_{\mathrm{imp}}(i\omega_n)$ are determined by the hybridization function $\Delta(\tau)$ (or $\mathcal{G}_0(\tau)$), Eq. (17) defines a self-consistency condition for these functions.

2. DMFT self-consistency loop

We now formulate the self-consistency loop for the Weiss Green's function $\mathcal{G}_0(i\omega_n)$. Starting from an arbitrary initial $\mathcal{G}_0(i\omega_n)$ (for example, the local Green's function of the non-interacting lattice model), we iterate the following steps until convergence:

1. Solve the impurity problem, that is, compute the impurity Green's function $G_{\mathrm{imp}}(i\omega_n)$ for the given $\mathcal{G}_0(i\omega_n)$,

2. Extract the self-energy of the impurity model: $\Sigma_{\rm imp}(i\omega_n) = \mathcal{G}_0^{-1}(i\omega_n) - G_{\rm imp}^{-1}(i\omega_n)$,

3. Identify the lattice self-energy with the impurity self-energy, $\Sigma(\mathbf{k}, i\omega_n) = \Sigma_{\rm imp}(i\omega_n)$ (DMFT approximation), and compute the local lattice Green's function $G_{\rm loc}(i\omega_n) = \int (d\mathbf{k})[i\omega_n + \mu - \epsilon_{\mathbf{k}} - \Sigma_{\rm imp}(i\omega_n)]^{-1}$,

4. Apply the DMFT self-consistency condition, $G_{\rm loc}(i\omega_n) = G_{\rm imp}(i\omega_n)$, and use it to define a new Weiss Green's function $\mathcal{G}_0^{-1}(i\omega_n) = G_{\rm loc}^{-1}(i\omega_n) + \Sigma_{\rm imp}(i\omega_n)$.

The computationally expensive step is the solution of the impurity problem (Step (i)). When the loop converges, the Weiss Green's function contains information about the topology of the lattice (through the density of states), and about the phase (metal, Mott insulator, antiferromagnetic insulator, ...). The impurity thus behaves, at least to some extent, as if it were a site of the lattice.

Obviously, a single-site impurity model does not capture all the physics. In particular, the DMFT approximation neglects all spatial fluctuations. These fluctuations are important, for example, in low-dimensional systems. The DMFT formalism is believed to provide a qualitatively correct description of three-dimensional unfrustrated lattice models. It becomes exact in the limit of infinite dimension [75, 76] or infinite coordination number (where spatial fluctuations are negligible), in the non-interacting limit ($U = 0$ implies $\Sigma = 0$), and in the atomic limit ($t = 0$ implies $\Delta = 0$).

B. Holstein-Hubbard model

In a Hamiltonian formulation, a lattice model with dynamically screened $U(\omega)$ can be represented by coupling the electron density on a given site to a continuum of bosonic modes with frequency ω, with appropriately chosen coupling strengths g_ω. If there is only a single bosonic mode with frequency ω_0 and coupling g, this corresponds to the Holstein-Hubbard model

$$\begin{aligned} H_{\rm HH} = &- t \sum_{\langle ij\rangle\sigma} (d_{i\sigma}^\dagger d_{j\sigma} + d_{j\sigma}^\dagger d_{i\sigma}) + U \sum_i n_{i\uparrow} n_{i\downarrow} - \mu \sum_{i\sigma} n_{i\sigma} \\ &+ g \sum_i (b_i^\dagger + b_i)(n_{i\uparrow} + n_{i\downarrow} - 1) + \omega_0 \sum_i b_i^\dagger b_i. \end{aligned} \tag{18}$$

Here, $b^\dagger$ denotes the boson creation operator. In the DMFT approximation, this lattice model is mapped onto a single-site impurity model with Hamiltonian $H_{\rm imp} = H_{\rm loc} + H_{\rm hyb} + H_{\rm bath}$, where

$$H_{\rm loc} = Un_\uparrow n_\downarrow - \mu(n_\uparrow + n_\downarrow) + g(n_\uparrow + n_\downarrow - 1)(b^\dagger + b) + \omega_0 b^\dagger b, \tag{19}$$

$$H_{\rm hyb} = \sum_{p\sigma} \Big[V_{p\sigma} d^\dagger_\sigma a_{p\sigma} + V^*_{p\sigma} a^\dagger_{p\sigma} d_\sigma \Big], \tag{20}$$

$$H_{\rm bath} = \sum_{p\sigma} \varepsilon_p a^\dagger_{p\sigma} a_{p\sigma}. \tag{21}$$

In terms of the harmonic oscillator position and momentum operators

$$X = (b^\dagger + b)/\sqrt{2}, \quad P = i(b^\dagger - b)/\sqrt{2}, \tag{22}$$

the local Hamiltonian can (up to a constant) be written as

$$H_{\rm loc} = Un_\uparrow n_\downarrow - \mu(n_\uparrow + n_\downarrow) + \sqrt{2}g(n_\uparrow + n_\downarrow - 1)X + \frac{\omega_0}{2}(X^2 + P^2), \tag{23}$$

so the physics of this model is that the charge couples to bosons describing either local lattice distortions (phonons) or local density fluctuations (plasmons).

The hybridization term $H_{\rm hyb}$ and the fermionic bath $H_{\rm bath}$ are defined such that the parameters $V_{p\sigma}$ and ε_p encode the hybridization function

$$\Delta_\sigma(i\omega_n) = \sum_p \frac{|V_{p\sigma}|^2}{i\omega_n - \varepsilon_p}. \tag{24}$$

On the other hand, integrating out the bosons yields the frequency-dependent interaction

$$U(i\nu_n) = U + \frac{2g^2\omega_0}{(i\nu_n)^2 - \omega_0^2}, \tag{25}$$

or, after analytical continuation to the real-frequency axis,

$$\mathrm{Re}U(\omega) = U + \frac{2g^2\omega_0}{\omega^2 - \omega_0^2}, \tag{26}$$

$$\mathrm{Im}U(\omega) = -g^2\pi(\delta(\omega - \omega_0) - \delta(\omega + \omega_0)). \tag{27}$$

The real part of the frequency-dependent interaction, illustrated in the left panel of Fig. 4 therefore has poles at the boson energy $\pm\omega_0$ and ranges from the unscreened interaction $U_{\rm bare} = U$ at high frequencies to a static (screened) interaction

$$U_{\rm scr} = U - 2g^2/\omega_0 \tag{28}$$

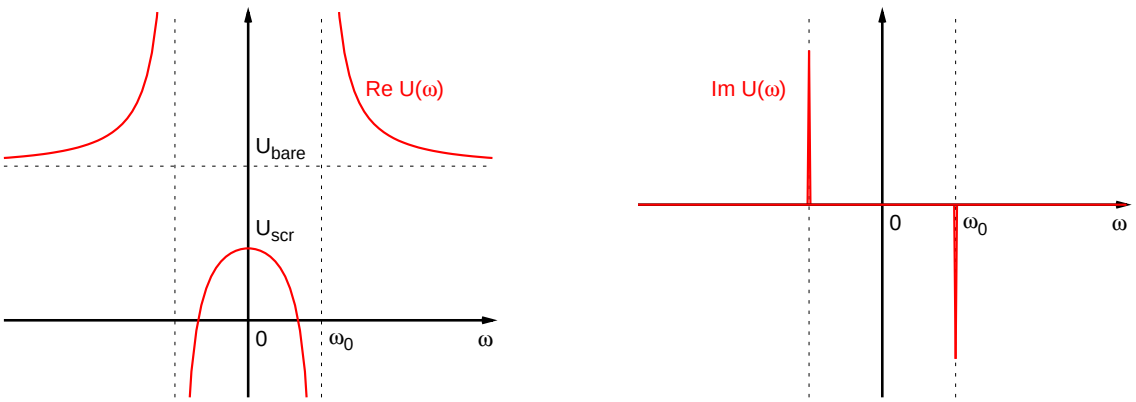


FIG. 4: Retarded interaction corresponding to the Holstein-Hubbard model with on-site interaction $U = U_{\rm bare}$, bosonic frequency ω_0 and electron-boson coupling g. The difference between bare and screened interaction is $\lambda = 2g^2/\omega_0$.

at $\omega = 0$.

While the DMFT approximation simplifies the problem considerably, by mapping the Holstein-Hubbard lattice model onto an auxiliary single-site impurity model, this effective model is still a complicated interacting many-body system. The electron-boson coupling introduces additional energy scales, besides the bandwidth and Kondo scale of the Anderson impurity model, namely the boson frequency ω_0 and the effective coupling strength $\lambda = 2g^2/\omega_0$. (In the high-frequency limit, the Holstein-Hubbard model simplifies to the Hubbard model with interaction $U_{\rm scr} = U - \lambda$.) Even in the DMFT approximation, and in the absence of long-range order, the Holstein-Hubbard model features a rich phase diagram with metallic, Mott insulating and bipolaronic insulating phases (Sec. III B 4) [77–81]. Antiferromagnetic, charge-ordered, superconducting and supersolid phases can also be found [82–84] if symmetry breaking is allowed. In the following, we will discuss efficient, yet accurate numerical approaches for solving the Holstein-Hubbard impurity problem, and also show how these techniques can be generalized to models with a coupling to a continuum of bosonic modes (or arbitrary retarded interactions). In fact, in the context of DMFT based *ab initio* simulations of correlated materials, the numerical challenge of treating dynamically screened interactions has been a major bottleneck which has hampered the implementation of advanced LDA+DMFT or GW+DMFT schemes for many years. The techniques

introduced in the following sections eliminate this bottleneck.

1. DALA approach

An approximate, but often very useful scheme is the so-called dynamic atomic-limit approximation (DALA) [85]. The main idea behind the DALA is to assume the following *ansatz* for the Green's function in imaginary time:

$$G(\tau) \;=\; G^{\text{static}}(\tau, \mu, U_{\text{scr}}) \exp\left(\frac{1}{\beta}\sum_{n\neq 0} \frac{U(i\nu_n) - U_{\text{scr}}}{\nu_n^2}\left(e^{i\nu_n\tau} - 1\right)\right), \tag{29}$$

where $G^{\text{static}}(\tau, \mu, U_{\text{scr}})$ is the "standard" Green's function of the model with static interaction U_{scr}. The factor which multiplies this Green's function takes into account the dynamic nature of the interaction. For the Holstein-Hubbard model, $U(i\nu_n)$ is defined in Eq. (25) and U_{scr} is the static screened interaction, defined in Eq. (28) as the zero-frequency limit of $U(\omega)$. This *ansatz* can be extended to arbitrary retarded interactions, fillings and number of orbitals. The latter dependence enters only through G^{static}. The above *ansatz* is exact in the atomic limit, that is, when the hybridization function Δ is set to zero and the impurity is isolated from the bath. In that limit the Green's function exactly factorizes into the Bose factor

$$F_{\text{DALA}}(\tau) = \exp\left(\frac{1}{\beta}\sum_{n\neq 0} \frac{U(i\nu_n) - U_{\text{scr}}}{\nu_n^2}\left(e^{i\nu_n\tau} - 1\right)\right), \tag{30}$$

depending only on dynamic U quantities, and a fermionic part G^{static}, which is the Green's function of the atomic limit with static screened U_{scr}. Other trivial exact limits are the static and non-interacting regimes, where $F_{\text{DALA}} = 1$.

Away from the atomic limit, one can still define the Bose factor F by

$$F(\tau) = \frac{G(\tau)}{G^{\text{static}}(\tau)}, \tag{31}$$

where $G(\tau)$ is the exact Green's function of the dynamic $U(\omega)$ problem and $G^{\text{static}}(\tau)$ is the exact Green's function of the Hubbard model with the same hybridization Δ as G but with the static Hubbard repulsion U_{scr}. One may then approximate the exact F by its atomic limit form F_{DALA} in Eq. (30). On the other hand, $G^{\text{static}}(\tau)$ can be obtained quite accurately by the solution of the Anderson model with static U_{scr} via "standard" methods. Therefore, in the DALA framework, the Green's function G of the full problem is approximated by the product $G^{\text{static}} F_{\text{DALA}}$.

Several remarks are in order here: (i) the DALA approach is non-perturbative in both the electron-electron screened interaction (through the $G^{\rm static}$ solution) *and* the electron-boson interaction, as one may argue from the exponential form of $F_{\rm DALA}$. In fact, $F_{\rm DALA}$ can also be seen as a cumulant expansion of the Green's function in the retarded interaction around $\Delta = 0$. A similar formalism has been used to compute the multiple plasmon satellites in silicon within the GW framework [8]. (ii) It has been shown that the DALA works quite well even away from the atomic limit, as long as $U_{\rm scr}$ and ω_0 are large compared to Δ. The approximation is problematic when the hybridization becomes essential for the low-energy low-temperature properties of the system. In particular, the DALA does not fulfill the Friedel sum rule, which sets the zero frequency limit of the exact Green's function, $\mathrm{Im}G(i0^+) = -4/D$, in a half-filled system with a semicircular density of states of bandwidth D. On the other hand, the DALA gives the right high-energy properties of the Green's function. (iii) Once the DALA solution of the Anderson impurity model with retarded interaction (Eq. (11)) is plugged into the DMFT cycle, the high-energy tails of the impurity Green's function, correctly modulated by the Bose factor $F_{\rm DALA}$, can have a strong impact on the self-consistent solution. In general, in the strongly correlated regime, the Mott transition line modified by retardation effects is quite accurately described by the DALA-DMFT solution of the lattice problem, as shown by a direct comparison with more advanced and accurate methods such as CTQMC (see Sec. III B 3 and Fig. 6). (iv) The very simple structure of the factorization *ansatz* used in the DALA framework is suggestive of the physics of the system. Indeed, the analytic form of $F_{\rm DALA}$ is the basis for a very effective analytic continuation method, described in Sec. V, which can produce the correct strength and position of the plasmon/phonon satellites in the spectral function of G. These high energy features are fingerprints of the dynamically screened electron-electron interaction and the DALA inspired analytic continuation can successfully resolve them.

2. Lang-Firsov approach

To introduce the Lang-Firsov (LF) approach, let us start with $H_{\rm imp}$, the single-band single-boson impurity Hamiltonian, introduced in Sec. III B. The Lang-Firsov transformation is a unitary transformation O of the fermion and boson local (impurity) operators, which eliminates the explicit electron-boson interaction and introduces dressed fermion quasipar-

ticles [86]. It is defined as follows:

$$O = \exp\left(-\frac{g}{\omega_0}(b^\dagger + b)\left(n_\uparrow + n_\downarrow - 1\right)\right), \tag{32}$$

$$\tilde{b} = O^{-1} b O = b - \frac{g}{\omega_0}\left(n_\uparrow + n_\downarrow - 1\right), \tag{33}$$

$$\tilde{d} = O^{-1} d O = \exp\left(-\frac{g}{\omega_0}(b^\dagger - b)\right) d, \tag{34}$$

where $\tilde{b}$ and $\tilde{d}$ are the transformed boson and fermion local operators, respectively. Therefore, the transformed impurity Hamiltonian $\tilde{H}_{\rm imp} = O^{-1} H_{\rm imp} O$ reads

$$\begin{aligned}\tilde{H}_{\rm imp} &= \sum_\sigma (-\mu + g^2/\omega_0) d^\dagger_\sigma d_\sigma + (U - 2g^2/\omega_0) n_\uparrow n_\downarrow + \omega_0 b^\dagger b \\ &+ \sum_{p\sigma}\left[V_{p\sigma}\exp\left(\frac{g}{\omega_0}(b^\dagger - b)\right) d^\dagger_\sigma a_{p\sigma} + V^*_{p\sigma}\exp\left(-\frac{g}{\omega_0}(b^\dagger - b)\right) a^\dagger_{p\sigma} d_\sigma\right] \\ &+ \sum_{p\sigma} \varepsilon_p a^\dagger_{p\sigma} a_{p\sigma}.\end{aligned} \tag{35}$$

A nontrivial effect of the LF transformation is that it changes the bare local Hubbard repulsion to the screened value $U_{\rm scr}$ (Eq. (28)). The interaction between dressed quasiparticles $\tilde{d}^\dagger|0\rangle$ is *reduced* by the presence of bosons. Analogously, we can write the impurity Green's function expressed in the transformed coordinates as

$$G(\tau) = Z^{-1}\langle T\tilde{d}^\dagger(0)\tilde{d}(\tau)\exp(-\beta\tilde{H})\rangle. \tag{36}$$

While the LF transformation reveals the role of bosons as mediators of the effective screened electron-electron interaction, which is the core of the screening theory presented in this review, the transformed $H_{\rm imp}$ in Eq. (35) is not immediately useful, as it shifts all the complexity of the electron-boson interaction into "electronic polarons", the dressed quasiparticles, i.e. electrons coupled to their surrounding polarization cloud. We need to make some approximation, which exploits the form of Eq. (35). A widely used one is to project the full Fock space onto the zero boson mode, the so-called LF approximation. The dynamic nature of the bosons is thereby reduced to their lowest harmonic level. It is clear that this approximation is good when $\omega_0 \gg E^*$, with E^* the relevant energy scale (bandwidth, hybridization, or Hubbard U repulsion) of the purely fermionic part. In this regime, the fermionic degrees of freedom are well separated from the bosonic high-energy ones. The LF approximation is exact in the antiadiabatic $\omega_0 \to \infty$ limit. It turns out that many realistic cases fall into

the antiadiabatic regime, as the characteristic screening frequency is usually the plasma frequency ω_0 of the homogeneous electron gas evaluated at the same average density as the real system. As shown in Ref. [85], $\omega_0 \geq 15$ eV in many correlated materials, which is normally larger than the energy scale of the correlated bands.

Once $\tilde{H}_{\rm imp}$ in Eq. (35) is projected onto the boson vacuum, the resulting LF approximated Anderson model becomes a standard (non-retarded) one with renormalized hybridization, shifted chemical potential, and screened on-site interaction:

$$\begin{aligned} H_0 \;=\; & \sum_{\sigma}(-\mu + g^2/\omega_0) d^\dagger_\sigma d_\sigma + (U - 2g^2/\omega_0) n_\uparrow n_\downarrow + \omega_0 b^\dagger b \\ & + \sum_{p\sigma}\left(V_{p\sigma} \exp\left(-\frac{g^2}{2\omega_0^2}\right) d^\dagger_\sigma a_{p\sigma} + V^*_{p\sigma} \exp\left(-\frac{g^2}{2\omega_0^2}\right) a^\dagger_{p\sigma} d_\sigma \right) \\ & + \sum_{p\sigma} \varepsilon_p a^\dagger_{p\sigma} a_{p\sigma}. \end{aligned} \tag{37}$$

Analogously, the LF approximated form of the Green's function in Eq. (36) is

$$\begin{aligned} G_{LF}(\tau) \;&=\; \exp\left(-g^2/\omega_0^2\right) Z^{-1} \langle T d^\dagger(0) d(\tau) \exp(-\beta H_0)\rangle \\ &\equiv\; \exp\left(-g^2/\omega_0^2\right) G_{H_0}(\tau). \end{aligned} \tag{38}$$

After integration over the fermionic bath, one obtains the following Lang-Firsov Green's function for the Anderson-Holstein model in Eqs. (19)-(21):

$$G_{LF}(i\omega_n) = \frac{\exp(-g^2/\omega_0^2)}{i\omega_n + \mu - g^2/\omega_0^2 - \exp(-g^2/\omega_0^2)\Delta(i\omega_n) - \Sigma[U_{\rm scr}](i\omega_n)}, \tag{39}$$

where $\Delta(i\omega_n) = \sum_{p\sigma} |V_{p\sigma}|^2/(i\omega_n - \varepsilon_p)$ is the hybridization function and $\Sigma[U_{\rm scr}](i\omega_n)$ is the self-energy, which depends on the screened value of U.

We note that the same $\exp\left(-g^2/\omega_0^2\right)$ factor renormalizes both the hybridization function and the Green's function. Therefore, the physical effect of retarding bosons, at least in the antiadiabatic regime, is threefold: (i) They reduce the Hubbard repulsion U to its screened value, (ii) they reduce the hopping elements between the impurity and the bath, which in the DMFT framework means reducing the bandwidth of the related lattice model, and (iii) they reduce the weight of the low-energy Green's function, which mimics the spectral weight transfer from the correlated manifold to higher-energy satellites, due to boson shake-off processes. All these physical insights provided by the LF approximation will be used in Sec. III D to derive an effective static model which properly describes the low-energy effects of screening in realistic strongly correlated systems.

In contrast to the DALA approximation, the LF Green's function of Eq. (39) fulfills the Friedel sum rule. Therefore the LF approximation can be used to correct the low-energy behavior of the DALA, as suggested in Ref. [85]. However, the combination of the two theories is quite cumbersome. If a numerically exact result is desirable, it is better to use the continuous-time Monte Carlo approach extended to dynamic interactions, which we describe in the next subsection.

3. Continuous-time Monte Carlo approach

Continuous-time Monte Carlo simulations rely on an expansion of the partition function into a series of diagrams and the stochastic sampling of (collections) of these diagrams. We represent the partition function as a sum (or, more precisely, integral) of configurations c with weight w_c,

$$Z = \sum_c w_c, \tag{40}$$

and implement a random walk $c_1 \to c_2 \to c_3 \to \ldots$ in configuration space in such a way that each configuration can be reached from any other in a finite number of steps (*ergodicity*) and that *detailed balance* is satisfied,

$$|w_{c_1}| p(c_1 \to c_2) = |w_{c_2}| p(c_2 \to c_1). \tag{41}$$

This assures that each configuration c is visited with a probability proportional to $|w_c|$. One can thus obtain an estimate for the Green's function from a finite number N of measurements:

$$g = \frac{\sum_c w_c g_c}{\sum_c w_c} = \frac{\sum_c |w_c| \mathrm{sign}_c g_c}{\sum_c |w_c| \mathrm{sign}_c} \approx \frac{\sum_{i=1}^N \mathrm{sign}_{c_i} g_{c_i}}{\sum_{i=1}^N \mathrm{sign}_{c_i}} = \frac{\langle \mathrm{sign} \cdot g \rangle_{MC}}{\langle \mathrm{sign} \rangle_{MC}}. \tag{42}$$

The error on this estimate decreases like $1/\sqrt{N}$.

The first step in the derivation of the continuous-time impurity solver [9] is to rewrite the partition function $Z = \mathrm{Tr}[e^{-\beta H_{\mathrm{imp}}}]$ as a time ordered exponential using some interaction representation. We split the impurity Hamiltonian into two parts, $H = H_1 + H_2$ and define the time-dependent operators in the interaction picture as $O(\tau) = e^{\tau H_1} O e^{-\tau H_1}$. We furthermore introduce the operator $A(\beta) = e^{\beta H_1} e^{-\beta H}$ and write the partition function as $Z = \mathrm{Tr}[e^{-\beta H_1} A(\beta)]$. The operator $A(\beta)$ satisfies $dA/d\beta = e^{\beta H_1}(H_1 - H)e^{-\beta H} = -H_2(\beta)A(\beta)$ and can be expressed as $A(\beta) = \mathcal{T} \exp[-\int_0^\beta d\tau H_2(\tau)]$.

In a second step, the time-ordered exponential is expanded into a power series,

$$\begin{aligned} Z &= \mathrm{Tr}\Big[e^{-\beta H_1}\mathcal{T}e^{-\int_0^\beta d\tau H_2(\tau)}\Big] \\ &= \sum_{n=0}^{\infty}\int_0^\beta d\tau_1 \ldots \int_{\tau_{n-1}}^\beta d\tau_n \mathrm{Tr}\Big[e^{-(\beta-\tau_n)H_1}(-H_2)\ldots e^{-(\tau_2-\tau_1)H_1}(-H_2)e^{-\tau_1 H_1}\Big], \end{aligned}$$

which is a representation of the partition function of the form (40), namely the sum of all configurations $c = \{\tau_1, \ldots, \tau_n\}$, $n = 0, 1, \ldots$, $\tau_i \in [0, \beta)$ with weight

$$w_c = \mathrm{Tr}\Big[e^{-(\beta-\tau_n)H_1}(-H_2)\ldots e^{-(\tau_2-\tau_1)H_1}(-H_2)e^{-\tau_1 H_1}\Big]d\tau^n. \tag{43}$$

In the following we will discuss the so-called "hybridization-expansion" approach [87, 88], which is based on an expansion of Z in powers of the impurity-bath hybridization term H_{hyb}, and an interaction representation in which the time evolution is determined by the *local* part $H_{\mathrm{loc}} + H_{\mathrm{bath}}$.

In the case of the Holstein-Hubbard model [89] the trace in Eq. (43) is over the Fock states of the impurity, the fermionic bath and the bosonic bath ($\mathrm{Tr} = \mathrm{Tr}_d\mathrm{Tr}_c\mathrm{Tr}_d$), or an equivalent basis. After the expansion in the hybridization operators, the time-evolution from one hybridization event to the next does no longer couple the impurity and the fermionic bath. Since the fermionic bath is noninteracting, the trace over the c-states can be evaluated analytically, resulting in two determinants (one for each spin) of matrices M_σ^{-1}, whose elements are the hybridization functions Δ evaluated at the time-intervals determined by the hybridization operator positions. The weight of a Monte Carlo configuration corresponding to a perturbation order $\sum_\sigma 2n_\sigma$ (n_σ creation operators $d_\sigma^\dagger(\tau_\sigma)$ and n_σ annihilation operators $d_\sigma(\tau'_\sigma)$) can thus be expressed as

$$\begin{aligned} w(\{O_i(\tau_i)\}) = Z_{0,c}\mathrm{Tr}_d\mathrm{Tr}_b\Big[\mathcal{T}e^{-\beta H_{\mathrm{loc}}}\prod_\sigma d_\sigma(\tau_{\sigma,n_\sigma})d_\sigma^\dagger(\tau'_{\sigma,n_\sigma})\ldots \\ \ldots d_\sigma(\tau_{\sigma,1})d_\sigma^\dagger(\tau'_{\sigma,1})\Big]\prod_\sigma(\det M_\sigma^{-1})(d\tau)^{2n_\sigma}, \end{aligned} \tag{44}$$

where the the matrix elements are $M_\sigma^{-1}(i,j) = \Delta_\sigma(\tau'_{\sigma,i} - \tau_{\sigma,j})$. We denote the time-ordered sequence of impurity creation and annihilation operators by $\{O_i(\tau_i)\}$ ($1 \le i \le 2n$, $n = \sum_\sigma n_\sigma$). At this stage, the time-evolution from one operator to the next still includes the coupling to the bosons. In order to evaluate the trace over the boson states, we perform the Lang-Firsov [86] transformation introduced in the previous subsection. Here, we express it in terms of the boson position and momentum operators X and P defined in Eq. (22).

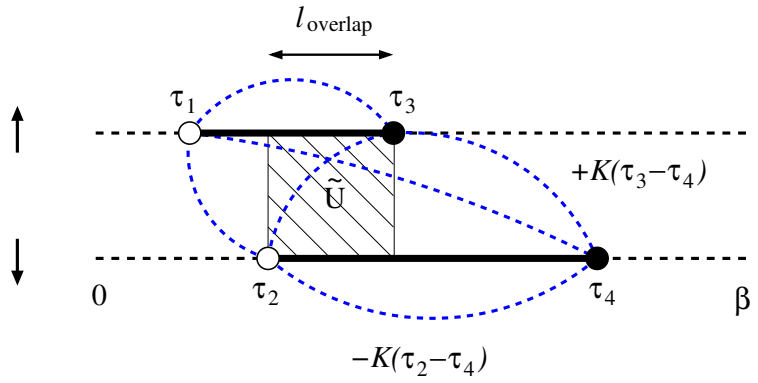


FIG. 5: Illustration of a segment configuration with one segment for spin up and spin down. The interaction and chemical potential contribution to the configuration weight can be obtained from the lengths and overlaps of the segments. The boson contribution is indicated by the blue dashed lines, which connect all pairs of operators.

The unitary transformation specified by e^{iPX_0} shifts X by X_0, and if we choose $X_0 = (\sqrt{2}g/\omega_0)(n_\uparrow + n_\downarrow - 1)$, the transformed local Hamiltonian (23),

$$\begin{aligned} \tilde{H}_{\rm loc} &= e^{-iPX_0} H_{\rm loc} e^{iPX_0} \\ &= \tilde{U}\tilde{n}_\uparrow\tilde{n}_\downarrow - \tilde{\mu}(\tilde{n}_\uparrow + \tilde{n}_\downarrow) + \frac{\omega_0}{2}(X^2 + P^2), \end{aligned} \tag{45}$$

has no explicit electron-phonon coupling anymore. $\tilde{H}_{\rm loc}$ is of the Hubbard form but with modified chemical potential and interaction strength,

$$\tilde{\mu} = \mu - g^2/\omega_0, \tag{46}$$

$$\tilde{U} = U - 2g^2/\omega_0. \tag{47}$$

Note that $\tilde{U} = U_{\rm scr}$ (Eq. (28)). The transformation also affects the impurity creation and annihilation operators, which acquire a boson factor:

$$\tilde{d}^\dagger_\sigma = e^{iPX_0} d^\dagger_\sigma e^{-iPX_0} = e^{\frac{g}{\omega_0}(b^\dagger - b)} d^\dagger_\sigma, \tag{48}$$

$$\tilde{d}_\sigma = e^{iPX_0} d_\sigma e^{-iPX_0} = e^{-\frac{g}{\omega_0}(b^\dagger - b)} d_\sigma. \tag{49}$$

After this transformation, the electron and boson sectors are decoupled and the trace in Eq. (44) becomes the product of a term involving electron operators which is identical to the weight appearing in a Hubbard model simulation (with shifted $\tilde{U}$ and $\tilde{\mu}$), and a phonon term which is the expectation value of a product of exponentials of boson operators, to be

evaluated with the noninteracting boson Hamiltonian $\omega_0 b^\dagger b$. The phonon contribution w_b to the weight (44) can be written as

$$w_b(\{O_i(\tau_i)\}) \;=\; Z_{0,b}\left\langle e^{s_{2n}A(\tau_{2n})}e^{s_{2n-1}A(\tau_{2n-1})}\cdots e^{s_1A(\tau_1)}\right\rangle_b, \tag{50}$$

with $Z_{0,b}$ the noninteracting boson partition function, $\langle\ldots\rangle_b = \mathrm{Tr}_b[\ldots]/Z_{0,b}$, $0 \le \tau_1 < \tau_2 < \ldots < \tau_{2n} < \beta$, $s_i = 1$ (-1) if the i^{th} operator is a creation (annihilation) operator and $A(\tau)$ given by

$$A(\tau) = \frac{g}{\omega_0}(e^{\omega_0\tau}b^\dagger - e^{-\omega_0\tau}b). \tag{51}$$

The expectation value is to be taken in the thermal state of free bosons. Using $e^{sA(\tau)} = e^{-g^2/(2\omega_0^2)}e^{s(g/\omega_0)e^{\omega_0\tau}b^\dagger}e^{-s(g/\omega_0)e^{-\omega_0\tau}b}$, one finds the disentangled expression

$$\begin{aligned} w_b(\{O_i(\tau_i)\}) \;=\; & Z_{0,b}e^{-n(g^2/\omega_0^2)}e^{-\sum_{2n\ge i>j\ge 1}s_is_j(g^2/\omega_0^2)e^{-\omega_0(\tau_i-\tau_j)}} \\ & \times\left\langle e^{\sum_j s_j(g/\omega_0)e^{\omega_0\tau_j}b^\dagger}e^{-\sum_j s_j(g/\omega_0)e^{-\omega_0\tau_j}b}\right\rangle_b. \end{aligned} \tag{52}$$

For thermal expectation values, we have the formula [90] $\langle e^{ub^\dagger}e^{vb}\rangle_b = e^{uv/(e^{\beta\omega_0}-1)}$, which gives the final expression for the bosonic weight

$$w_b(\{O_i(\tau_i)\}) = Z_{0,b}\exp\left[\sum_{2n\ge i>j\ge 1} s_is_jK(\tau_i-\tau_j)\right], \tag{53}$$

$$K(\tau) = -\frac{g^2}{\omega_0^2}\frac{\cosh(\omega_0(\beta/2-\tau)) - \cosh(\beta\omega_0/2)}{\sinh(\beta\omega_0/2)}. \tag{54}$$

The total weight (44) can be expressed as

$$w(\{O_i(\tau_i)\}) = w_b(\{O_i(\tau_i)\})\tilde{w}_{\mathrm{Hubbard}}(\{O_i(\tau_i)\}), \tag{55}$$

where $\tilde{w}_{\mathrm{Hubbard}}$ denotes the weight of a corresponding configuration in the pure Hubbard impurity model (with parameters modified according to Eqs. (46) and (47)). This weight can be efficiently computed using the segment picture [87] (see Fig. 5). For each spin, we mark the imaginary-time intervals corresponding to an occupied impurity state by a segment. Then, $w_{\mathrm{Hubbard}}(\{O_i(\tau_i)\})$ can be obtained from the total length l_σ of these segments and the total length l_{overlap} of the overlaps between up-spin and down-spin segments:

$$w_{\mathrm{Hubbard}}(\{O_i(\tau_i)\}) = sZ_{0,c}e^{\tilde{\mu}(l_\uparrow+l_\downarrow)-\tilde{U}l_{\mathrm{overlap}}}\prod_\sigma(\det M_\sigma^{-1})(d\tau)^{2n}, \tag{56}$$

with s a permutation sign related to the time-ordering of the impurity creation and annihilation operators.

In a segment insertion move, a pair of σ-operators is added to the sequence $\{O_i(\tau_i)\}$. For the Metropolis test, one has to compute the ratio $w_b^{\rm new}/w_b^{\rm old}$ and a determinant ratio $\det M^{-1}_{\sigma,\rm new}/\det M^{-1}_{\sigma,\rm old}$, both at a cost $O(n)$. The ratio of the traces over the impurity states (evaluated from the segment lengths and overlaps) is also at most $O(n)$. If the move is accepted, the matrix M_σ needs to be updated. This is the computationally most expensive step requiring an effort $O(n^2)$, but this is identical to the effort in the Hubbard model without electron-phonon coupling [9]. Hence, the treatment of the bosons does not affect the scaling of the algorithm.

Observables such as the Green's function or double occupation can be measured as in the case with static interaction [87], i.e. from the elements of the inverse hybridization matrix and the segment overlaps. Specifically, the formula for the Green's function reads

$$G_\sigma(\tau) = \left\langle -\sum_{ij} \frac{1}{\beta}\delta(\tau, \tau_i - \tau'_j)(M_\sigma)_{ij} \right\rangle \tag{57}$$

with $\delta(\tau,\tau') = \delta(\tau-\tau')$ for $\tau' > 0$, $\delta(\tau,\tau') = -\delta(\tau-\tau'-\beta)$ for $\tau' < 0$, and τ_i (τ'_j) denoting the time of the ith annihilation (jth creation) operator. Efficient measurement schemes for the self-energy and vertex function [91] on the other hand need to be specifically adapted to the case of retarded interactions. A detailed discussion of these techniques can be found in Ref. [92].

As a final remark, we note that the DALA Bose factor reported in Eq. (30) of Sec. III B 1 can be written in terms of the K function (54) as $F_{\rm DALA}(\tau) = \exp(-K(\tau))$. In the atomic limit, i.e. zero hybridization, only the 0-th order term in the hybridization expansion survives, leading to a total Green's function $G_\sigma(\tau)$ consisting of the product of the global factor $F_{\rm DALA}(\tau)$ and the static Green's function, as explained in Sec. III B 1. Therefore, the exact CTQMC hybridization expansion algorithm with retarded interactions naturally reduces to the DALA result in the atomic limit.

4. Phase diagram

We illustrate the DMFT phase diagram of the half-filled Holstein-Hubbard model in the left panel of Fig. 6. The results are for a semi-circular density of states with bandwidth 4 and inverse temperature $\beta = 50$. A paramagnetic solution is enforced. At weak boson coupling g, there is a metallic phase at small $U_{\rm bare}$ and a Mott insulating phase for sufficiently

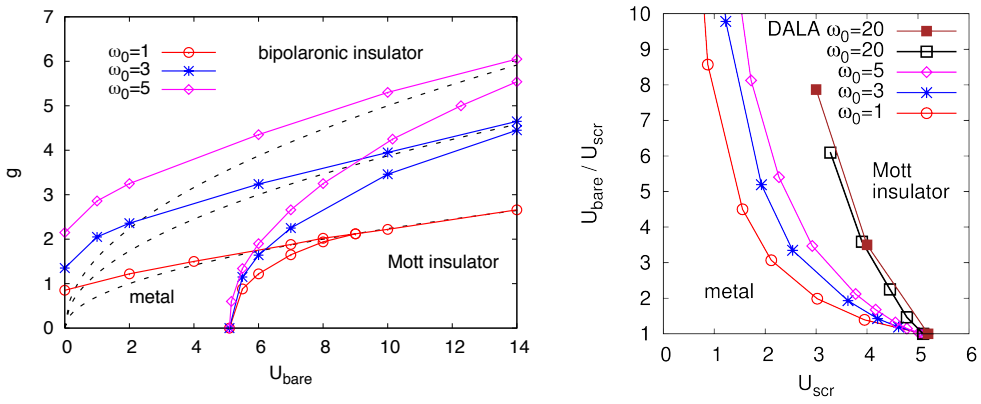


FIG. 6: Left panel: half-filled metal-insulator phase diagram for $\beta = 50$ in the space of bare interaction $U_{\rm bare}$ and boson coupling strength g for different values of the screening frequency ω_0 (DMFT solution for a semi-circular density of states with bandwidth 4). The dashed lines indicate the boson coupling at which the screened interaction $U_{\rm scr}$ changes sign. Right panel: phase diagram in the space of screened and bare interaction. The approximated DALA results (Sec. III B 1), corrected by the low-energy Lang-Firsov behavior, are also reported for $\omega_0 = 20$ and different coupling strengths. (Adapted from Ref. [93].)

large $U_{\rm bare}$. As g is increased, the effective on-site interaction is reduced and eventually, the system makes a transition to a bipolaronic insulating phase. The dashed line indicates the value of g at which the screened interaction $U_{\rm scr} = U_{\rm bare} - 2g^2/\omega_0$ vanishes. For small boson frequency, the sign change in $U_{\rm scr}$ essentially coincides with the transition from Mott insulator to bipolaronic insulator, while for large boson frequency, there exists a metallic solution near $U_{\rm scr} = 0$, which separates the two insulators.

The right panel shows the metal-to-Mott insulator phase boundary in the space of $U_{\rm bare}/U_{\rm scr}$ and $U_{\rm scr}$, for different values of the boson frequency. A larger $U_{\rm bare}/U_{\rm scr}$ stabilizes the Mott insulator, and this effect is most pronounced for a low screening frequency.

C. General $U(\omega)$

It follows from Eq. (27) that the Holstein-Hubbard model corresponds to a frequency-dependent interaction $U(\omega)$, whose imaginary part is a δ-function at $\omega = \pm\omega_0$, with a weight

given by $\mp g^2\pi$. An arbitrary $U(\omega)$ can thus be thought of as arising from a Holstein-type coupling to a continuum of bosonic modes with energy ω and coupling strength g_ω given by $g_\omega^2 = -\mathrm{Im}U(\omega)/\pi$. According to the derivation in Sec. III B 3 each boson contributes an effective "interaction" $K(\tau_i - \tau_j) = -\frac{g_\omega^2}{\omega^2}\frac{\cosh(\omega(\beta/2-(\tau_i-\tau_j))-\cosh(\beta\omega/2)}{\sinh(\beta\omega/2)}$ between impurity creation or annihilation operators at imaginary times τ_i and τ_j (Eq. (54)). Hence, the hybridization expansion Monte Carlo simulation for a model with general $U(\omega)$ proceeds exactly as in the case of the Holstein-Hubbard model, but with the K-function replaced by [93]

$$K(\tau) = \int_0^\infty d\omega \frac{\mathrm{Im}U(\omega)}{\pi\omega^2}\frac{\cosh(\omega(\beta/2-\tau))-\cosh(\beta\omega/2)}{\sinh(\beta\omega/2)} \tag{58}$$

and the shifted interaction and chemical potential (Eqs. (46) and (47)) given by

$$\tilde{\mu} = \mu + \int_0^\infty d\omega \frac{\mathrm{Im}U(\omega)}{\pi\omega}, \tag{59}$$

$$\tilde{U} = U + 2\int_0^\infty d\omega \frac{\mathrm{Im}U(\omega)}{\pi\omega} = U_{\mathrm{scr}}. \tag{60}$$

The last identity follows from the Kramers-Kronig relation and the anti-symmetry of $\mathrm{Im}U(\omega)$.

These formulas can also be derived from the impurity action with retarded $U(\tau)$, without the detour through the Hamiltonian representation [94]. In fact, it is easy to evaluate the interaction contribution $\frac{1}{2}\int_0^\beta d\tau d\tau' U(\tau-\tau')n(\tau)n(\tau')$ in the action (11) for a given segment configuration. In a first step, we split the interaction into its instantaneous contribution and a retarded part:

$$U(\tau) = U_{\mathrm{bare}}\delta(\tau) + U_{\mathrm{ret}}(\tau-\tau'), \tag{61}$$

$$U(\omega) = U_{\mathrm{bare}} + U_{\mathrm{ret}}(\omega). \tag{62}$$

$U_{\mathrm{ret}}(\omega)$ has the same imaginary part as $U(\omega)$, but its real part approaches 0 in the high frequency limit. Therefore, we have the spectral representation ($0 \le \tau \le \beta$)

$$U_{\mathrm{ret}}(\tau) = -\frac{1}{\pi}\int_{-\infty}^\infty d\omega \mathrm{Im}U(\omega)\frac{e^{-\omega\tau}}{e^{-\omega\beta}-1} = \frac{1}{\pi}\int_0^\infty d\omega \mathrm{Im}U(\omega)\frac{\cosh(\omega(\beta/2-\tau))}{\sinh(\omega\beta/2)}. \tag{63}$$

Plugging Eq. (63) into the expression for the interaction contribution and using $n = n_\uparrow + n_\downarrow$, as well as $n_\sigma^2 = n_\sigma$, we find

$$\begin{aligned}\frac{1}{2}\int_0^\beta d\tau d\tau' U(\tau-\tau')n(\tau)n(\tau') &= U_{\mathrm{bare}}\int_0^\beta d\tau n_\uparrow(\tau)n_\downarrow(\tau) + \frac{U_{\mathrm{bare}}}{2}\int_0^\beta d\tau(n_\uparrow(\tau)+n_\downarrow(\tau)) \\ &+ \int_0^\beta d\tau d\tau' n_\uparrow(\tau)U_{\mathrm{ret}}(\tau-\tau')n_\downarrow(\tau') + \sum_\sigma \frac{1}{2}\int_0^\beta d\tau d\tau' n_\sigma(\tau)U_{\mathrm{ret}}(\tau-\tau')n_\sigma(\tau').\end{aligned} \tag{64}$$

The first term yields $U_{\rm bare} l_{\rm overlap}$ and the second term a shift of the chemical potential. The contribution from the retarded interaction, which acts both between same and opposite spin electrons, is given by the last two terms. Since n_σ is 1 only on a segment of spin σ, and zero otherwise, we can express the retarded contribution as

$$\sum_{k_1 \neq k_2} \int_{k_1} d\tau_1 \int_{k_2} d\tau_2 U_{\rm ret}(\tau_1 - \tau_2) + \frac{1}{2} \sum_{k} \int_{k} d\tau_1 \int_{k} d\tau_2 U_{\rm ret}(\tau_1 - \tau_2), \tag{65}$$

Where k_i denotes the segment i. The first term is the inter-segment contribution and the second term the intra-segment contribution of the retarded interaction. Now, let as assume that we know a β-periodic function $h(\tau)$, which is even, and satisfies $\frac{d^2h}{d\tau^2} = U_{\rm ret}(\tau)$ in the interval $0 < \tau < \beta$. With the help of this function, we can express the integral over a pair of segments as $\int_{k_1} d\tau_1 \int_{k_2} d\tau_2 U_{\rm ret}(\tau_1 - \tau_2) = -h(\tau_1^e - \tau_2^e) + h(\tau_1^e - \tau_2^s) + h(\tau_1^s - \tau_2^e) - h(\tau_1^s - \tau_2^s)$, where τ_i^s (τ_i^e) denotes the start and end points of segment k_i. Similarly, the double integral over segment k evaluates to $h(\tau_e - \tau_s) - h(0)$. Hence, the retarded interaction energy for a segment configuration with n creation and n annihilation operators can be written as

$$-\sum_{i>j} s_i s_j (h(\tau_i - \tau_j) - h(0)), \tag{66}$$

where we assumed that the operators are time-ordered ($\tau_i > \tau_j$ for $i > j$) and the sign s_i is $+1$ if the ith operator is a creation operator, and -1 if it is an annihilation operator.

From the expression (63) we find by double-integration that $h(\tau) - h(0) = K(\tau)$, the function defined in Eq. (58). Hence, the nonlocal interaction contribution to the weight becomes $\exp\big[\sum_{i>j} s_i s_j K(\tau_i - \tau_j)\big]$, as derived in section III B 3.

There is one subtlety which we need to consider: due to the slope-discontinuity in the β-periodic function $h(\tau)$ at $\tau = 0$, the second derivative yields a delta-function contribution with weight

$$-\frac{2}{\pi} \int_0^\infty d\omega \frac{{\rm Im}U(\omega)}{\omega} = -{\rm Re}U_{\rm ret}(\omega = 0) = -(U_{\rm scr} - U_{\rm bare}). \tag{67}$$

So, if we use this $h(\tau)$ in the formula for the retarded interaction contribution, we have to subtract $-(U_{\rm scr} - U_{\rm bare})\delta(\tau)$ from the instantaneous interaction. The total instantaneous interaction thus becomes $(U_{\rm bare} + (U_{\rm scr} - U_{\rm bare}))\delta(\tau) = U_{\rm scr}\delta(\tau)$, which means that the overlap contribution to the weight of a segment configuration has to be evaluated with the screened interaction. A similar shift is introduced to the chemical potential, so that the end result is identical to Eqs. (59) and (60).

D. Effective static model

Even though there exist efficient numerical methods for treating dynamically screened monopole interactions, it is conceptually interesting to ask how to define a low-energy model with static interactions, which properly captures the low-energy physics. To derive this model, we again first consider the simple case of the Holstein-Hubbard model (18). Applying the Lang-Firsov transformation [86] $H_{\rm HH} \to H_{\rm LF} = e^S H_{\rm HH} e^{-S}$ with $S = \frac{g}{\omega_0}\sum_i (n_{i\uparrow} + n_{i\downarrow} - 1)(b_i^\dagger + b_i)$ yields a decoupled Hamiltonian in terms of the polaron operators (48) and (49):

$$H_{\rm LF} = -t \sum_{\langle ij\rangle\sigma} (\tilde{d}_{i\sigma}^\dagger \tilde{d}_{j\sigma} + \tilde{d}_{j\sigma}^\dagger \tilde{d}_{i\sigma}) + U_{\rm scr} \sum_i n_{i\uparrow} n_{i\downarrow} - \mu \sum_{i\sigma} n_{i\sigma} + \sum_i \omega_0 b_i^\dagger b_i, \tag{68}$$

with $U_{\rm scr} = U - 2g^2/\omega_0$. As shown in Ref. [95], the low-energy effective model can now be defined by projecting this Hamiltonian onto the zero-boson subspace:

$$H_{\rm eff} = \langle 0|H_{\rm LF}|0\rangle = -Z_B t \sum_{\langle ij\rangle\sigma} (d_{i\sigma}^\dagger d_{j\sigma} + d_{j\sigma}^\dagger d_{i\sigma}) + U_{\rm scr} \sum_i n_{i\uparrow} n_{i\downarrow} - \mu \sum_{i\sigma} n_{i\sigma}. \tag{69}$$

$H_{\rm eff}$ is of the Hubbard form and involves the original fermionic operators $d^\dagger$ and d, the screened interaction $U_{\rm scr}$, and a hopping term reduced by a factor

$$Z_B = \exp[-g^2/\omega_0^2]. \tag{70}$$

Hence, a crucial effect of the dynamical screening is an effective bandwidth reduction.

The projection onto the zero boson subspace is a good approximation if the screening frequency ω_0 is large. As an illustration of this, we list in Tab. I the critical interaction strengths for the Mott transition in a DMFT simulation of the Holstein-Hubbard model with semi-circular density of states of bandwidth 4, at inverse temperature $\beta = 100$. The result from the exact DMFT treatment based on the method explained in Sec. III B 3 is compared to the result of a DMFT treatment of the effective static model (69), with the bandwidth renormalization (70).

In a model with a general $U(\omega)$ we can again view the frequency dependence as arising from a coupling to a continuum of bosonic modes with frequency ω and coupling strength $g_\omega^2 = -{\rm Im}U(\omega)/\pi$. The screened interaction is then given by Eq. (60) (or simply ${\rm Re}U(\omega = 0)$), and the formula for the Lang-Firsov renormalization factor becomes

$$Z_B = \exp\Big[\frac{1}{\pi}\int_0^\infty d\omega \frac{{\rm Im}U(\omega)}{\omega^2}\Big]. \tag{71}$$

TABLE I: Critical interaction strength $U_{0,\mathrm{crit}}^{\mathrm{exact}}$ for the Mott transition obtained from the single-site DMFT approximation to model (18) at inverse temperature $\beta = 100$, compared to the estimate $U_{0,\mathrm{crit}}^{\mathrm{eff}}$ from the solution of the effective static model (69) for different values of the screening frequency ω_0 and coupling strength g. Also shown is the Lang-Firsov renormalization factor (70). (From Ref. [95].)

ω_0	g	Z_B	$U_{\mathrm{crit}}^{\mathrm{exact}}$	$U_{\mathrm{crit}}^{\mathrm{eff}}$
1.5	0.820	0.74	2.103	1.891
1.5	2.010	0.17	0.613	0.423
2.5	1.330	0.75	2.085	1.921
2.5	2.770	0.29	0.861	0.747
10.0	3.725	0.87	2.225	2.220
10.0	6.465	0.66	1.640	1.679

In a model with strongly correlated "d" states and itinerant "p" states, and associated hopping parameters $\mathcal{T}_{pp}$, $\mathcal{T}_{pd}$ and $\mathcal{T}_{dd}$, the Lang-Firsov transformation and subsequent projection onto the zero-boson sector leads to a renormalization of each d operator by a factor $\sqrt{Z_B} = \langle 0| \exp(\frac{g}{\omega_0}(b_i - b_i^\dagger))|0\rangle$. Hence, the hopping part of the one-particle Hamiltonian is renormalized as

$$\left(p^\dagger d^\dagger\right) \begin{pmatrix} \mathcal{T}_{pp} & \sqrt{Z_B}\mathcal{T}_{pd} \\ \sqrt{Z_B}\mathcal{T}_{pd}^\dagger & Z_B\mathcal{T}_{dd} \end{pmatrix} \begin{pmatrix} p \\ d \end{pmatrix}. \tag{72}$$

This expression shows that the bandwidth reduction implied by the effective model cannot simply be translated into an effective increase of the on-site interaction in the multi-band situation typically considered in first-principles calculations.

E. Multiorbital systems

Up to now, we have discussed dynamically screened on-site interactions in a single-orbital model. The extension of these techniques to multi-orbital systems is straight-forward if the total charge on a given site is screened, that is, if the electron-boson coupling in a

Hamiltonian formulation is of the type

$$H_{\text{el-b}} = \sum_{i,\lambda} g_{i,\lambda} n_i^{\text{tot}} (b_{i,\lambda}^\dagger + b_{i,\lambda}), \tag{73}$$

with i the site index, $b_{i,\lambda}$ the annihilation operator for the oscillator of frequency $\omega_{i,\lambda}$ at site i and $g_{i,\lambda}$ the corresponding coupling strength. The total charge on site i is $n_i^{\text{tot}} = \sum_{\alpha=1}^{N_{\text{orbitals}}} \sum_\sigma n_{i,\alpha,\sigma}$. Within DMFT, one then has to solve a multi-orbital impurity system with an analogous electron-boson coupling. In the hybridization expansion formalism introduced in Sec. III B 3, each hybridization operator changes the total charge on the multi-orbital impurity by ± 1 and hence excites the bosons. After integrating out the bosons, one again finds an "interaction" of the form (58) between each operator pair, with a sign that depends on the operator types (creation or annihilation operators). Now, $U(\omega)$ denotes the dynamically screened monopole interaction. In the trace calculation, the intra- and inter-orbital interaction parameters are replaced by the static values, in analogy to Eq. (60). Note that this procedure works both in the case of density-density interactions (segment formalism [87]), and for models with rotationally invariant interactions (matrix formalism [88]), because spin-flips and pair-hoppings do not change the total charge on the impurity and hence do not couple to the bosons.

A more complicated situation arises if the Hund coupling has a significant frequency dependence, such as in alkali-doped fullerides [42, 96], where Jahn-Teller screening may even produce an overscreened (negative) static J. In this case, the changes in the orbital occupation associated with spin-flips and pair-hoppings will couple to bosonic modes and the rotationally invariant system becomes much more difficult to simulate. After integrating out the phonons, the interaction part of the action reads [97]

$$\begin{aligned} S_{\text{int}} = & \frac{1}{2} \sum_{\substack{\alpha,\sigma \\ \beta,\sigma'}} \int_0^\beta d\tau \int_0^\beta d\tau' n_{\alpha,\sigma}(\tau) U_{\alpha,\sigma}^{\beta,\sigma'}(\tau - \tau') n_{\beta,\sigma'}(\tau') \\ & + \frac{1}{2} \sum_{\substack{\alpha,\beta,\sigma,\sigma' \\ \alpha<\beta}} \int_0^\beta d\tau \int_0^\beta d\tau' J(\tau - \tau') \Big[X_\sigma^{\alpha\beta}(\tau) X_{\sigma'}^{\beta\alpha}(\tau') \\ & + X_\sigma^{\beta\alpha}(\tau) X_{\sigma'}^{\alpha\beta}(\tau') + X_\sigma^{\alpha\beta}(\tau) X_{\sigma'}^{\alpha\beta}(\tau') + X_\sigma^{\beta\alpha}(\tau) X_{\sigma'}^{\beta\alpha}(\tau') \Big], \end{aligned} \tag{74}$$

with $X_\sigma^{\alpha\beta} = c_{\alpha,\sigma}^\dagger c_{\beta,\sigma}$ and retarded density-density interaction and Hund coupling parameters.

A possible algorithm based on a double-expansion in the hybridization and Hund coupling has recently been presented in Ref. [97]. The full problem with retarded spin-flips and

pair-hoppings however suffers from a sign problem, so that in practice it seems necessary to treat these operators as instantaneous and keep the retardation only in the density-density component. Note that even the simulation of such a simplified model requires a double-expansion approach. To illustrate this, let us consider an on-site electron-boson coupling term of the form $H_{\text{el-b}} = \sum_{\alpha,\lambda} g_{\alpha,\lambda} n_\alpha (b^\dagger_\lambda + b_\lambda)$ and the multi-orbital and multi-boson version of the Lang-Firsov transformation (48), (49): $\tilde{d}^\dagger_{\alpha,\sigma} = e^{\sum_\lambda \frac{g_{\alpha,\lambda}}{\omega_\lambda}(b^\dagger_\lambda - b_\lambda)} d^\dagger_{\alpha,\sigma}$, $\tilde{d}_{\alpha,\sigma} = e^{-\sum_\lambda \frac{g_{\alpha,\lambda}}{\omega_\lambda}(b^\dagger_\lambda - b_\lambda)} d_{\alpha,\sigma}$. This transformation leaves density operators unchanged, $\tilde{n}_\alpha = n_\alpha$, while a pair hopping operator $d^\dagger_{\alpha,\uparrow} d^\dagger_{\alpha,\downarrow} d_{\beta\uparrow} d_{\beta,\downarrow}$ acquires a factor $e^{\sum_\lambda \frac{2(g_{\alpha,\lambda} - g_{\beta,\lambda})}{\omega_\lambda}(b^\dagger_\lambda - b_\lambda)}$, which for example in the case of a Jahn-Teller coupling ($g_\alpha = -g_\beta$) is nonzero. Hence, we cannot keep such non-density-density terms in the time-evolution operators, but need to expand in them.

IV. TOWARDS A SELF-CONSISTENT DESCRIPTION OF SCREENING

In the previous sections, we have discussed the cRPA technique for computing low-energy effective models for correlated materials, and different approximate and exact schemes for treating the resulting dynamically screened interactions within DMFT. We also mentioned the fact that the elimination of low-energy screening processes in cRPA generically leads to rather long-ranged interactions. In this section, we would like to improve the DMFT description by (i) including the screening effect from long-ranged Coulomb interactions, and (ii) considering nonlocal correlations. First, we will focus on the single orbital extended Hubbard model (Sec. IV A), which allows us to introduce these advanced schemes in the simplest possible set-up, and then discuss how some of these techniques can be implemented in an *ab initio* context (Sec. IV B). The goal is to provide a self-consistent description of screening and correlations within the low-energy window defined by the cRPA downfolding, and in the future perhaps even within a larger window containing some of the screening bands.

A. U-V Hubbard model

1. *Extended DMFT*

The screening from nonlocal Coulomb interactions can be described by the so-called extended DMFT (EDMFT) formalism [94, 98–100]. This method is still based on an effective single-site impurity model, but involves two self-consistently computed dynamical mean fields: the Weiss Green's function $\mathcal{G}_0(i\omega_n)$ (or hybridization function $\Delta(i\omega_n)$), which controls the hopping of electrons in and out of the impurity site, and the dynamical on-site interaction $\mathcal{U}(i\nu_n)$, which incorporates the effect of screening. While $\mathcal{G}_0$ is β-antiperiodic, $\mathcal{U}$ is β-periodic. We denote the fermionic Matsubara frequencies by ω_n and the bosonic Matsubara frequencies by ν_n.

For simplicity, we derive the EDMFT formalism for the U-V Hubbard model

$$H_{\text{UV-Hubbard}} = -t\sum_{\langle ij\rangle\sigma}(d^\dagger_{i\sigma}d_{j\sigma} + d^\dagger_{j\sigma}d_{i\sigma}) - \mu\sum_{i\sigma} n_{i\sigma} + U\sum_i n_{i\uparrow}n_{i\downarrow} + \frac{V}{2}\sum_{\langle ij\rangle} n_i n_j, \tag{75}$$

with $n_i = n_{i\uparrow} + n_{i\downarrow}$. Here, we assume that the hoppings and off-site interactions are between nearest-neighbor sites, although the generalization to arbitrary hoppings and longer range interactions is straightforward. We furthermore take the bare interactions U and V as static. If the U-V Hubbard model is a low-energy effective theory derived from some downfolding procedure, then these bare parameters can themselves have a frequency-dependence. Again, the generalization of the following formalism to the case of frequency-dependent bare interactions is straightforward, and merely involves the replacement of U by $U(\tau)$ or $U(i\nu_n)$ and similarly for V.

We start by writing the action of the lattice model in terms of Grassmann fields d^*, d as

$$S = \int_0^\beta d\tau\Big[\sum_{ij\sigma} d^*_{i\sigma}(\tau)((\partial_\tau - \mu)\delta_{ij} + t_{ij})d_{j\sigma}(\tau) + U\sum_i n_{i\uparrow}(\tau)n_{i\downarrow}(\tau) + \frac{1}{2}\sum_{ij} v_{ij}n_i(\tau)n_j(\tau)\Big] \tag{76}$$

$$= \int_0^\beta d\tau\Big[\sum_{ij\sigma} d^*_{i\sigma}(\tau)((\partial_\tau - \tilde{\mu})\delta_{ij} + t_{ij})d_{j\sigma}(\tau) + \frac{1}{2}\sum_{ij}\tilde{v}_{ij}n_i(\tau)n_j(\tau)\Big]. \tag{77}$$

In the second expression, we have written the interaction contributions in terms of $\tilde{v}_{ij} = U\delta_{ij} + v_{ij}$, and shifted the chemical potential as $\tilde{\mu} = \mu + \frac{U}{2}$. Note that for the U-V Hubbard model, $t_{ij} = -t\delta_{\langle ij\rangle}$ and $v_{ij} = V\delta_{\langle ij\rangle}$, but it is more convenient to use the general notation.

Since we want to map the lattice model onto a single-site impurity model, we next decouple the interaction term by a Hubbard-Stratonovich transformation, thereby replacing the (on-site and off-site) interaction by a local coupling to a real, β-periodic field ϕ [101]:

$$\exp\left[-\frac{1}{2}\int_0^\beta d\tau \sum_{ij} n_i(\tau)\tilde{v}_{ij}n_j(\tau)\right] = ((2\pi)^N \det v)^{-1/2} \int \mathcal{D}[\phi_1,\ldots,\phi_N] \times \exp\left[-\int_0^\beta d\tau\Big\{\frac{1}{2}\sum_{ij}\phi_i(\tau)(\tilde{v}^{-1})_{ij}\phi_j(\tau) + i\sum_j \phi_j(\tau)n_j(\tau)\Big\}\right]. \quad (78)$$

After this decoupling, the action of the lattice model can be written as

$$S = \int_0^\beta d\tau\Big[-\sum_{ij\sigma} d^*_{i\sigma}(\tau)(G_0^{-1})_{ij}d_{j\sigma}(\tau) + \frac{1}{2}\sum_{ij}\phi_i(\tau)(\tilde{v}^{-1})_{ij}\phi_j(\tau) + i\sum_j \phi_j(\tau)n_j(\tau)\Big], \quad (79)$$

where we have introduced the inverse of the noninteracting lattice Green's function, $(G_0^{-1})_{ij} = ((-\partial_\tau + \tilde{\mu})\delta_{ij} - t_{ij})$ to simplify the first term. In EDMFT, this lattice model is self-consistently mapped onto an impurity model with action

$$S^\phi_{\mathrm{EDMFT}} = -\int_0^\beta d\tau d\tau' \sum_\sigma d^*_\sigma(\tau)\mathcal{G}^{-1}(\tau-\tau')d_\sigma(\tau') + \frac{1}{2}\int_0^\beta d\tau d\tau' \phi(\tau)\mathcal{U}^{-1}(\tau-\tau')\phi(\tau') + i\int_0^\beta d\tau\phi(\tau)n(\tau). \quad (80)$$

A detailed derivation can be found in Refs. [100] and [94]. For the present purpose it suffices to note that in addition to the fermionic Weiss field $\mathcal{G}$, there also appears a β-periodic Weiss field $\mathcal{U}$, which has to be adjusted in such a way that the local dynamics of the Hubbard-Stratonovich field is well reproduced. In the self-consistency loop, one computes the impurity Green's functions

$$G_{\mathrm{imp}} = -\langle \mathcal{T} d(\tau)d^*(0)\rangle_{S_{\mathrm{EDMFT}}}, \quad (81)$$

$$W_{\mathrm{imp}} = \langle \mathcal{T}\phi(\tau)\phi(0)\rangle_{S_{\mathrm{EDMFT}}}, \quad (82)$$

and identifies them with the corresponding local lattice Green's functions $G^{\mathrm{latt}}_{i,i} = -\langle \mathcal{T} d_i(\tau)d_i^*(0)\rangle_{S_{\mathrm{latt}}}$ and $W^{\mathrm{latt}}_{i,i} = \langle \mathcal{T}\phi_i(\tau)\phi_i(0)\rangle_{S_{\mathrm{latt}}}$, where the latter are computed using a local approximation for the lattice self-energies Σ and P:

$$\Sigma(\mathbf{k}, i\omega_n) \approx \Sigma_{\mathrm{imp}}(i\omega_n), \quad \Sigma_{\mathrm{imp}}(i\omega_n) = \mathcal{G}^{-1}(i\omega_n) - G_{\mathrm{imp}}(i\omega_n), \quad (83)$$

$$P(\mathbf{k}, i\nu_n) \approx P_{\mathrm{imp}}(i\nu_n), \quad P_{\mathrm{imp}}(i\nu_n) = \mathcal{U}^{-1}(i\nu_n) - W_{\mathrm{imp}}(i\nu_n). \quad (84)$$

Physically, $P(\mathbf{k}, i\nu_n)$ ($P_{\rm imp}(i\nu_n)$) represents the lattice (impurity) polarization. For the actual calculations, it is convenient to integrate out the ϕ-field from the impurity action (80), to obtain

$$S_{\rm EDMFT} = -\int_0^\beta d\tau d\tau' \sum_\sigma d^*_\sigma(\tau)\mathcal{G}^{-1}(\tau-\tau')d_\sigma(\tau') + \frac{1}{2}\int_0^\beta d\tau d\tau' n(\tau)\mathcal{U}(\tau-\tau')n(\tau') - \frac{1}{2}\mathrm{Tr}\ln\mathcal{U}. \quad (85)$$

This impurity problem with retarded density-density interaction can be solved for example using the hybridization expansion Monte Carlo method discussed in Sec. III B 3. While the fermionic Green's function (81) can be measured directly, the evaluation of the bosonic Green's function (82) requires an intermediate step. From Eq. (80) it follows that $\frac{\delta \ln Z}{\delta \mathcal{U}^{-1}} = -2\mathcal{U}\frac{\delta \ln Z}{\delta \mathcal{U}}\mathcal{U}$, while Eq. (85) implies $\frac{\delta \ln Z}{\delta \mathcal{U}} = \frac{1}{2}\langle \mathcal{T} n(\tau)n(0)\rangle_{S_{\rm EDMFT}} - \frac{1}{2\mathcal{U}}$. Combining the two expressions yields the measurement formula

$$W_{\rm imp} = \mathcal{U} - \mathcal{U}\chi_{\rm loc}\mathcal{U}, \quad \chi_{\rm loc} = \langle \mathcal{T} n(\tau)n(0)\rangle_{S_{\rm EDMFT}}. \quad (86)$$

The density density correlation function $\chi_{\rm loc}$ can be easily evaluated in the hybridization expansion Monte Carlo method discussed in Sec. III B 3.

The fermionic self-consistency loop in an EDMFT calculation is identical to usual DMFT:

1. Compute $G_{\rm imp}(i\omega_n)$ for the given $S_{\rm EDMFT}$,
2. Extract fermionic self-energy: $\Sigma_{\rm imp}(i\omega_n) = \mathcal{G}_0^{-1}(i\omega_n) - G_{\rm imp}^{-1}(i\omega_n)$,
3. Use DMFT approximation $\Sigma(\mathbf{k}, i\omega_n) = \Sigma_{\rm imp}(i\omega_n)$ to compute the local lattice Green's function $G_{\rm loc}(i\omega_n) = \int (d\mathbf{k})[(G_0)^{-1} - \Sigma_{\rm imp}(i\omega_n)]^{-1}$,
4. Use DMFT self-consistency condition $G_{\rm loc}(i\omega_n) = G_{\rm imp}(i\omega_n)$ to define a new Weiss Green's function $\mathcal{G}_0^{-1}(i\omega_n) = G_{\rm loc}^{-1}(i\omega_n) + \Sigma_{\rm imp}(i\omega_n)$,

while the bosonic self-consistency loop is analogous,

1. Compute $W_{\rm imp}(i\nu_n)$ for the given $S_{\rm EDMFT}$ (Eq. (86)),
2. Extract bosonic self-energy: $P_{\rm imp}(i\nu_n) = \mathcal{U}^{-1}(i\nu_n) - W_{\rm imp}^{-1}(i\nu_n)$,
3. Use DMFT approximation $P(\mathbf{k}, i\nu_n) = P_{\rm imp}(i\nu_n)$ to compute the local lattice Green's function $W_{\rm loc}(i\nu_n) = \int (d\mathbf{k})[\frac{1}{2}(\tilde{v})^{-1} - P_{\rm imp}(i\nu_n)]^{-1}$,

4. Use DMFT self-consistency condition $W_{\rm loc}(i\nu_n) = W_{\rm imp}(i\nu_n)$ to define a new retarded interaction $\mathcal{U}^{-1}(i\nu_n) = W_{\rm loc}^{-1}(i\nu_n) + P_{\rm imp}(i\nu_n)$.

In an EDMFT calculation, these two loops are typically solved in parallel, i.e., both the Weiss Green's function $\mathcal{G}$ and the retarded interaction $\mathcal{U}$ is updated before the next impurity calculation is started. We finally remark that in the case of frequency dependent U and V, the bosonic Dyson equation which allows to update $W_{\rm loc}$ from $P_{\rm imp}$ will have frequency dependent $(\tilde{v})^{-1}$. Therefore, retarded U and V are readily included in this framework, as already mentioned before.

2. GW+DMFT

We next discuss the implementation of the GW+DMFT method for the U-V Hubbard model (75), for which fully self-consistent calculations have recently been implemented [94, 102, 103]. GW+DMFT is based on the EDMFT framework, but involves momentum dependent fermionic and bosonic self-energies, which are obtained by combining the (local) EDMFT self-energies with the nonlocal components of the GW self-energies:

$$\Sigma_{jk}^{\rm GW+DMFT}(i\omega_n) = \Sigma_{jj}^{\rm EDMFT}(i\omega_n)\delta_{jk} + \Sigma_{jk}^{GW}(i\omega_n)(1-\delta_{jk}), \tag{87}$$

$$P_{jk}^{\rm GW+DMFT}(i\nu_n) = P_{jj}^{\rm EDMFT}(i\nu_n)\delta_{jk} + P_{jk}^{GW}(i\nu_n)(1-\delta_{jk}). \tag{88}$$

We note that this is not the only combination which avoids a double counting of self-energy diagrams. In fact, the subtraction of all the local GW diagrams also removes contributions (e. g. with nonlocal polarization bubbles) which are not accounted for in the EDMFT self-energy. An alternative strategy would be to remove the subset of GW diagrams which contains only local propagators: $\Sigma_{jk}^{\rm GW+DMFT}(i\omega_n) = \Sigma_{jj}^{\rm EDMFT}(i\omega_n)\delta_{jk} + \Sigma_{jk}^{GW}(i\omega_n) - \Sigma_{jj}^{GW}[G_{ii}](i\omega_n)\delta_{jk}$, and similarly for P. In the case of the two-dimensional Hubbard model in the weak-coupling regime, both double counting corrections were found to produce similar results [22], but in more general situations, the effect of different double counting schemes has not yet been studied systematically.

The computational steps in the self-consistent GW+DMFT calculation are the following:

1. Start, e. g., from the converged EDMFT solution ($\Sigma_{\rm imp}(i\omega_n)$, $P_{\rm imp}(i\nu_n)$), and define approximate lattice self-energies:

$$\Sigma(\mathbf{k}, i\omega_n) = \Sigma_{\rm imp}(i\omega_n), \quad P(\mathbf{k}, i\nu_n) = P_{\rm imp}(i\nu_n), \tag{89}$$

2. Update the lattice Green's functions:

$$G(\mathbf{k}, i\omega_n) = [G_0^{-1}(\mathbf{k}, i\omega_n) - \Sigma(\mathbf{k}, i\omega_n)]^{-1}, \tag{90}$$

$$W(\mathbf{k}, i\nu_n) = [\tfrac{1}{2}\tilde{v}(\mathbf{k})^{-1} - P(\mathbf{k}, i\nu_n)]^{-1}, \tag{91}$$

3. Compute the local lattice Green's functions and the new Weiss fields $\mathcal{G}_0$ and $\mathcal{U}$:

$$G_{\rm loc}(i\omega_n) = \int (d\mathbf{k}) G(\mathbf{k}, i\omega_n) \quad \rightarrow \quad \mathcal{G}_0^{-1}(i\omega_n) = G_{\rm loc}(i\omega_n)^{-1} + \Sigma_{\rm imp}(i\omega_n), \tag{92}$$

$$W_{\rm loc}(i\nu_n) = \int (d\mathbf{k}) W(\mathbf{k}, i\nu_n) \quad \rightarrow \quad \mathcal{U}^{-1}(i\nu_n) = W_{\rm loc}(i\nu_n)^{-1} + P_{\rm imp}(i\nu_n), \tag{93}$$

4. Solve the impurity problem, i.e. compute $G_{\rm imp}$ and $\chi_{\rm loc} \rightarrow W_{\rm imp} = \mathcal{U} - \mathcal{U}\chi_{\rm loc}\mathcal{U}$. Compute the fermionic and bosonic self-energies

$$\Sigma_{\rm imp}(i\omega_n) = \mathcal{G}_0^{-1}(i\omega_n) - G_{\rm imp}^{-1}(i\omega_n), \tag{94}$$

$$P_{\rm imp}(i\nu_n) = \mathcal{U}^{-1}(i\nu_n) - W_{\rm imp}^{-1}(i\nu_n), \tag{95}$$

5. Calculate the GW+DMFT self-energies:

   - Calculate the GW self-energies,

$$\Sigma^{GW}(\mathbf{k}, i\omega_n) = -\frac{T}{N_{\mathbf{k}}} \sum_{\mathbf{q}} \sum_{\nu_m} G(\mathbf{q}, i\omega_n - i\nu_m) W(\mathbf{k}-\mathbf{q}, i\nu_m), \tag{96}$$

$$P^{GW}(\mathbf{k}, i\nu_n) = 2\frac{T}{N_{\mathbf{k}}} \sum_{\mathbf{q}} \sum_{\omega_m} G(\mathbf{q}, i\omega_m) G(\mathbf{q}-\mathbf{k}, i\omega_m - i\nu_n), \tag{97}$$

   - Extract the nonlocal parts,

$$\Sigma^{GW}_{\rm nonlocal}(\mathbf{k}, i\omega_n) = \Sigma^{GW}(\mathbf{k}, i\omega_n) - \int (d\mathbf{k}) \Sigma^{GW}(\mathbf{k}, i\omega_n), \tag{98}$$

$$P^{GW}_{\rm nonlocal}(\mathbf{k}, i\nu_n) = P^{GW}(\mathbf{k}, i\nu_n) - \int (d\mathbf{k}) P^{GW}(\mathbf{k}, i\nu_n), \tag{99}$$

   - Combine GW and EDMFT self-energies

$$\Sigma(\mathbf{k}, i\omega_n) = \Sigma_{\rm imp}(i\omega_n) + \Sigma^{GW}_{\rm nonlocal}(\mathbf{k}, i\omega_n), \tag{100}$$

$$P(\mathbf{k}, i\nu_n) = P_{\rm imp}(i\nu_n) + P^{GW}_{\rm nonlocal}(\mathbf{k}, i\nu_n), \tag{101}$$

6. Go back to (ii) until convergence is reached.

Note that the GW self-energy defined in Eq. (96) contains a Hartree contribution involving the bare local interaction. This contribution is however removed in the definition of $\Sigma^{GW}_{\rm nonlocal}$ (Eq. (98)).

An interesting question is how accurately the GW+DMFT method captures the momentum and energy dependence of the nonlocal self-energies. While a complete picture is lacking, some systematic tests against numerically exact diagrammatic Monte Carlo results [104] have recently been performed for the two-dimensional square-lattice Hubbard model in the weak-coupling regime [22]. It was shown that the DMFT approximation provides a very good description of $\Sigma_{\rm loc}(i\omega_n)$, and that the GW+DMFT result is of comparable accuracy (Fig. 7). While the nonlocal components are of the correct order of magnitude in the weak-coupling regime, their relative errors are large. Apparently, the GW approximation does not capture the correct momentum dependence at weak U and away from half-filling, and the result can only be expected to get worse in the intermediate coupling regime and closer to half-filling. In particular, GW+DMFT does not reproduce the strong differentiation between node and antinode which is found in cluster DMFT simulations [18, 19] in the intermediate coupling regime. Figure 7 also shows the comparison to alternative many-body perturbation theory + DMFT schemes, namely the bare second order perturbation theory ($\Sigma^{(2)}$) + DMFT [100] and the fluctuation exchange approximation (FLEX) + DMFT methods. They are of similar accuracy, but also fail to correctly capture the nonlocal components. $\Sigma^{(2)}$+DMFT at least ensures the correct high-frequency behavior of the local self-energy.

While GW+DMFT produces rather poor results for the momentum dependence of the two-dimensional Hubbard model, it should be kept in mind that (i) DMFT based methods are by construction most appropriate for high-dimensional systems, and (ii) that the main advantage of the GW+DMFT lies in the self-consistent description of the screening, and thus in the possibility to self-consistently compute the appropriate "Hubbard-U" parameters in an *ab initio* simulation.

Finally, let us note that the factor of two in the GW polarization (97) comes from the sum over spin orientations. For the Hubbard model, with its spin-dependent instantaneous on-site interaction, the RPA polarization diagrams should in fact only include odd numbers of bubbles with alternating spin. To avoid unphysical diagrams, one should implement a spin-dependent GW formalism, which involves 2×2 matrices in spin space. While the polarization P is diagonal, the Hubbard interaction becomes an off-diagonal matrix $U\sigma_x$.

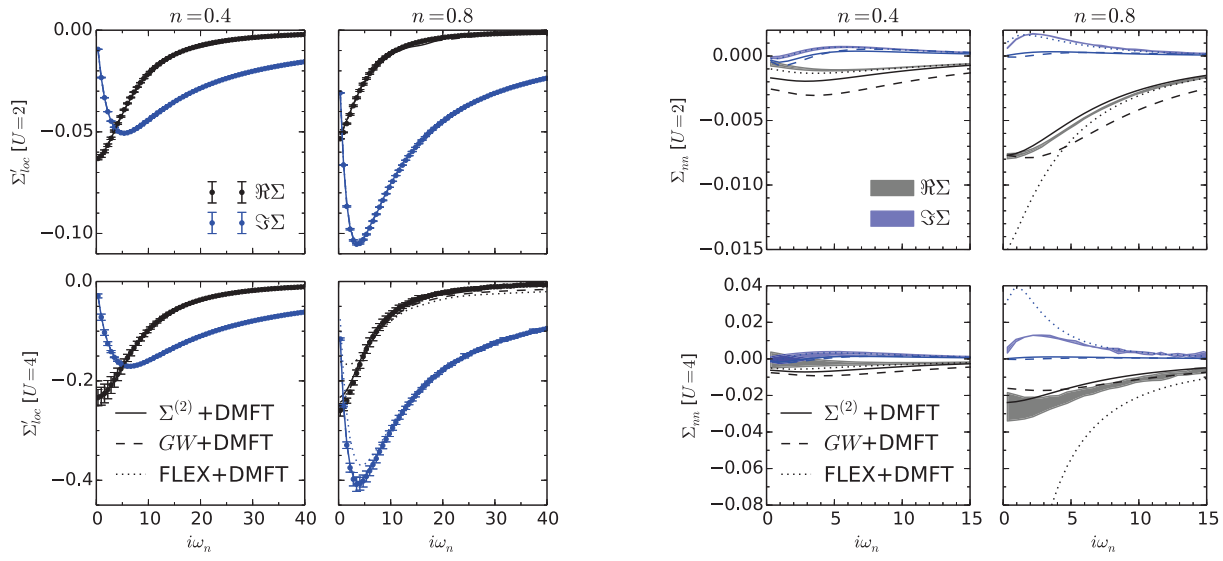


FIG. 7: Comparison of the local and nonlocal self-energies from different many-body perturbation theory + DMFT approximations to the numerically exact diagrammatic Monte Carlo results for the square lattice Hubbard model with bandwidth 8. The left panels show the imaginary part of the local self-energy for indicated values of the interaction U and filling n. The error bars are estimated from different cutoff orders in the diagrammatic sampling. The right panels show the imaginary part of the non-local self-energy for nearest neighbor sites, with the gray and blue shaded bands corresponding to the diagrammatic Monte Carlo result. Note the much smaller y-axis scale compared to the left panels. (From Ref. [22].)

Therefore, in a spin-dependent GW calculation for the Hubbard model, the self-energy Σ is constructed with the following diagonal element of the screened interaction:

$$W_{\sigma\sigma}(\mathbf{k}, i\nu_n) = \frac{U^2 P(\mathbf{k}, i\nu_n)}{1 - [UP(\mathbf{k}, i\nu_n)]^2}. \tag{102}$$

Systematic tests of the spin-dependent and spin-independent GW schemes for the two-dimensional Hubbard model [22] have shown that the spin-dependent formulation indeed cures the most obvious deficiencies of the spin-independent scheme. However, in models with nonlocal interactions and realistic material simulations within GW or GW+DMFT, this issue becomes less relevant.

3. Dual boson

The dual boson formalism [105, 106] is a systematic extension of EDMFT, which incorporates momentum-dependent correlations and enables a consistent description of collective excitations. This method is still under active development, so we will content ourselves here with a sketch of the main ideas, and references to the original papers, where the mathematical details can be found. As in the previous sections, we will consider the U-V Hubbard model and start the discussion by rewriting the Grassmann path-integral for the lattice action (77) in the Matsubara formalism:

$$\begin{aligned} S = &- T \sum_{j\omega_n\sigma} d^*_{j\sigma}(i\omega_n)[i\omega_n + \tilde{\mu}] d_{j\sigma}(i\omega_n) + T \sum_{\langle jl\rangle\omega_n\sigma} t_{jl} d^*_{j\sigma}(i\omega_n) d_{l\sigma}(i\omega_n) \\ &+ \frac{UT}{2} \sum_{j\nu_n} n_j(i\nu_n) n_j(i\nu_n) + \frac{VT}{2} \sum_{\langle jl\rangle\nu_n} n_j(-i\nu_n) n_l(i\nu_n), \end{aligned} \tag{103}$$

where the angular brackets denote the sum over nearest neighbors, and we have split $\tilde{v}_{ij} = U\delta_{ij} + V\delta_{\langle ij\rangle}$ into the on-site and nearest-neighbor contributions. We next rewrite Eq. (103) as a sum of EDMFT-type impurity actions and a rest

$$S = \sum_j S_{\mathrm{imp},j} + S_{\mathrm{rest}}, \tag{104}$$

$$S_{\mathrm{imp}} = -T \sum_{\omega_n\sigma} d^*_\sigma(i\omega_n)[i\omega_n + \tilde{\mu} - \Delta_\sigma(i\omega_n)] d_\sigma(i\omega_n) + \frac{T}{2} \sum_{\nu_n} n(i\nu_n)[U + D(i\nu_n)] n(i\nu_n), \tag{105}$$

with at this stage an unspecified hybridization function Δ and retarded interaction D (see illustration in Fig. 8). In the next step, S_{rest}, which contains hopping and hybridization terms, the nonlocal interactions and a local retarded interaction, is decoupled using Hubbard-Stratonovich transformations. The decoupling of the interactions is analogous to EDMFT (Eq. (78)) and introduces the bosonic fields ϕ_j, which in the present context are called 'dual bosons'. At the same time, the fermionic hopping and hybridization terms in S_{rest} are decoupled by an appropriate Hubbard-Stratonovich transformation, which introduces auxiliary fermions f_j, called 'dual fermions' [107], and replaces the nonlocal quadratic term in the d-operators by a local coupling between d- and f-fermions (see bottom right panel of Fig. 8). In the final step, the d-electrons are integrated out, which generates a dual action for the f and ϕ variables, with a complicated interaction $\tilde{V}(f_j, f^*_j, \phi_j)$, which can be related to (high-order) vertices of the impurity model S_{imp}. The explicit form of the dual action is

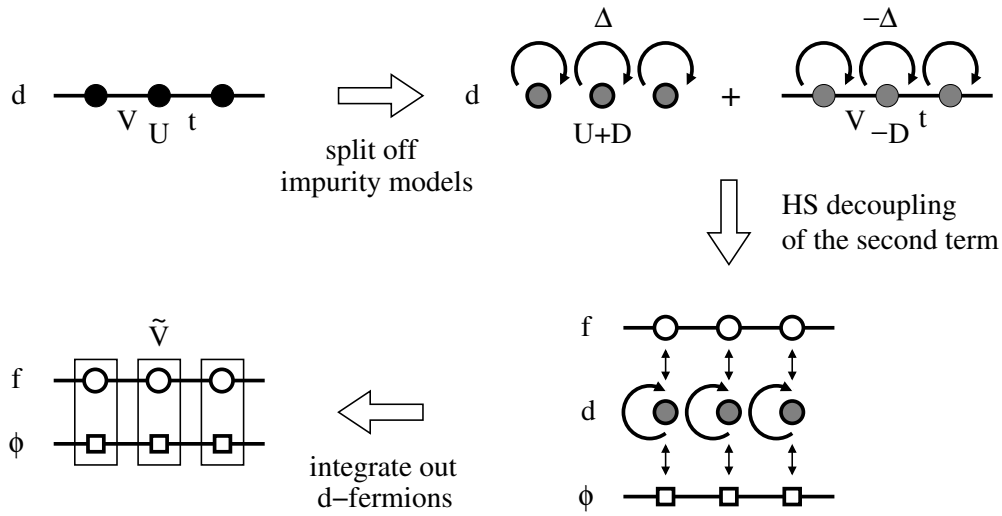


FIG. 8: Illustration of the dual boson formalism. In the first step, the lattice model is split into a collection of impurity models with retarded interaction D and a rest. In the second step, the rest term is decoupled by Hubbard-Stratonovich transformations, which introduce a local coupling to dual fermions (f) and dual bosons (ϕ). In the last step, the original d-fermions are integrated out, which yields a dual theory with an interaction $\tilde{V}$, which is of arbitrary order in f, f^* and ϕ.

$$\tilde{S} = -T \sum_{\mathbf{k}\omega_n\sigma} f^*_{\mathbf{k}\sigma}(i\omega_n)\tilde{\mathcal{G}}^{-1}_{0,\mathbf{k}\sigma}(i\omega_n) f_{\mathbf{k}\sigma}(i\omega_n) - \frac{T}{2}\sum_{\mathbf{k}\nu_n} \phi_{\mathbf{k}}(i\nu_n)\tilde{\mathcal{X}}^{-1}_{0,\mathbf{k}}(i\nu_n)\phi_{\mathbf{k}}(i\nu_n) + \sum_j \tilde{V}(f_j, f^*_j, \phi_j), \tag{106}$$

where the bare dual propagators, expressed in terms of the impurity Green's function $g(i\omega_n) = -\langle d^*(i\omega_n) d(i\omega_n)\rangle_{S_{\rm imp}}$ and impurity charge susceptibility $\chi(i\nu_n) = -\langle n(i\nu_n) n(-i\nu_n)\rangle_{S_{\rm imp}}$ are [106]

$$\tilde{\mathcal{G}}_{0,\mathbf{k}\sigma}(i\omega_n) = [g^{-1}(i\omega_n) + \Delta(i\omega_n) - \epsilon_{\mathbf{k}}]^{-1} - g(i\omega_n), \tag{107}$$

$$\tilde{\mathcal{X}}_{0,\mathbf{k}}(i\nu_n) = [\chi(i\nu_n)^{-1} + D(i\nu_n) - V_{\mathbf{k}}]^{-1} - \chi(i\nu_n), \tag{108}$$

with $\epsilon_{\mathbf{k}}$ and $V_{\mathbf{k}}$ the Fourier transforms of the hopping and nearest neighbor interaction.

The dual action (106) is treated in perturbation theory, where in practice one only retains low-order or ladder-type diagrams in $\tilde{V}$. The main idea is to exploit the freedom of choosing $\Delta(i\omega_n)$ and $D(i\nu_n)$, and to define these quantities in such a way that the strong correlation

effects are captured at the level of the impurity model $S_{\rm imp}$, which can be solved exactly using the technique described in Sec. III B 3, so that only weaker correlations must be treated by the dual perturbation theory. For example, the EDMFT solution can be incorporated as the zeroth order of this dual perturbation theory, in which case the dual boson formalism becomes a systematic expansion around EDMFT. Better choices for Δ and D, which take into account a feedback from the lattice solution onto the impurity problem may exist, as has been recently discussed in Ref. [106].

From the dual perturbation theory, one obtains a dual self-energy $\tilde{\Sigma}_{\mathbf{k}}(i\omega_n)$ and a dual polarization $\tilde{P}_{\mathbf{k}}(i\nu_n)$. These can then be used to obtain the lattice Green's function $G_{\mathbf{k}}(i\omega_n)$ and lattice susceptibility $\mathcal{X}_{\mathbf{k}}(i\nu_n)$ of the original d-fermions:

$$G^{-1}_{\mathbf{k}}(i\omega_n) = [g(i\omega_n) + g(i\omega_n)\tilde{\Sigma}_{\mathbf{k}}(i\omega_n)g(i\omega_n)]^{-1} + \Delta(i\omega_n) - \epsilon_{\mathbf{k}}, \tag{109}$$

$$\mathcal{X}^{-1}_{\mathbf{k}}(i\nu_n) = [\chi(i\nu_n) + \chi(i\nu_n)\tilde{P}_{\mathbf{k}}(i\nu_n)\chi(i\nu_n)]^{-1} + D(i\nu_n) - V_{\mathbf{k}}. \tag{110}$$

While an appropriately formulated dual boson theory is self-consistent both on the single-particle and two-particle level [106], in contrast to GW+DMFT, this appealing feature comes at the cost of having to calculate and manipulate vertex functions. This makes it challenging to apply this formalism to realistic multiband systems.

B. Realistic materials

1. *GW+DMFT*

The full implementation of the GW+DMFT scheme as proposed in Ref. [10] is doable in practice only for simple Hamiltonians, such as the U-V extended Hubbard model discussed above. This represents already a significant step forward with respect to the situation just a few years ago, when only *static* and *non-self-consistent* GW+DMFT applications had been performed. The methods which allow to treat the dynamically screened nature of $\mathcal{U}$, inherent in the GW+DMFT formalism, and to determine it self-consistently in some particular cases, have been discussed in Secs. III B and III C. However, in an *ab initio* framework, the local dynamical impurity problem is too large to be solved in a reasonable computer time. Indeed, the local basis set of an *ab initio* Hamiltonian can be very large, and in the genuine GW+DMFT formulation *all* local orbitals should be taken into account

in the embedded site, as they all contribute to the screening of the effective local interaction $\mathcal{U}$.

A practical GW+DMFT implementation recently introduced is the so-called "orbital-separated" scheme, where only the correlated orbitals are kept in the impurity problem, whose size becomes then manageable by state-of-the-art CTQMC solvers, provided the low energy model is a single-site multiorbital system, and not a cluster. On one hand, it is reasonable to include only the most correlated orbitals in the impurity problem. On the other hand, separating the self-energy contribution of the local, correlated manifold from the non-local *or* non-correlated one has no unique solution, as there is no rigorous free energy functional which generates this separation unambiguously, as discussed in Ref. [108]. Therefore, in defining the local self energy, one needs to make an *ad hoc* choice. The one which seems the most general is

$$\Sigma^{\mathrm{xc}}(\mathbf{k}, i\omega_n)_{LL'} = \Sigma^{\mathrm{xc}}_{GW}(\mathbf{k}, i\omega_n)_{LL'} - \sum_{\mathbf{k}} [\Sigma^{\mathrm{xc},d}_{GW}(\mathbf{k}, i\omega_n)]_{LL'} + [\Sigma^{\mathrm{xc},d}_{\mathrm{imp}}(i\omega_n)]_{LL'}, \tag{111}$$

where L is the full-orbital index, and d denotes the projection onto the low-energy correlated space. The corresponding equation for the total polarization is

$$P(\mathbf{k}, i\nu_n)_{\alpha\beta} = P_{GW}(\mathbf{k}, i\nu_n)_{\alpha\beta} - \sum_{\mathbf{q}} [P^{d}_{GW}(\mathbf{k}, i\nu_n)]_{\alpha\beta} + [P^{d}_{\mathrm{imp}}(i\nu_n)]_{\alpha\beta}, \tag{112}$$

where α and β are indices of a two-particle basis, constructed from the full one-body basis set L. Equations (111) and (112) are analogous to Eqs. (87) and (88), written for the GW+DMFT calculation of the U-V Hubbard model. $\Sigma^{\mathrm{xc},d}_{\mathrm{imp}}$ and P^{d}_{imp} are the (fermionic) self-energy and polarization (bosonic self-energy) computed as solutions of the impurity problem in the correlated local basis (see the extended DMFT description in Sec. IV A 1). From $\Sigma^{\mathrm{xc}}(\mathbf{k}, i\omega_n)_{LL'}$ and $P(\mathbf{k}, i\nu_n)_{\alpha\beta}$ one obtains the dressed Green's function $G(\mathbf{k}, i\omega_n)_{LL'}$ and the fully screened interaction $W(\mathbf{k}, i\nu_n)_{\alpha\beta}$ by standard procedures. As in step (ii) of the GW+DMFT loop in Sec. IV A 2, one then computes the "Weiss" fields $\mathcal{G}_0$ and $\mathcal{U}$, after projection of the local G^{loc} and W^{loc} onto d. Thus, the orbital-separated framework follows the usual GW+DMFT self-consistency loop, where the non-perturbative many-body solution is provided only in a correlated subspace, and the convergence is reached when the local lattice Green's function and polarization projected to the correlated subspace become identical to the impurity Green's function and impurity polarization, respectively.

Significant effort has also been devoted to the development of simplified and numerically more efficient approaches, based on some approximations. On the one hand, the double self-consistency in the Green's function and polarization has been replaced by only one based on the Green's function. In these calculations, the polarization is frozen to the cRPA value, but the corresponding retarded interaction is kept in the impurity problem. This approximate scheme is detailed in Sec. IV B 2. On the other hand, a series of approximations has been proposed, which simplify the frequency *and* spatial dependence of the GW self-energy, which is one of the heaviest ingredients to compute. We will give a short survey of these simplified methods, which in order of increasing complexity are (i) SEX+DMFT (Sec. IV B 3), (ii) DMFT@nonlocal-GW (Sec. IV B 4), and (iii) quasi-particle self-consistent GW (QSGW) + DMFT (Sec. IV B 5).

2. *Frozen polarization: $\mathcal{U}$ replaced by the cRPA $U(\omega)$*

Instead of computing explicitly $P_{\rm imp}$ to update the bosonic Weiss field $\mathcal{U}$ at each GW+DMFT iteration, one can approximate it by its RPA value, i.e. $P_{\rm imp} = 2G^{\rm loc,d}G^{\rm loc,d}$, with $G^{\rm loc,d}$ the local starting Green's function, taken from LDA and projected onto the correlated manifold [108, 109]. Therefore, the total polarization in Eq. (112) can be written as $P = 2G_{\rm LDA}G_{\rm LDA}$. Its value is frozen during the self-consistency cycle, which is performed only on G. This also implies that the interaction $\mathcal{U}$ of the impurity model is frozen. Moreover, instead of evaluating this interaction as $\mathcal{U}^{-1}(i\nu_n) = W_{\rm loc}(i\nu_n)^{-1} + P_{\rm imp}(i\nu_n)$ (step (ii) of the GW+DMFT loop), which involves *local* quantities only, $\mathcal{U}$ is calculated as

$$\mathcal{U} = \left[\sum_q [W^{-1} + P^d]^{-1}\right]_d , \tag{113}$$

where W is the fully screened interaction. Hence, W is undressed by P^d, which is the RPA polarization function containing electron-hole processes in the d manifold only. Note that the "locality" operation ($\sum_q$) is performed after undressing W, and the matrix is projected onto the d-manifold only at the end. Equation (113) is the partially screened cRPA value of $U_{mn}(\mathbf{0},\omega)$ in Eq. (4), where n, m are indices of the d subspace. Therefore, in this approach, $\mathcal{U}$ is kept fixed at the cRPA value. At a first glance, this might seem a very rough approximation, with respect to the double loop on G and W. However, if compared to available electron energy loss spectroscopy (EELS) measurements, the RPA polarization

function computed from the LDA band structure looks usually reasonable. This suggests that the cRPA estimate of $\mathcal{U}$ is quantitatively correct, particularly at not-so-low frequencies, where the interplay with the low-energy correlated manifold is supposed to be weak. In the impurity calculation, the cRPA frequency dependence of $\mathcal{U}$ is taken into account and the self-consistent solution for G is hence affected by retardation effects contained in the impurity model.

As far as $\Sigma^{\rm xc}_{GW}$ is concerned, one needs to carry out a one-shot GW calculation on top of the LDA band structure to compute the initial non-local self-energy part. In the simplified implementation based on a constant P, the non-local part does not change, while the local part is changed according to the solution of the dynamic impurity model. Thus, the resulting lattice Green's function is $G(\mathbf{k}, i\omega) = [i\omega + \mu - H_0 - \Sigma(\mathbf{k}, i\omega)]^{-1}$, where $H_0 = H_{\rm LDA} - V^{\rm xc}_{\rm LDA}$ is the LDA Hamiltonian without the exchange-correlation potential, and $\Sigma(\mathbf{k}, i\omega)$ is the one defined in Eq. (111).

We note that if instead of replacing $V_{\rm xc}$ by $\Sigma^{\rm xc}_{GW}$ one keeps $V_{\rm xc}$ and adds a local Σ only, the above scheme reduces to the DFT+DMFT+$U(\omega)$ approach. From this perspective, the DFT+DMFT+$U(\omega)$ can be regarded as an embryo of the GW+DMFT method, which lacks non-locality and a proper treatment of double counting, but where the dynamical nature of both local and non-local screening effects is taken into account in the effective interaction of the impurity problem via the cRPA estimate of $U(\omega)$.

In the DFT+DMFT+$U(\omega)$ scheme, one could ask what is the correct double counting term in the presence of a retarded U. By assuming that the spectroscopic high-energy features described by the coupling with plasmons cancel out in the zero-temperature mean-field solution to recover the potentially exact DFT ground state energy, it turns out [110, 111] that the appropriate double counting is the same as the one introduced in Sec. II for static U, which in this case takes the value of the *screened* static limit of $U(\omega)$ ($U = U(\omega \to 0)$).

3. SEX+DMFT

In the GW approach, the COHSEX approximation[1] is a way to simplify greatly the calculation of the self-energy, by separating it into two static contributions $\Sigma = \Sigma_{\rm SEX} + \Sigma_{\rm COH}$,

where:

$$\Sigma_{\rm SEX}(\mathbf{r},\mathbf{r}') \;=\; -\sum_{i}^{\rm occ} \psi_i(\mathbf{r})\psi_i^*(\mathbf{r}')W(\mathbf{r},\mathbf{r}',0) \tag{114}$$

$$\Sigma_{\rm COH}(\mathbf{r},\mathbf{r}') \;=\; \frac{1}{2}\delta(\mathbf{r}-\mathbf{r}')\left(W(\mathbf{r},\mathbf{r}',0)-v(\mathbf{r}-\mathbf{r}')\right), \tag{115}$$

called screened exchange and Coulomb hole, respectively [2–4]. W is the static fully screened interaction. While the first term significantly improves upon the exchange contribution in the Hartree-Fock theory, the second one describes the contribution to the self-energy due to interactions between the quasiparticle and its surrounding hole. As it is apparent in Eqs. (114)-(115), the first term is non-local, while the second one is local.

The idea behind the SEX+DMFT theory is to replace the static local Coulomb hole self-energy by a dynamic one provided by the DMFT solution of a *downfolded* Hubbard model with retarded U, i.e. $\Sigma = \Sigma_{\rm SEX} + \Sigma_{\rm DMFT}$. The clear advantage with respect to the COH self-energy is that the DMFT one is dynamical and non-perturbative. Moreover, the validity of the SEX+DMFT theory is supported by the observation, verified in the iron pnictides and transition metal oxides such as $SrVO_3$, that at low-energy scales the non-local contributions to the self-energy are essentially static, while the local ones are dynamic. The self-energy separation between static non-local terms on the one side and dynamic local terms on the other side is implemented in the SEX+DMFT by merging SEX and DMFT. This is done in the same spirit as in LDA+DMFT, except that the $H^{\rm LDA} = H_0 + V^{\rm xc}_{\rm LDA}$ Hamiltonian is replaced by $H_0+\Sigma_{\rm SEX}$. We note that SEX+DMFT is not double-counting error free, because the DMFT Hamiltonian contains a local Hartree term already included in H_0. This can be easily estimated as a mean-field approximation of the Hubbard terms. Therefore, a double counting correction is needed as in regular LDA+DMFT, or LDA+DMFT with dynamic U.

Despite this fact, SEX+DMFT improves upon the LDA+DMFT method with dynamic U. The reason is that the SEX part yields wider bands than LDA, which partially compensates the band narrowing produced by the frequency dependence of U. As found in the case of the compound $BaCo_2As_2$ (Sec. VII B), which is isostructural to the more famous $BaFe_2As_2$ and only moderately correlated, these opposite effects almost cancel each other in the final result, and rather accurate quasiparticle energies are obtained.

In the practical implementation of Ref. [112], the screened exchange contribution is calculated as a Fock exchange with the screened potential in the limit of long wavelengths, i.e.

$W \approx W_{\rm TF} = \frac{e^2}{q^2+k_{\rm TF}^2}$, where $k_{\rm TF}$ is the Thomas-Fermi wavevector or inverse screening length. In the Thomas-Fermi theory, its value depends on the density of states (DOS) at the Fermi level. Thus, a self-consistent determination of $W_{\rm TF}$ can be devised, as a given $W_{\rm TF}$ yields a new DOS, that implies a new $k_{\rm TF}$, that closes the loop by finally fixing a new $W_{\rm TF}$, and so on. In the actual calculation of Ref. [112], this self-consistency has been replaced by a simple manual inspection to check that the guessed $k_{\rm TF}$ is consistent with the final DOS.

The band widening produced by SEX has the same origin as the larger bandwidth found in the non-local self-energy framework by a number of authors [26, 113–115]. The simplified static non-local version bears the same physics as the more involved full GW convolution. SEX+DMFT is the simplest theory capable of including non-local correlation effects besides the non-perturbative local ones provided by DMFT. Therefore, SEX+DMFT goes in the direction of extending DMFT in a fully *ab initio* fashion, to include longer-range interactions beyond the Hubbard type.

4. DMFT@nonlocal-GW

The DMFT@nonlocal-GW approach [108], as the previous SEX+DMFT method, is based on the observation (see Sec. VII C 1) that the local and non-local self-energy contributions are dynamically separable, with the former one frequency dependent and the latter one static. The DMFT self-consistency condition for the one-body quantities requires the local Green's function to satisfy

$$G^{\rm loc}(i\omega) = \sum_{\mathbf{k}} [i\omega + \mu - H_0(\mathbf{k}) - \Sigma_{GW}^{\rm nonloc}(\mathbf{k}, i\omega) - \Sigma_{\rm imp}(i\omega)]^{-1}, \tag{116}$$

with $H_0 = H_{\rm LDA} - V_{\rm LDA}^{\rm xc}$, and $\Sigma_{GW}^{\rm nonloc}$ is the nonlocal part of the full GW t_{2g} self-energy. As the nonlocal correlation self-energies are purely static in the low-energy window, i.e. $\Sigma_{GW}^{\rm nonloc}(\mathbf{k}, \omega) = \Sigma_{GW}^{\rm nonloc}(\mathbf{k})$, one can construct an effective quasi-particle Hamiltonian that also comprises these correlation effects:

$$H^{\rm qp}(\mathbf{k}) = H_0(\mathbf{k}) + {\rm Re}\Sigma_{GW}^{\rm nonloc}(\mathbf{k}). \tag{117}$$

$H^{\rm qp}$ is a simplified one-shot analogue of the QSGW Hamiltonian $H^{\rm QSGW}$ that was proposed in the context of the QSGW+DMFT formalism [116]. Then the DMFT self-consistency is much simpler since quantities are either frequency *or* momentum dependent, but not both,

which drastically reduces memory requirements. Of course, the simplified DMFT@nonlocal-GW scheme is not expected to give quantitatively accurate results *outside* the quasi-particle energy range. In particular the dispersion of collective excitations will not be captured. However, their position in the local spectrum which is determined by the structure of the dynamic interaction $\mathcal{U}(\omega)$ is still meaningful. The results of the DMFT@nonlocal-GW for $SrVO_3$ have been presented by Tomczak *et al.* in Ref. [108]. A previous attempt on the same compound was presented by Taranto *et al.* [117] by using a one-shot version of QSGW. However, in the latter work the authors obtained quite different results from Tomczak's, with a much stronger quasi-particle renormalization (Z=0.36) when the Z_B factor was used, probably due to a different way of dealing with the local self-energy subtraction at the QSGW level.

5. QSGW+DMFT

In the quasi-particle self-consistent GW (QSGW) + DMFT, one defines an effective static Hamiltonian, which includes non-local and dynamic correlation effects, through the fully self-consistent QSGW construction [118, 119]. In QSGW+DMFT, an additional self-consistency on the GW-level is performed which circumvents the full GW+DMFT self-consistency that is computationally very demanding and has so far has only been achieved on the model level [94, 102, 103], and the simpler case of a two-dimensional system of adatoms on surfaces [61]. In the QSGW+DMFT framework, once a self-consistent QSGW calculation is performed and the quasiparticles energies $E_{\mathbf{k}n}$ are found, the local part of the self-energy is subtracted to avoid double counting, and the non-local self-energy is evaluated at the corresponding $E_{\mathbf{k}n}$ energies. In this way, a static correction to the initial Hamiltonian is obtained, and incorporated into a modified Hamiltonian H^{nl}. Then, a DMFT calculation with dynamical $\mathcal{U}$ can be performed on top of H^{nl}. In contrast to DMFT@nonlocal-GW, dynamical non-local corrections can be incorporated into the QSGW+DMFT through the iterative QSGW construction. Suggested in Ref. [116] and later in [108], a simplified variant of this approach has recently been applied to the Mott insulator La_2CuO_4 [120].

6. Concluding remarks on simplified GW+DMFT approaches

All methods in Secs. IV B 3, IV B 4, and IV B 5, make the calculation of the non-local GW part faster and more efficient. However, the self-consistency is performed at the G level only. Therefore, these schemes are not fully self-consistent GW+DMFT approaches. However, in the SEX+DMFT approach, it is possible to perform an additional self-consistency on the screening Fermi wave-vector, through the evaluation of the density of states at the Fermi level. This replaces the self-consistency at the polarization level in a purely static screening approach.

We remark that the Thomas-Fermi model used for the SEX part in Ref. [112] has several well-known limitations. Its exponential decay form is valid only for metals; in insulators there is a longer-range decay instead [121]. Moreover, the Thomas-Fermi model (as well as RPA) overestimates screening in metals. In fact, due to the singularity at $2k_F$, there are Friedel oscillations with a $2k_F$ period, decaying as $1/r^3$, while in the Thomas-Fermi model the decay is always exponential. On the other hand, SEX+DMFT solves one of the major problems of the fully static COHSEX approximation, namely the lack of quasiparticle renormalization coming from the Z factor. Indeed, in SEX+DMFT, the DMFT part provides a non-perturbative frequency-dependent local self-energy, which usually yields a good estimate of Z. Therefore, as future perspective, it is worth trying to implement better approximations for the SEX part, to go beyond the Thomas-Fermi model, within the SEX+DMFT framework.

V. ANALYTICAL CONTINUATION

At present, the Monte Carlo technique discussed in Sec. III B 3 is the method of choice for the solution of impurity problems with dynamically screened interactions. For this reason, the extended DMFT or GW+DMFT calculations are most conveniently implemented on the Matsubara axis. For the interpretation of the results, it is however often important to have access to spectral functions. The analytical continuation from the Matsubara-frequency to the real-frequency axis is a delicate problem and particularly challenging in the case where high-energy features exist and need to be resolved. Both the Padé [122] and maximum entropy methods [123], which usually work well for low-frequency features

in systems at low enough temperature, are not well-suited for capturing the high-frequency part of the spectrum. A pre- and post-processing of the data is needed in order to use these methods as part of a somewhat elaborate analytical continuation scheme. In Sec. V A, we explain the scheme for calculating the fermionic spectral function corresponding to some LDA+DMFT+$U(\omega)$ calculation. We will also briefly address the calculation of the bosonic spectral functions from EDMFT or GW+DMFT calculations, focusing in this case on models with static bare interactions (Sec. V B).

A. Fermionic spectral function

The idea proposed in Ref. [85] is to split the Green function $G(\tau)$ into a product of a bosonic function $B(\tau)$ and an auxiliary fermionic Green function $G_{\rm aux}(\tau)$:

$$G(\tau) = B(\tau) G_{\rm aux}(\tau). \tag{118}$$

From the spectral functions ρ_B and $\rho_{\rm aux}$ of the two factors one can then obtain the spectral function $\rho(\omega)$ of the original Green function using the convolution

$$\rho(\omega) = \int_{-\infty}^{\infty} d\epsilon \rho_B(\epsilon) \frac{1+e^{-\beta\omega}}{(1+e^{\beta(\epsilon-\omega)})(1-e^{-\beta\omega})} \rho_{\rm aux}(\omega-\epsilon). \tag{119}$$

The bosonic function $B(\tau)$ can be chosen arbitrarily, as long as the factorization (118) does not lead to unphysical properties of $G_{\rm aux}$. A natural choice, which often works in practice, is

$$B(\tau) = e^{-K(\tau)}, \tag{120}$$

where $K(\tau)$ is the twice-integrated screening function defined in Eq. (58). The rationale for this choice is that such a factorization holds in the atomic limit (see Sec. III B).

Substituting $\tau = it$ in Eq. (58), and expressing the factor $\frac{\cosh(\omega(\beta/2-it))}{\sinh(\omega\beta/2)}$ as $e^{-it\omega} + \frac{2\cos(\omega t)}{e^{\beta\omega}-1}$, one finds

$$K(t) = \int_0^{\infty} d\omega \frac{{\rm Im}U(\omega)}{\pi\omega^2} \left(e^{-it\omega} + \frac{2\cos(\omega t)}{e^{\beta\omega}-1} - \frac{e^{\beta\omega}+1}{e^{\beta\omega-1}} \right) \approx \int_0^{\infty} d\omega \frac{{\rm Im}U(\omega)}{\pi\omega^2} (e^{-it\omega}-1). \tag{121}$$

In the last step we used the fact that at low temperatures, $e^{\beta\omega} \gg 1$, except near $\omega = 0$, where ${\rm Im}U(\omega)$ vanishes. At low enough temperature, we can therefore express the bosonic factor on the real-time axis as

$$B(t) = e^{-K(t)} = \underbrace{\exp\Big[\int_0^{\infty} d\omega \frac{{\rm Im}U(\omega)}{\pi\omega^2} \Big]}_{Z_B} \exp\Big[-\int_0^{\infty} d\omega \frac{{\rm Im}U(\omega)}{\pi\omega^2} e^{-i\omega t} \Big] \tag{122}$$

The first term corresponds to the Bose factor defined in Eq. (71), while the second term oscillates around 1 as $t \to \infty$. We thus split off Z_B and write

$$B(t) = Z_B + B_{\text{reg}}(t), \tag{123}$$

with the regular term $B_{\text{reg}}(t) = Z_B(\exp[-\int_0^\infty d\omega \frac{\text{Im}U(\omega)}{\pi\omega^2} e^{-i\omega t}] - 1)$. The corresponding spectral density $\rho^B_{\text{reg}}(\omega)$ can be obtained numerically from an appropriate Fourier transform. We have the spectral representation

$$B_{\text{reg}}(t) = \int_{-\infty}^{\infty} d\omega' \rho^B_{\text{reg}}(\omega') \frac{e^{-i\omega' t}}{1 - e^{-\beta\omega'}}, \tag{124}$$

and therefore

$$\int_{-\infty}^{\infty} dt e^{i\omega t} B_{\text{reg}}(t) = \int_{-\infty}^{\infty} d\omega' \underbrace{\int_{-\infty}^{\infty} dt e^{i(\omega-\omega')t}}_{=2\pi\delta(\omega-\omega')} \frac{\rho^B_{\text{reg}}(\omega')}{1 - e^{-\beta\omega'}} = 2\pi \frac{\rho^B_{\text{reg}}(\omega)}{1 - e^{-\beta\omega}}. \tag{125}$$

Using $B_{\text{reg}}(-t) = [B_{\text{reg}}(t)]^*$, we can write the left hand side as $2\text{Re}\int_0^\infty dt e^{i\omega t} B_{\text{reg}}(t)$, which finally yields the expression

$$\rho^B_{\text{reg}}(\omega) = \frac{1 - e^{-\beta\omega}}{\pi} \text{Re} \int_0^\infty dt e^{i\omega t} B_{\text{reg}}(t). \tag{126}$$

It immediately follows from this derivation that the constant Z_B in Eq. (123) gives a non-regular contribution

$$\rho^B_{\text{non-reg}}(\omega) = Z_B(1 - e^{-\beta\omega})\delta(\omega) \tag{127}$$

to the spectral density. Substitution of (127) into Eq. (119) gives

$$\rho_{\text{non-reg}}(\omega) = Z_B \rho_{\text{aux}}(\omega), \tag{128}$$

which is the expected renormalization of the quasi-particle peak by the Bose factor (see Sec. III D and Eq. (71)).

In summary, the spectral function ρ can be computed from the maximum entropy result for $\rho_{\text{aux}}(\omega)$ and either the cRPA result or some numerical estimate for $\text{Im}U(\omega)$ using the following formulas:

$$\rho(\omega) = Z_B \rho_{\text{aux}}(\omega) + \int_{-\infty}^{\infty} d\epsilon \rho^B_{\text{reg}}(\epsilon) \frac{1 + e^{-\beta\omega}}{(1 + e^{\beta(\epsilon-\omega)})(1 - e^{-\beta\omega})} \rho_{\text{aux}}(\omega - \epsilon), \tag{129}$$

$$\rho^B_{\text{reg}}(\omega) = \frac{1 - e^{-\beta\omega}}{\pi} \text{Re} \int_0^\infty dt e^{i\omega t} B_{\text{reg}}(t), \tag{130}$$

$$B_{\text{reg}}(t) = Z_B \Big(\exp\Big[- \int_0^\infty d\omega \frac{\text{Im}U(\omega)}{\pi\omega^2} e^{-i\omega t} \Big] - 1 \Big). \tag{131}$$

B. Bosonic spectral function

Here we discuss a useful strategy for calculating the spectral function $\mathrm{Im}U(\omega)$ corresponding to some retarded interaction $U_{\mathrm{ret}}(\tau)$, as it is obtained for example in the self-consistency loop of an EDMFT or GW+DMFT simulation [103]. In a maximum entropy approach, it is important to work with a properly normalized spectral function. In the bosonic case, we can use the relation

$$U_{\mathrm{scr}} - U = 2\int_0^\infty d\omega \frac{1}{\pi}\frac{\mathrm{Im}U(\omega)}{\omega} \tag{132}$$

to define such a normalized distribution function:

$$B(\omega) = \frac{2}{\pi(U_{\mathrm{scr}} - U)}\frac{\mathrm{Im}U(\omega)}{\omega}, \quad \int_0^\infty d\omega B(\omega) = 1. \tag{133}$$

Equation (63), which connects the retarded interaction to the spectral density can then be written in the form

$$U_{\mathrm{ret}}(\tau) = \int_0^\infty d\omega K(\omega,\tau)B(\omega), \tag{134}$$

with the bosonic kernel

$$K(\omega,\tau) = \frac{\omega(U_{\mathrm{scr}} - U)}{2}\frac{\cosh(\omega(\beta-\tau/2))}{\sinh(\omega\beta/2)}. \tag{135}$$

(If the ω integration is taken from $-\infty$ to ∞, the kernel becomes $\tilde{K}(\omega,\tau) = \frac{e^{-\tau\omega}}{1-e^{-\beta\omega}}\frac{\omega(U_{\mathrm{scr}}-U)}{2}$.) The factor $(U_{\mathrm{scr}} - U)$ is known from the solution on the Matsubara axis.

We can now use the maximum entropy method [123] to solve Eq. (134) for $B(\omega)$, and finally Eq. (133) to find $\mathrm{Im}U(\omega)$. The real part can as usual be obtained from the antisymmetry of $\mathrm{Im}U(\omega)$ and the Kramers-Kronig relation

$$\mathrm{Re}U_{\mathrm{ret}}(\omega) = \frac{1}{\pi}P\int_{-\infty}^\infty d\omega' \frac{\mathrm{Im}U(\omega')}{\omega'-\omega} = \frac{1}{\pi}P\int_{-\infty}^\infty d\omega' \left(\frac{\mathrm{Im}U(\omega') - \mathrm{Im}U(\omega)}{\omega'-\omega}\right). \tag{136}$$

In the last step, we have re-expressed the integral in a form which is suitable for numerical treatment.

VI. APPLICATIONS TO MODEL SYSTEMS

A. Extended DMFT

1. U-V Hubbard model

The EDMFT solution for the half-filled U-V Hubbard model (75) on the cubic lattice predicts a paramagnetic phase diagram with three phases: a metallic phase for small U and small V, a Mott insulating phase for large U and small V, and a charge ordered insulating phase for sufficiently large V [100]. Recently, the low-temperature phase diagrams on the 2D square and 3D cubic lattices have been mapped out using the efficient and unbiased impurity solver described in Sec. III B 3 [94, 103]. In Fig. 9 we show the results for generalizations of model (75) with nonlocal interactions up to the third-nearest neighbors. Here, the parameter V encodes the strength of the nonlocal interactions, i.e. the non-local interactions are scaled as $V_{ij} = a/|r_i - r_j|$, with a the lattice spacing and $r_{i,j}$ the positions of the nearest-neighbor, next-nearest neighbor or third nearest neighbor sites. The unit of energy is the hopping.

In the square-lattice case with only nearest-neighbor interactions, the $V_c(U)$ phase boundary jumps near the intersection with the Mott transition line. In the models with longer-ranged interactions, the metallic phase extends to larger values of U, forming a "nose" which separates the Mott insulator and charge ordered phases at low temperature. The jump in $V_c(U)$ disappears, so that the phase diagram looks qualitatively similar to that of the Hubbard-Holstein model with large phonon frequency (Fig. 6). However, in the Hubbard-Holstein case, the boundary to the charge ordered phase does not exhibit a slope change near the critical U for the Mott transition, which indicates that the slope change in the EDMFT phase diagram originates from changes in the dominant screening modes near U_c [103].

Overall, the phase diagrams for the 2D and 3D lattice are similar, with the main difference being the larger extent of the metallic nose in the 3D case, and a different dependence of the metal-charge order phase boundary on the interaction range. The latter can be explained by considering the lattice geometry and our definition of next-nearest and third-nearest neighbors [103]: in the 2D case, the third-nearest neighbor interactions act between sites on the same sublattice, and hence frustrate the charge order, while in the 3D case, they act between sites on different sublattices.

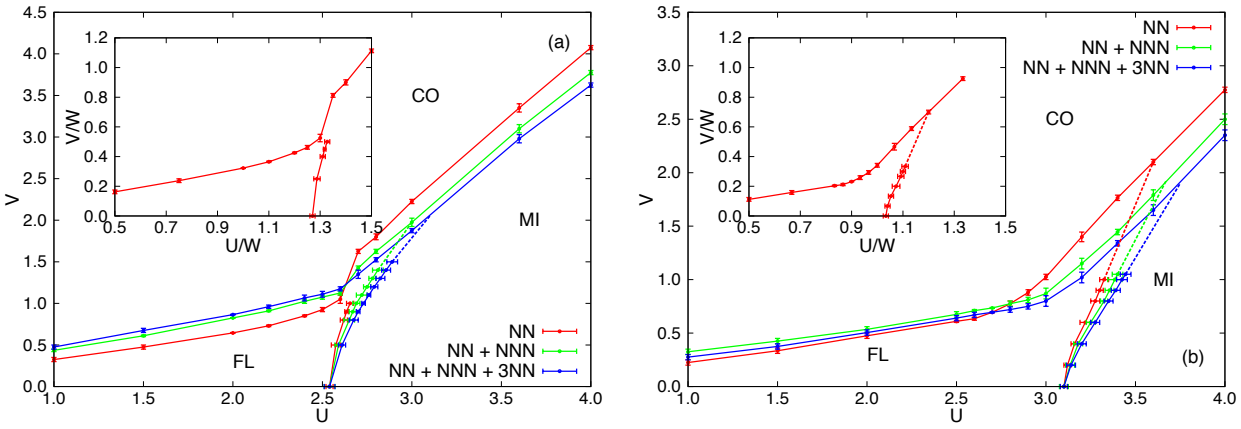


FIG. 9: Paramagnetic phase diagram of the half-filled U-V Hubbard model on the 2D square lattice (a) and 3D cubic lattice (b). Results for non-local interactions up to nearest neighbors (NN), next-nearest neighbors (NN+NNN) and third nearest neighbors (NN+NNN+3NN) are shown. FL denotes the metallic phase, CO the charge ordered insulating phase, and MI the Mott insulating phase. The insets show the phase diagrams of the models with NN interactions with axes rescaled by the bandwidth. (From Ref. [103].)

In order to identify the dominant screening modes, and understand their origin, it is instructive to compute the bosonic and fermionic spectral functions, as illustrated in Fig. 10 for a metallic and Mott insulating system. Let us focus first on the half-filled case (blue lines and symbols). As seen in panels (c) and (f), Im$W(\omega)$, which is proportional to the square of the coupling strength of the screening modes with frequency ω, exhibits two peaks near U and $U/2$ in the metallic system, and a single peak near U in the insulating case. The comparison to the fermionic spectral functions plotted in panels (a) and (d) suggests that the peak at U is related to transitions between the Hubbard bands, while the peak at $U/2$ in the metallic system originates from transitions between the quasi-particle band and one of the Hubbard bands.

If the chemical potential is shifted away from the particle-hole symmetric value (green curves), the spectral functions change. In the metallic system, the peak near $U/2$ grows and shifts to lower energies, consistent with the increased weight of the quasi-particle peak and the reduced separation between this peak and the upper Hubbard band in the fermionic spectral function. The high energy peak also grows, which suggests that the asymmetric shape and population of the Hubbard bands enhances the screening effect. Despite the

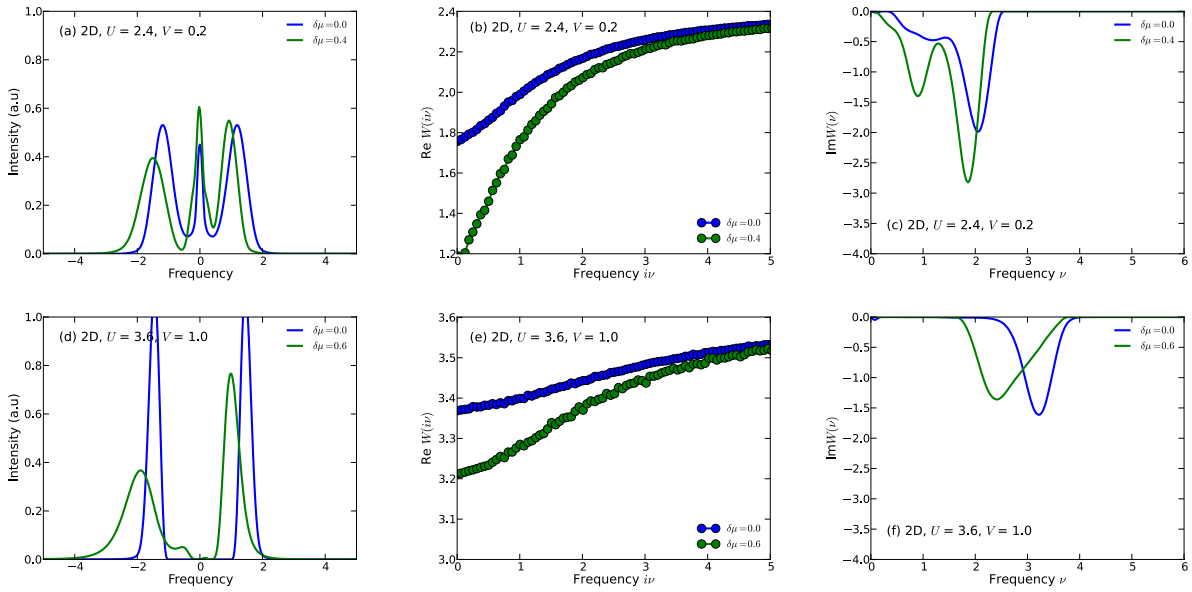


FIG. 10: Fermionic and bosonic spectral functions for the paramagnetic Hubbard model with NN interactions on the square lattice. The blue curves show the results for a half-filled system and the green curves for a particle-hole asymmetric system with a chemical potential shift of $\delta\mu = 0.4$ and 0.6 relative to the half-filled value $\mu = U/2$. Panels (a)-(c) show results for a metallic system with $U = 2.4$ and $V = 0.2$, while panels (d)-(f) show results for a Mott insulating system with $U = 3.6$ and $V = 1.0$. The left panels plot the fermionic spectral function $A(\omega)$, the middle panels the real part of the screened interaction Re$W(i\nu)$ on the Matsubara axis, and the right panels the bosonic spectral functions Im$W(\omega)$. (From Ref. [103].)

uncertainties in the analytical continuation, it appears that one can even identify a third low-energy mode associated with transitions within the quasi-particle peak. In the insulating case, the reduction in the gap size and the broadening of the lower Hubbard band are reflected in a shift of the peak in Im$W(\omega)$ to lower energies, and a broader distribution of screening modes.

In the middle panels, we plot the real part of the screened interactions on the Matsubara axis. In the high-frequency limit Re$W(i\nu_n)$ approaches the bare on-site interaction U, while below an energy scale determined by the dominant screening modes, the screened interaction is reduced. Here, we should recall the fact that this reduction is dominated by the low-energy modes (see Eq. (28)). Hence, Re$W(0)$ is not much smaller than U in the insulator, while

the low-energy screening modes in the metallic case lead to a substantially reduced static interaction.

2. Dynamical screening in photo-doped Mott insulators

The real-time dynamics of screening has been recently investigated using a nonequilibrium generalization of EDMFT [124]. As discussed in Ref. [125], the DMFT formalism can be applied to nonequilibrium problems by solving the DMFT equations on a 3-branch Kadanoff-Baym contour which runs from 0 to some maximum time $t_{\max}$ along the real time axis, back to time 0 along the real time axis, and then to $-i\beta$ along the imaginary time axis. The solution on the imaginary-time branch corresponds to the usual DMFT solution for the initial equilibrium state (with β the inverse temperature), while the solution on the real-time branches allows to describes the evolution of the system after some perturbation or in the presence of external fields. In a similar manner, the bosonic self-consistency loop of EDMFT can be solved on the Kadanoff-Baym contour and the resulting nonequilibrium EDMFT formalism then captures the changes in the screening properties resulting from the nonthermal state of the system. In Ref. [124], the U-V Hubbard model (75) on the square lattice was driven out of an initially Mott insulating state by a single-cycle electric-field pulse with frequency $\Omega_{\text{pulse}} \approx U$ directed along the lattice diagonal. As shown in the right hand panel of Fig. 11, $\text{Im}W(\omega)$, which represents the distribution of screening modes, initially exhibits a single broad peak centered at energy U, similar to Fig. 10(f). This is because in a Mott insulator, the screening processes involve particle excitations across the gap.

However, as soon as the field pulse creates doublon-hole pairs, a second screening mode appears at lower energy, and the imaginary part of $W(\omega, t) = \int_t^{t+t_{\text{cut}}} dt' e^{i\omega(t'-t)} W^{\text{ret}}(t', t)$ (with Fourier cutoff $t_{\text{cut}} = 10$) qualitatively resembles the equilibrium result for a metallic system (Fig. 10(c)). An essential difference to the equilibrium metallic system however is the absence of a coherent quasi-particle band [126], which implies that the low-energy screening modes in the photo-doped system are not associated with transitions between quasi-particle and Hubbard bands, but rather with screening transitions within the photo-doped Hubbard bands. This also explains the broader energy distribution. As shown in Fig. 11, the low-energy mode grows while the pulse (which lasts up to $t \approx 1.5$) produces additional carriers, and then essentially saturates. The subsequent slower evolution of the bosonic spectral

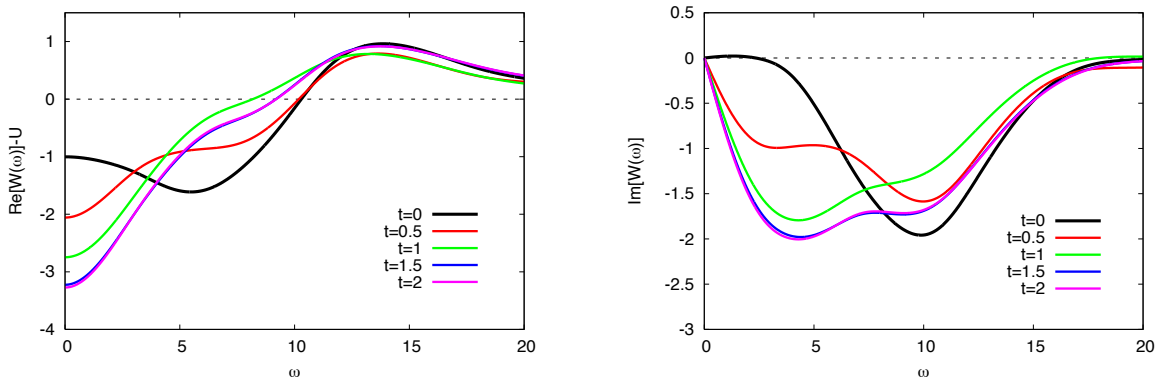


FIG. 11: Time-evolution of the screened interaction W in a Mott insulator which is excited by a mono-cycle electric field pulse with $\Omega_{\rm pulse} = U$. The electric field pulse has the form $E(t) = E_0 \sin(\Omega_{\rm pulse}(t-t_0)) \exp(-4.6(t-t_0)^2/t_0^2)$ with $t_0 = 2\pi/\Omega_{\rm pulse}$ and $E_0 = 9$. $U = 10$, $V = 2$, initial $\beta = 5$. (From Ref. [124].)

function (not shown) is governed by changes in the energy distribution of the photo-doped carriers, and on much longer timescales by doublon-hole recombination processes.

Looking at the real part of the screened interaction, which is plotted in the left hand panel, we see that the high-energy mode produces only a small screening effect, as expected in a Mott insulator, while the low-energy screening modes linked to screening transitions within the photo-doped Hubbard bands lead to a significant reduction of $\mathrm{Re}W(\omega = 0, t)$. The evolution of the bosonic Weiss field $\mathcal{U}(\omega, t)$ looks qualitatively similar to that of $W(\omega, t)$, but with smaller screening effects. The reduction of $\mathcal{U}$ by the enhanced screening in the photo-doped Mott insulator results in a shrinking of the gap size and potentially even in a screening-induced transition to a transient metallic state.

B. GW+DMFT

1. U-V Hubbard model

The first self-consistent GW+DMFT calculations have been presented for the U-V Hubbard model (75) in Refs. [102] and [94]. The nonlocal component of the self-energy Σ was

found to be much smaller than the local contribution, even close to the Mott transition. This result is inconsistent with cluster DMFT data, which (for the half-filled Hubbard model) predict a strong momentum differentiation between the nodal and antinodal region, and even a momentum-selective metal-insulator transition [18]. However, as mentioned in Sec. IV A 2, the main purpose of the GW+DMFT scheme is not to provide an accurate description of the momentum dependent self-energy, but to enable a self-consistent description of screening. Hence, it is more interesting to look at the polarization function $P(\mathbf{k}, \omega)$. It was shown in Ref. [94] that the nonlocal components of the polarization can be of the same order of magnitude as the local polarization if the system is close to the charge ordering instability.

A relevant question is to what extent the self-consistent feedback of the momentum-dependent polarization and self-energy affects the converged result. To illustrate this, we compare in Fig. 12 different approximations for the polarization [94]: the local polarization obtained from EDMFT (panel (a)), the bubble GG computed with EDMFT lattice Green's functions (panel (b)), the sum of the local EDMFT polarization and the nonlocal part of the bubble (panel (c)), and the self-consistent GW+DMFT polarization (panel (d)). Let us first consider panels (a) and (c). While the bubble diagram GG yields a $\mathbf{k}$-dependent polarization, it lacks vertex corrections beyond those built into the EDMFT propagators. The local EDMFT polarization, which is calculated from the density-density correlation function (86), contains the local vertex. An advantage of the GW+DMFT method is that it incorporates both this local vertex and the momentum-dependence of the bubble in a self-consistent manner. The effect of the self-consistent treatment becomes apparent by comparing panels (b) and (d). While we can combine the local EDMFT polarization and the nonlocal component of the EDMFT polarization bubble in the spirit of GW+DMFT, such a calculation lacks a self-consistent feedback, and as a result, the momentum-dependence of the polarization looks quite similar to the bubble result, away from the $(0, 0)$ point. In the GW+DMFT polarization, some of the momentum-dependent structures differ significantly from the "one-shot" result in panel (b), especially near the $(\pi, 0)$ point.

The self-consistent feedback of the $\mathbf{k}$-dependent self-energy and polarization also has an effect on local observables, such as the local spectral function. In Refs. [102], [94] and [103] it was found that in the half-filled U-V Hubbard model, the self-consistent GW+DMFT calculation yields stronger correlation effects than DMFT, as exemplified by a larger mass enhancement or more pronounced Hubbard bands. "One shot" calculations, in which a

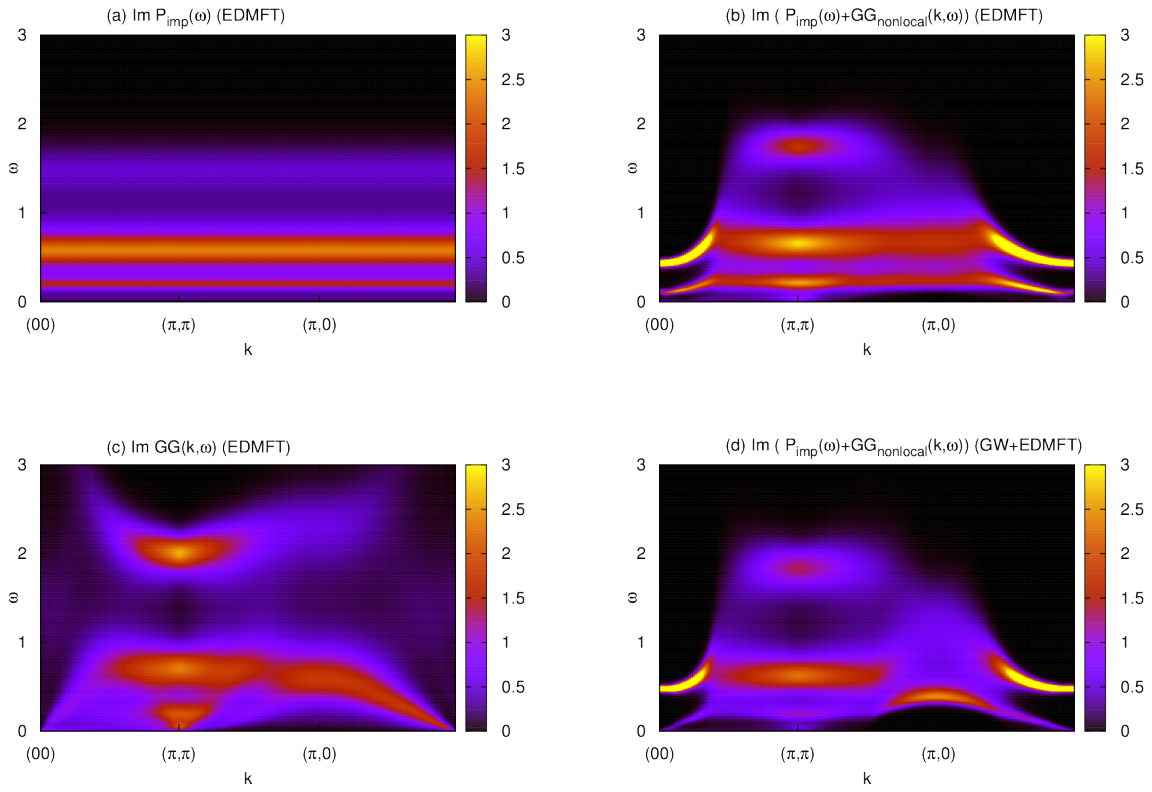


FIG. 12: Comparison of various approximations for the momentum dependent polarization function ($U = 1.5$, $V = 0.4$). (From Ref. [94].)

nonlocal GW contribution is added to the converged EDMFT self-energy, produced the opposite effect. This result however appears not to be a generic one. For example, it was found in a recent study of the Hubbard model away from half-filling that the inclusion of the non-local GW diagrams reduces the correlation effects [22]. The latter study, which was restricted to the weak-coupling regime, concluded that GW+DMFT provides slightly more accurate results for the local self-energy than DMFT, while the non-local components are not improved with respect to pure GW.

In the strong-coupling regime, where the failure of self-consistent GW to produce Hubbard bands is well known, the combination with DMFT enables physically meaningful self-consistent calculations [102]. Therefore, the main advantage of the GW+DMFT scheme is that it enables a self-consistent treatment of screening effects at arbitrary interaction strength.

TABLE II: Bare [effective] on-site interactions U^{bare} [U] and nearest-neighbor interactions V^{bare} [V]. Also shown is the static value of the effective on-site interaction $\mathcal{U}(\omega = 0)$ obtained from GW+DMFT. All values are in eV. (From Ref. [61].)

	C	Si	Sn	Pb
U	1.4	1.1	1.0	0.9
V	0.5	0.5	0.5	0.5
U^{bare}	6.0	4.7	4.4	4.3
V^{bare}	2.8	2.8	2.7	2.8
$\mathcal{U}(\omega = 0)$	1.3	0.94	0.84	0.67 (insulator)
				0.54 (metal)

2. Adatom systems on semiconductor surfaces

An interesting playground to explore correlation effects in two-dimensional lattice systems are periodic systems of adatoms on a semiconductor surface [127]. A recent *ab initio* study of Si(111):X (X=Sn, C, Si, or Pb) based on cRPA downfolding and a self-consistent GW+DMFT solution of the low-energy effective theory has revealed the importance of non-local Coulomb interactions and dynamical screening effects in these systems and consistently explained material trends for this series of adatoms [61]. In this work, the one-particle part of the Hamiltonian was calculated in the LDA approximation, yielding a half-filled single band of predominantly p_z character near the Fermi level, with a bandwidth of approximately 0.5 eV for all systems considered. The interaction parameters (partially screened Coulomb matrix elements) were calculated using cRPA and a low-energy window containing the surface band. The resulting *static* interaction parameters for the on-site (U) and nearest-neighbor (V) interactions are listed in Tab. II. Also shown for comparison are the bare interaction values, which ignore the screening effects from higher-energy bands.

While the on-site interaction is large, about 2-3 times the bandwidth, the non-local interactions are also substantial, and the resulting nonlocal screening effects are essential for understanding the properties of the different adatom systems. It is furthermore evident

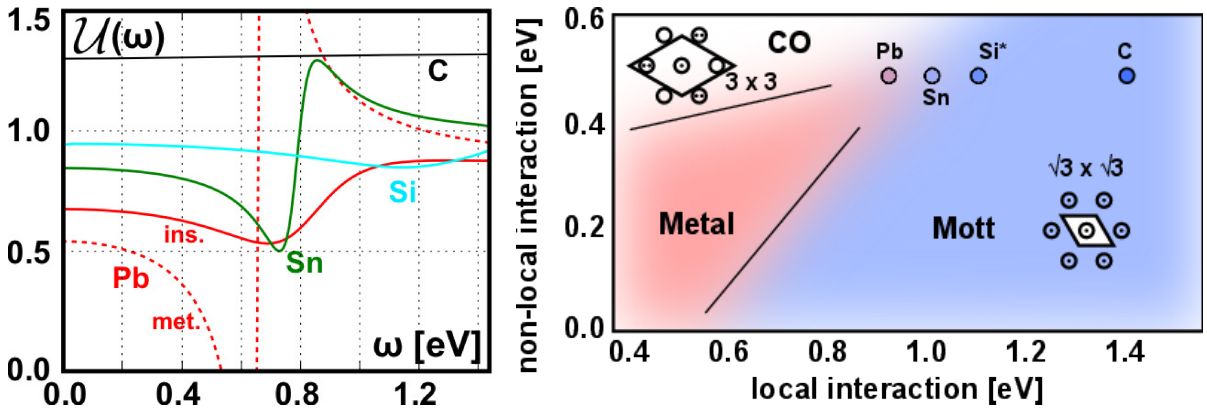


FIG. 13: Left panel: frequency-dependent on-site interactions for the adatom systems Si(111):X (X=Sn, C, Si, Pb) obtained within GW+DMFT. Right panel: Schematic phase diagram in the space of non-local and local interactions with Mott insulating, metallic and charge ordered (CO) regions. The surface unit cells of the insulating phases are sketched as in-sets. (From Ref. [61].)

that the nearest-neighbor interaction is almost independent of the adatom type. The reason is the relatively large distance of 6 Å between the adatoms, which implies that the intersite Coulomb energy is essentially that of two point charges. It was furthermore found that V is very close to the value of $V^{\rm bare}$ divided by the static dielectric constant of the silicon surface, which suggests that one can compute the longer-range interactions by rescaling V with a/r, where a is the nearest neighbor distance. In this sense, V parametrizes the strength of all the non-local interactions. The $1/r$ tail can be treated by an Ewald summation.

The low-energy model with these static on-site and off-site interactions (a particular realization of the single-orbital U-V Hubbard model) was solved using self-consistent GW+DMFT [61]. The dynamical interaction $\mathcal{U}(\omega)$ obtained within this scheme is plotted in the left panel of Fig. 13 and reflects the nonlocal screening effect on the local interaction. While at high frequencies, screening is not effective and $\mathcal{U}(\omega \to \infty) = U$, the static value of $\mathcal{U}$ can be substantially reduced, especially in a metallic system (Si(111):Pb). As a result, also the gap values are smaller than they would be in the absence of nonlocal screening.

The simulation results, which reproduce the experimentally observed materials trends, are summarized in the schematic phase diagram of Fig. 13 (right panel). While all the considered systems have the same strength of the nonlocal interactions, their on-site inter-

actions differ. As a result of this, the screening effect in Si(111):C and Si(111):Si is small (see left panel), which places these systems in the Mott insulating region of the phase diagram, while Si(111):Sn and Si(111):Pb are close to a metallic solution (the latter one is in fact in a coexistence regime). It was also found that Si(111):Pb is close to a charge ordering instability.

VII. APPLICATIONS TO REALISTIC MATERIALS

A. LDA+DMFT+$U(\omega)$

The frequency-dependent interaction parameters derived from cRPA have been employed in several recent *ab initio* simulations based on the LDA+DMFT framework [44, 110, 128, 129]. These simulations have produced high-energy satellites and enhanced correlations in often good agreement with experiments. In this section, we illustrate the important effects of the dynamical $U(\omega)$ by focusing on three materials: $SrVO_3$ (Sec. VII A 1), hole-doped $BaFe_2As_2$ (Sec. VII A 2) and undoped La_2CuO_4 (Sec. VII A 3).

1. Mass enhancement and satellites in $SrVO_3$

The correlated metal $SrVO_3$, with an undistorted perovskite structure, has been studied extensively within LDA+DMFT, LDA+DMFT+$U(\omega)$ and variants of GW+DMFT. It is a suitable test material for new computational schemes, because of its relatively simple bandstructure, with a well-defined low-energy window containing the three t_{2g} bands. The LDA bandwidth is 2.6 eV. Experiments indicate a substantial narrowing of these bands, by about a factor of two, and the appearance of satellites below and above the renormalized quasi-particle band [130]. Conventionally, these satellites have been interpreted as Hubbard bands, but recent theoretical results force us to reconsider this interpretation.

LDA+DMFT calculations with a static $U = 5$ eV and a Hund coupling parameter $J = 0.68$ eV were shown in Ref. [131] to produce the correct band renormalization. The resulting **k**-integrated spectrum features a pronounced lower and upper Hubbard band at -1.8 and 3 eV, respectively. A more recent study [132] employed $U = 5.5$ eV, which results in an even larger splitting between the Hubbard bands. LDA+DMFT calculations with a dynamically screened $U(\omega)$ have been performed within the DALA approximation

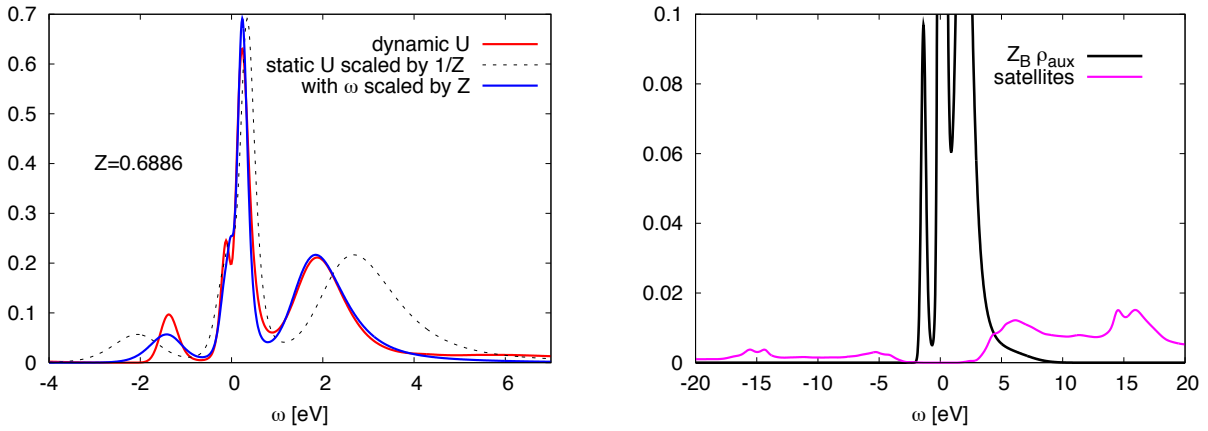


FIG. 14: Left panel: local spectral function of $SrVO_3$ from the dynamic-U simulation (red) and the effective static model of Sec. III D (blue). Right panel: Low-energy and satellite contributions to the local spectral function (Eq. (129)).

(Sec. III B 1) in Ref. [85] and using the full cRPA interaction and the CTQMC scheme of Sec. III B 3 in Refs. [128, 133]. The frequency dependent U used in Ref. [133] is plotted in the left panel of Fig. 2. It has a static value of 3.4 eV and a dominant pole structure near $\omega = 14$ eV. The width of the renormalized quasiparticle band predicted by the LDA+DMFT+$U(\omega)$ calculation is 0.9 eV, which is too narrow compared to experiment. As we will argue in Sec. VII C 1, the missing ingredient in this calculation is the widening of the band due to the momentum dependence of the self-energy. In this section, we would like to comment on the proper static-U description (Sec. III D), and the implications for the position of the Hubbard bands.

If the band-widening effect of the **k**-dependent self-energy is neglected, the static description should involve the cRPA $U(\omega = 0)$ and a bandwidth reduced by the Bose factor (71), which for $SrVO_3$ is $Z_B = 0.689$. Since the material has three equivalent t_{2g} bands, shrinking the bandwidth by Z_B is equivalent to increasing the static interaction to $3.4/Z_B = 4.93$ eV and rescaling the frequency axis by Z_B.

The left panel of Fig. 14 compares the local spectral function from the dynamic-U simulation (red line) to a static-U simulation with enhanced on-site interaction before (dashed black line) and after (blue line) the rescaling of the frequency axis. The dashed line is essentially the result of the previous LDA+DMFT simulations [131]. After the rescaling of the frequency axis by the factor Z_B, one recovers the mass renormalization of the quasi-particle

band and the Hubbard band positions of the $U(\omega)$ calculation. The upper Hubbard band is placed at 2 eV, instead of 3 eV, and the lower Hubbard band is shifted from about -2 eV to -1.6 eV. The latter position is consistent with photo-emission experiments [130]. The spectral weight which is lost by the rescaling of the frequency axis is shifted to high-energy satellites near ± 15 eV, and also at ± 5 eV (see right panel), which cannot be extracted from a static-U simulation. Looking at the cRPA result for $U(\omega)$ (Fig. 2), we see that the energies of these satellites are determined by the dominant screening modes (peaks in $\mathrm{Im}U(\omega)$). In fact, the analytical continuation procedure discussed in Sec. V by construction leads to satellite features at the corresponding energy off-sets.

This example illustrates the general fact that LDA+DMFT+$U(\omega)$ simulations can produce the same mass renormalizations as static-U LDA+DMFT simulations, but with a lower $U(\omega = 0)$ (here, 3.4 eV instead of 5 eV). As a consequence, the splitting between the Hubbard bands is reduced, or the Hubbard bands may not even be well defined anymore, as in the example discussed in the following subsection.

2. Spin-freezing crossover in hole-doped $BaFe_2As_2$

$BaFe_2As_2$ is a prototypical compound of the so-called 122 family of iron based superconductors. It becomes superconducting under pressure, or by hole- and electron-doping. The hole-doped compound exhibits nontrivial correlation effects, even in the normal phase (above the maximum T_c of 38 K [134]), as exemplified by the widely varying experimental estimates of the mass enhancement [135, 136]. The remarkable sensitivity of the electronic structure to changes in temperature, pressure or doping was shown [110] to be related to the proximity of the optimally hole-doped compound to a spin-freezing crossover. Spin-freezing [137] has recently been recognized as a generic and important phenomenon affecting the properties of multi-orbital systems with Hund coupling in a certain regime of filling, interaction strength and temperature [138]. Inside the spin-frozen regime, long-lived magnetic moments appear, which leads to strong scattering and bad metallic behavior. The boundary of the spin freezing regime is characterized by fluctuating local moments and non-Fermi liquid properties, in particular a self-energy which varies as a square-root of frequency (rather than linearly with frequency) on the Matsubara axis [137]. Such a square-root self-energy leads to strong band renormalizations at low energy, even in system which do not exhibit Hubbard bands. Due to

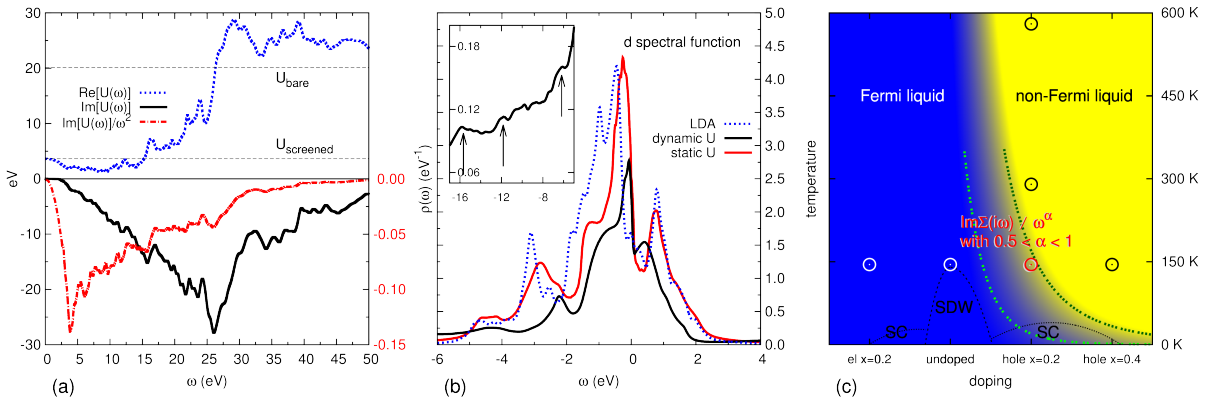


FIG. 15: Panel (a): cRPA result for the partially screened U of the 5-band model of $BaFe_2As_2$. Panel (b): d-electron spectral function from LDA (blue), LDA+DMFT with static $U = U_{\rm scr}$ (red), and LDA+DMFT+$U(\omega)$ calculations (black). The inset shows the high-energy features in the dynamic-U spectral function. Panel (c): Sketch of the phase diagram of $BaFe_2As_2$ in the space of temperature and doping. The spin-frozen region is indicated by yellow, whereas blue corresponds to Fermi liquid behavior. The border of the spin-frozen regime is characterized by a self-energy which varies like $\mathrm{Im}\Sigma(i\omega_n) \sim \omega_n^\alpha$, with $0.5 < \alpha < 1$. (Adapted from Ref. [110].)

the dramatic changes in the electronic structure in the spin-freezing crossover regime, an *ab initio* simulation of hole-doped $BaFe_2As_2$ requires an accurate estimation of the interaction parameters.

The left panel of Fig. 15 shows the real and imaginary parts of the partially screened interaction $U(\omega)$ for the Fe-d states estimated from cRPA [110]. The real part varies from the static value $U(\omega = 0) = 3.6$ eV to a bare value $U_{\rm bare} \approx 20$ eV. The plasmon excitation near $\omega \approx 26$ eV overlaps with single-particle excitations, which results in a broad peak in $\mathrm{Im}U(\omega)$. In order to properly judge the importance of the different features we also plot $\mathrm{Im}U(\omega)/\omega^2$. As discussed in Sec. III C it is the twice-integrated retarded interaction, or $\mathrm{Im}U(\omega)/\omega^2$, which enters into the calculation of the diagram weights in a hybridization expansion solver (see Eq. (58)). Apart from a dominant peak at 3.8 eV, which results from the lack of "high-energy" screening processes below this frequency, there are additional peaks at 6.1, 12 and 16 eV. As in the case of $SrVO_3$ discussed in the previous subsection, such sharp structures can be expected to lead to side-bands in the d-electron spectral function at the corresponding energies. Indeed, as shown in the middle panel (inset), we can identify

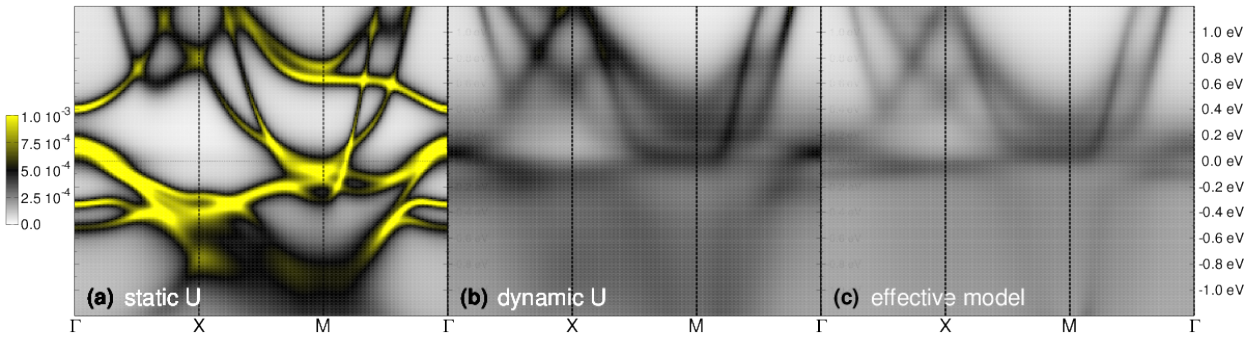


FIG. 16: Momentum-resolved spectral function for $K_xBa_{(1-x)}Fe_2As_2$ at optimal doping $x = 0.4$ and temperature $T = 600$ K. The left panel shows the LDA+DMFT result for the static interaction $U = U_{\rm scr}$, while the middle panel has been obtained using the frequency-dependent $U(\omega)$. The right panel shows the spectral function obtained in a simulation with $U = U_{\rm scr}$ and a bandwidth which is reduced by $Z_B = 0.59$. (From Ref. [95].)

these peaks in the spectral function computed with the procedure described in Sec. V. It is interesting to note that a satellite at approximately -6.5 eV has been seen in photoemission experiments [139, 140].

The middle panel also shows a comparison of the LDA+DMFT+$U(\omega)$ spectral function for optimally doped $BaFe_2As_2$ to the result obtained with LDA+DMFT using the static interaction parameter $U_{\rm scr} = U(\omega = 0)$ and to the LDA density of states. (A static Hund coupling parameter $J = 0.675$ was used in the DMFT calculations.) The much stronger renormalization of the quasi-particle peak in the dynamic-U calculation is due to the non-Fermi liquid self-energy in the spin-freezing crossover regime: Near optimal doping and for the simulation temperature of 145 K, the effective increase of the Coulomb interaction due to the barely screened fast charge fluctuations pushes the system closer to the spin-freezing region, resulting in large mass enhancements. In the underdoped regime, the behavior is more Fermi liquid like and the effect of the dynamic U on the electronic structure is less pronounced, while in the overdoped region, the spin-freezing leads to very short quasi-particle life-times. The location of the spin-freezing region in the space of doping and temperature is sketched in the right-hand panel of Fig. 15 (yellow region).

The calculated renormalized band structure of optimally doped $BaFe_2As_2$ is shown in Fig. 16 with the left panel plotting the result from the static-U approximation and the

middle panel the much more strongly renormalized and smeared out bands obtained in the dynamic-U simulation. As discussed in Sec. III D the proper static model involves an effectively reduced bandwidth. In the case of $BaFe_2As_2$ the renormalization factor $Z_B = 0.59$ is rather low [95]. The right hand panel of Fig. 16 shows the renormalized low-energy bands from a static-U calculation with such a renormalized bandwidth. Due to the enhanced correlation effects, we now get the proper mass enhancement and also the broadening of the bands due to the scattering with local moments. While the low-energy physics is correctly reproduced by the model with reduced bandwidth, this static description will of course not produce any high-energy satellites.

3. Mott gap and −13 eV satellite in La_2CuO_4

Low energy models of cuprates usually involve the Cu $d_{x^2-y^2}$ and O p_x and p_y orbitals. The one-band description considers the anti-bonding combination of these orbitals, while the three-band model also takes into account the bonding combination of Cu $d_{x^2-y^2}$ and O $p_{x,y}$, as well as the non-bonding p orbital. LDA+DMFT+$U(\omega)$ calculations based on the cRPA estimate of U have recently been analyzed for both models in Ref. [129]. The conclusion of this study was that in both models, a static approximation $U = U_{\rm scr}$ fails to open a Mott gap, while in the three-band model the dynamic-U calculations yields a gap of approximately 1.9 eV, in good agreement with experiment [141], *provided* that p-d interactions are accounted for within the DMFT self-consistency loop, at least at the Hartree level. The important role of interatomic Hartree potentials in the correct positioning of the p-bands and the opening of the gap is consistent with previous results [142] for a related three-band model.

The partially screened $U(\omega)$ for the three-band model of La_2CuO_4 is plotted in the left panel of Fig. 17. The broad peak in $\mathrm{Im}U(\omega)$ centered at $\omega = 30$ eV is a plasmon excitation coupled to single-particle excitations. At lower energies, $\mathrm{Im}U_{dd}$ exhibits a sharp peak at $\omega = 9$, which is absent in $\mathrm{Im}U_{pp}$ and $\mathrm{Im}U_{pd}$. This indicates that the collective excitation associated with the 9 eV peak is localized on the Cu site. The prominent 9 eV peak is primarily responsible for the low band renormalization factor $Z_B^{dd} = 0.52$, which suggests important screening effects in La_2CuO_4.

The **k**-integrated spectral function and its p-electron and d-electron contributions are plotted in the right hand panel of Fig. 17. At the simulated temperature of 1200 K, an-

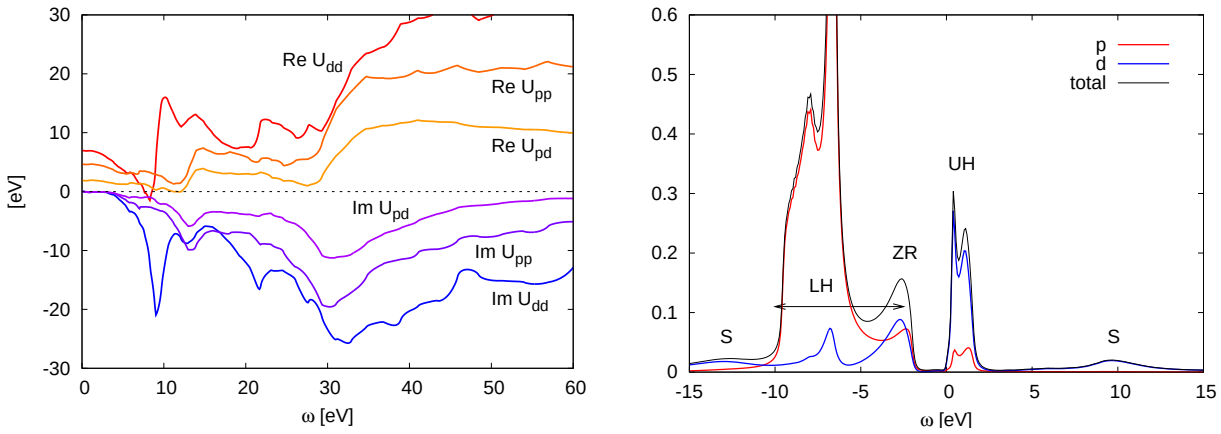


FIG. 17: Partially screened interactions from cRPA for the 3-band model of La_2CuO_4 (left panel) and spectral function at $T = 1200$ K from a LDA+DMFT+$U(\omega)$ simulation, which takes into account the interatomic Hartree potential (right panel). In the spectral function, we indicate the following features: satellites (S), lower Hubbard band (LH), upper Hubbard band (UH), and the Zhang-Rice singlet band (ZR). (Adapted from Ref. [129].)

tiferromagnetic correlations do not play an important role, so that the gap in the spectral function is a Mott gap. The upper Hubbard band has a width of about 2 eV, while the lower Hubbard band obtained in this simulation covers the same energy range as the p-bands and is hence not easily identified. The states near the lower gap edge, which have mixed p-d character, may be interpreted as Zhang-Rice singlet states [143]. The most interesting feature in this spectral function, as far as dynamical screening is concerned, are the two satellites at -13 eV and $+10$ eV. They originate from the sharp 9 eV peak in Im$U(\omega)$, and should not be confused with the Hubbard bands. A satellite feature at -13 eV has indeed been observed in photoemission measurements [144].

B. SEX+DMFT results for $BaCo_2As_2$

In the quest for new iron-based high-T_c superconductors, a significant effort has been devoted to alloying iron with other ferromagnetic $3d$ elements, such as Co and Ni. $Ba(Fe,Co)_2As_2$ and $Ba(Fe,Ni)_2As_2$ are superconducting, but with a lower T_c than the "parent" $BaFe_2As_2$ compound. While pristine $BaNi_2As_2$ is still a superconductor, $BaCo_2As_2$ is a paramagnetic metal close to a ferromagnetic instability, as suggested by a high Wilson

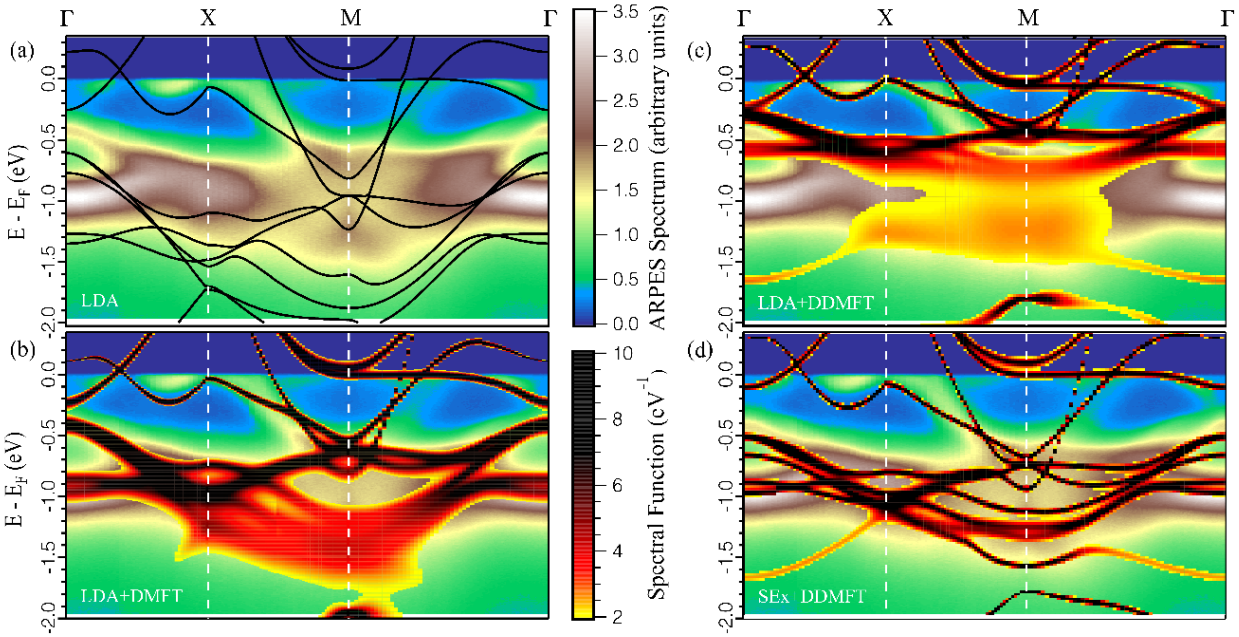


FIG. 18: LDA band structure of $BaCo_2As_2$ (panel (a)), and **k**-resolved spectral functions from LDA+DMFT (panel (b)), LDA+DMFT+$U(\omega)$ (dubbed LDA+DDMFT in panel (c)), and SEX+DMFT+$U(\omega)$ (dubbed SEx+DDMFT in panel (d)), overlaid on the experimental photoemission spectra. (Data taken from Ref. [112].)

ratio. The latter material is particularly interesting from the theoretical viewpoint, because it challenges *ab initio* methods to predict the correct magnetism and ARPES data. Density functional theory in the standard local spin density approximation (LSDA) gives a ferromagnetic ground state, which is not consistent with experiment. Moreover, the LDA bandwidth in the paramagnetic solution is a factor 1.5 too large compared to ARPES. The LDA density of states is peaked near the Fermi level, with a quite large value of 2.12 states/Co/spin/eV, which fulfills the Stoner criterion for ferromagnetism [145].

In Ref. [112], the SEX+DMFT scheme, presented in Sec. IV B 3, has been applied to $BaCo_2As_2$, in order to see whether a more refined treatment of electron correlations results in a better agreement with the experimental situation. On theoretical grounds, we expect $BaCo_2As_2$ to be less correlated than the superconducting $BaFe_2As_2$, because the nominal occupation of the d-orbital lattice site goes from the ideal spin-freezing value of 6 electrons in $BaFe_2As_2$ [110] to 7 in $BaCo_2As_2$. By moving farther away from half-filling, the onset of strong electron correlations is pushed up to larger values of U. Therefore, the electronic

structure of $BaCo_2As_2$ is supposed to be characterized by coherent quasiparticles, in contrast to $BaFe_2As_2$, where coherence is lost very quickly as the temperature increases, particularly in the hole-doped compounds (see Sec. VII A 2).

ARPES data confirm this scenario [146], by reporting quite sharp low-energy spectra for $BaCo_2As_2$, typical of a weakly-to-moderately correlated material, as shown in Fig. 18. A peculiar feature of its band structure is represented by the $d_{x^2-y^2}$ band, which is very flat along the Γ-M direction just below the empty part of the spectrum. This band contributes to a quite tall peak in the LDA density of states, exactly located at the Fermi level, and to the ferromagnetic nature of the LSDA solution.

The situation encountered here is common in iron-based superconductors, where the tendency to magnetism is largely overestimated by density functional theory. In this sense, it is useful to perform a detailed study of $BaCo_2As_2$ as a benchmark system. The authors of Ref. [112] tested LDA+DMFT calculations of different flavors, namely LDA+DMFT with the cRPA static U, LDA+DMFT+$U(\omega)$, and SEX+DMFT+$U(\omega)$. The resulting spectral functions are shown in Fig. 18. It was found that the regular DFT+DMFT performs quite well, whereas the dynamic U worsens the DFT+DMFT results particularly around the M $\mathbf{k}$-point and below -0.5 eV, due to a too large band renormalization. On the other hand, these features are corrected by the SEX+DMFT+$U(\omega)$, as the Z_B band narrowing is compensated by non-local correlation effects included in the SEX part, which yields instead a band widening, as it is apparent in Fig. 19.

Therefore, both ingredients, the dynamically screened U and the non-local screened exchange, are essential for a consistent description of this moderately correlated material. Electron correlations included in the non-perturbative solution of the impurity problem with retarded U are key to the broadening of the spectral function peak at the Fermi level (Fig. 19), which results in a density of states below the Stoner threshold. One thus recovers the correct paramagnetic phase in agreement with experimental conditions. SEX+DMFT is a promising scheme that should be applied to other strongly correlated compounds for further benchmarks and predictions.

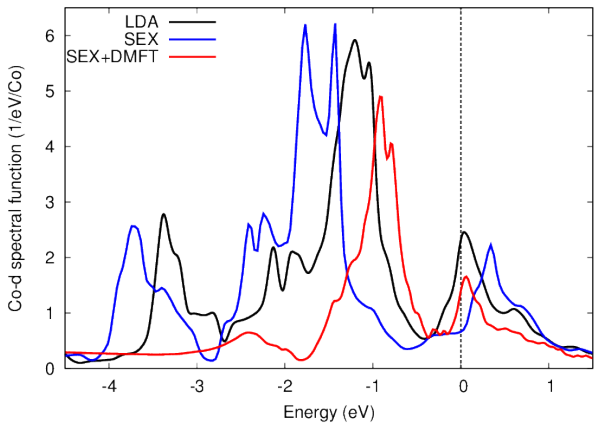


FIG. 19: Cobalt-d spectral function of of $BaCo_2As_2$ from SEX+DMFT+$U(\omega)$ (red), compared to the Co-d density of states within LDA (black), and SEX (solid blue line). (Data taken from Ref. [112].)

C. GW+DMFT results for $SrVO_3$

1. *Band widening from k-dependent* Σ

The simplest way of combining GW and DMFT is to add the local self-energy of a converged LDA+DMFT+$U(\omega)$ calculation to the nonlocal self-energy from a separate GW calculation [133]. To avoid a double-counting of interaction effects, the local component of the GW self-energy must be subtracted. Figure 20 compares the resulting quasi-particle bandstructure of $SrVO_3$, obtained as the solution of the quasi-particle equation $E_{\alpha,\mathbf{k}} - \epsilon_{\alpha,\mathbf{k}} - \mathrm{Re}\Sigma_{\alpha,\alpha}(k, E_{\alpha,\mathbf{k}}) = 0$, to LDA, GW and LDA+DMFT+$U(\omega)$ data. The bandwidth of 1.2 eV predicted by the one-shot GW+DMFT scheme is in good agreement with photoemission data [130]. In particular, the one-shot GW+DMFT corrects the overestimation of the correlation effect in LDA+DMFT+$U(\omega)$ (Sec. VII A 1), while producing a substantial renormalization of the GW bandstructure, especially in the unoccupied part of the spectrum. This is illustrated in the lower panel, where a rescaled GW quasiparticle bandstructure is compared to the one-shot GW+DMFT result. Note that the stronger renormalization of the bands in the unoccupied part is the result of the *local* self-energy, while the overall GW+DMFT band structure is wider than the DMFT one, because of the nonlocal self-energy components coming from the GW part.

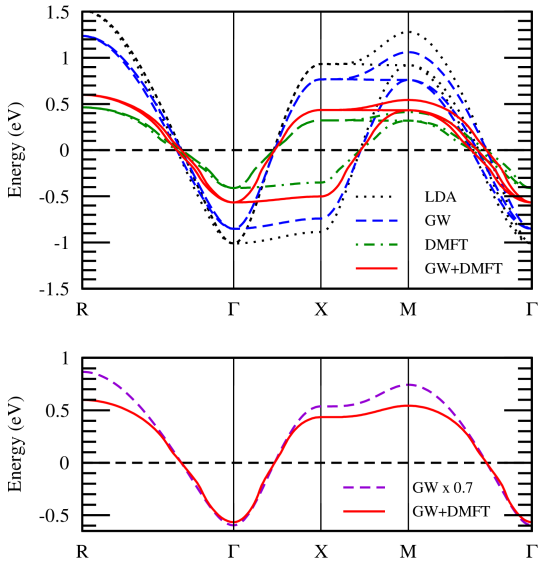


FIG. 20: Bare and renormalized quasi-particle bandstructures of $SrVO_3$ obtained from different approximate methods. DMFT here means the LDA+DMFT+$U(\omega)$ scheme, GW+DMFT the one-shot result. (From Ref. [133].)

It has been argued in Ref. [113] that the partial cancellation between the band-narrowing effect of a dynamically screened interaction (Sec. III D) and the band-widening effect of the nonlocal self-energy contributions is a generic phenomenon, which highlights the advantage of formalisms such as GW+DMFT, which incorporate both effects. In fact, it is useful and instructive to analyze the band widening effect due to the nonlocal exchange at the GW level. A one-shot GW calculation of $SrVO_3$ starting from the LDA band structure and wavefunctions produces the t_{2g} spectral function shown in the left panel of Fig. 21. The GW bandwidth is renormalized with respect to LDA, such that the effective mass is increased by a factor $m_{\rm GW}/m_{\rm LDA} = 1.3$. However, the quasiparticle weight $Z_{\mathbf{k}_F} = 1/\left(1 - \partial_\omega {\rm Re}\Sigma_{\rm GW}(\mathbf{k}_F, \omega)\right)_{\omega=0}$ is ~ 0.53, where the self-energy is defined with respect to the LDA exchange-correlation potential: $\Sigma_{\rm GW} = \Sigma^{\rm xc}_{\rm GW} - V^{\rm xc}_{\rm LDA}$. This would give a mass enhancement of ~ 2 in the absence of non-local self-energy effects. However, the expression for the group velocity within GW, from where the total mass enhancement is extracted, reads:

$$\frac{dE_{\mathbf{k}i}}{dk_\alpha} = \left. \frac{\langle \Psi_{\mathbf{k}i} | \partial_{k_\alpha} \left(H_{LDA}(\mathbf{k}) + {\rm Re}\Sigma_{GW}(\mathbf{k},\omega) \right) | \Psi_{\mathbf{k}i} \rangle}{\left(1 - \langle \Psi_{\mathbf{k}i} | \partial_\omega {\rm Re}\Sigma_{GW}(\mathbf{k},\omega) | \Psi_{\mathbf{k}i} \rangle\right)} \right|_{k=k_F, \omega=0}, \tag{137}$$

where the additional renormalization via the *nonlocality* of the self-energy, $\partial_{k_\alpha} {\rm Re}\Sigma(\mathbf{k},\omega)$,

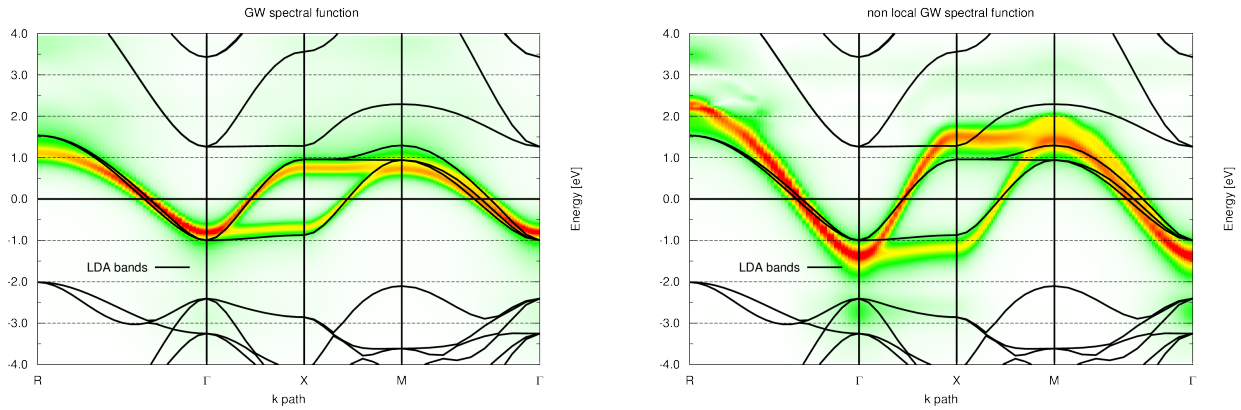


FIG. 21: Momentum resolved spectral function of $SrVO_3$ obtained from the GW approximation (left panel) and by taking into account only the *nonlocal* part of the GW self-energy (right panel). Superimposed is the LDA band structure. (From Ref. [108].)

must be taken into account.

In order to illustrate and quantify the effect of the nonlocal components, one can remove the local part from $\Sigma^{\rm xc}_{\rm GW}$ by defining $\Sigma^{\rm nonloc}_{\rm GW}(\mathbf{k},\omega) = \Sigma^{\rm xc}_{\rm GW}(\mathbf{k},\omega) - \sum_{\mathbf{k}} \Sigma^{\rm xc}_{\rm GW}(\mathbf{k},\omega)$. The spectral function of the corresponding Green's function $\tilde{G}(\mathbf{k},\omega) = 1/[\omega + \tilde{\mu} - H_{\rm LDA}(\mathbf{k}) + V^{\rm xc}_{\rm LDA} - \Sigma^{\rm nonloc}_{\rm GW}(\mathbf{k},\omega)]$ is plotted in the right panel of Fig. 21. It is apparent that non-local contributions, which mainly come from the exchange part, lead to a significant band widening, yielding a bandwidth ≈ 1.5 times larger than LDA. We also note a small asymmetry in the band-widening, that is, the effect is more prominent in the empty part of the spectrum, as pointed out in Refs. [108] and [112].

Another noteworthy feature of the GW self-energy of $SrVO_3$ is the separation of the local and non-local self-energy effects into dynamic and static ones, respectively. A way to quantify the non-locality of dynamical renormalizations is to compute the generalized $\mathbf{k}$-dependent quasiparticle weight

$$Z_{\mathbf{k}}(\omega) = \left[1 - \frac{\partial {\rm Re}\Sigma(\mathbf{k},\omega)}{\partial \omega}\right]^{-1}, \tag{138}$$

and its $\mathbf{k}$-fluctuations, defined by

$$\Delta_k Z = \sqrt{\sum_{\mathbf{k}} {\rm Tr}|Z_{\mathbf{k}}(\omega) - Z^{\rm loc}(\omega)|^2}, \tag{139}$$

where the local quantity is, as usual, $Z^{\rm loc}(\omega) = \sum_{\mathbf{k}} Z_{\mathbf{k}}(\omega)$. $\Delta_k Z$ and $Z^{\rm loc}(0)$ are plotted in the bottom panel of Fig. 22. It turns out that the $\mathbf{k}$-dispersion of $Z_{\mathbf{k}}$ around $Z^{\rm loc}$ is

very weak in the frequency window from -2 to 2 eV, signaling that dynamical effects are *local* at low-energy. Conversely, *non-local* effects are static in the same energy window. This is confirmed by the inspection of the real and imaginary parts of the GW self-energy, plotted for some selected high symmetry **k**-points in the top and middle panels of Fig. 22, respectively. One easily sees that at low energy the frequency dependence is **k**-insensitive in both the real and imaginary parts, while the **k**-dependence is ω-independent in the real part, leading to a **k**-dependent rigid shift of the self-energy curves. This effect has not only been observed in $SrVO_3$ [108, 147], but also in the iron pnictides and chalcogenides [116].

We come back to the asymmetry between the occupied and empty parts of the spectrum, which results from the non-local part of the self-energy. This asymmetry is not only present in the band widening, as seen in Fig. 21, but most prominently in the quasiparticle lifetimes. Indeed, the imaginary part of the GW self-energy is largest on the unoccupied orbitals for $\omega > 0$, as shown in the middle panel of Fig. 22, which implies a stronger effect of electron-

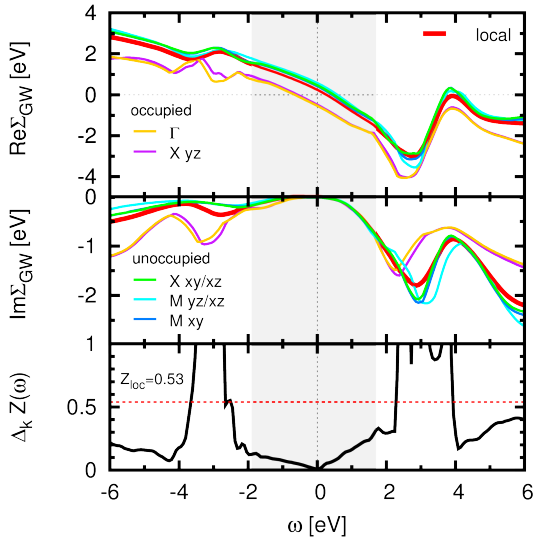


FIG. 22: The GW self-energy of $SrVO_3$ at several high symmetry points resolved into the three t_{2g} (Wannier) orbital contributions as a function of frequency. Also shown is the local projection (real parts: top panel, imaginary parts: middle panel). The lower panel displays the momentum dependence of the frequency dependent generalization of the quasi-particle weight. The origin of energy corresponds to the Fermi level and the shaded area roughly indicates the Fermi liquid regime within GW. (From Ref. [108].)

electron scattering in the empty part of the spectrum. However, this large imaginary part lies outside the energy window where the dynamic and static effects are separable in frequency. Hence, the asymmetry of the quasiparticle lifetime, a dynamic quantity in nature, *is* **k**-dependent.

2. Self-consistent calculation of Σ

The partially self-consistent implementation of Refs. [108, 109] goes a step beyond the one-shot calculation discussed in the previous subsection by performing a self-consistency loop for Σ and G. However, compared to the full GW+DMFT scheme discussed in Sec. IV A 2, a number of approximations have been made. The bosonic Weiss field $\mathcal{U}$ was kept frozen to the $U_{mn}(\mathbf{0}, \omega)$ cRPA value, as described in Sec. IV B 2. In other words, the self-consistency loop for P and W was not performed. However, the RPA polarization function computed from the LDA band structure of $SrVO_3$, and its corresponding dielectric function, compare favorably to electron energy loss spectroscopy measurements of $SrTiO_3$, an isostructural compound with a d^0 occupation, where data of this kind are available up to 40 eV.

The results for the GW and the GW+DMFT spectra are shown in Fig. 23. The dynamically screened impurity problem of GW+DMFT has been solved by DALA. Compared to LDA, the GW spectral function, plotted in the leftmost panel of Fig. 23, gives a better position of the O-2p and Sr-4d states, which are closer to the experimental photoemission spectroscopy (PES) and Bremsstrahl-Isochromat spectroscopy (BIS) curves taken from Refs. [148] and [149]. However, GW yields a too strong quasiparticle peak at the Fermi level, of full t_{2g} character, and a too weak mass enhancement. GW+DMFT, reported in the middle panel of Fig. 23, corrects for these deficiencies, by strongly renormalizing the height of this peak, and producing a mass enhancement of ~ 2. The renormalization is accompanied by a spectral weight transfer from the quasiparticle peak to the lower Hubbard band, correctly located at -1.6 eV (see rightmost panel in Fig. 23), and to plasmon satellites, which can be identified in the figure at -4 eV, 5 eV, and 15 eV. Therefore, dynamic screening and correlation effects play a major role in determining the renormalized low-energy properties of the material.

Surprisingly, the upper Hubbard band is not visible in the GW+DMFT spectral function computed in Refs. [108, 109]. It may be hidden by non-local self-energy effects, particu-

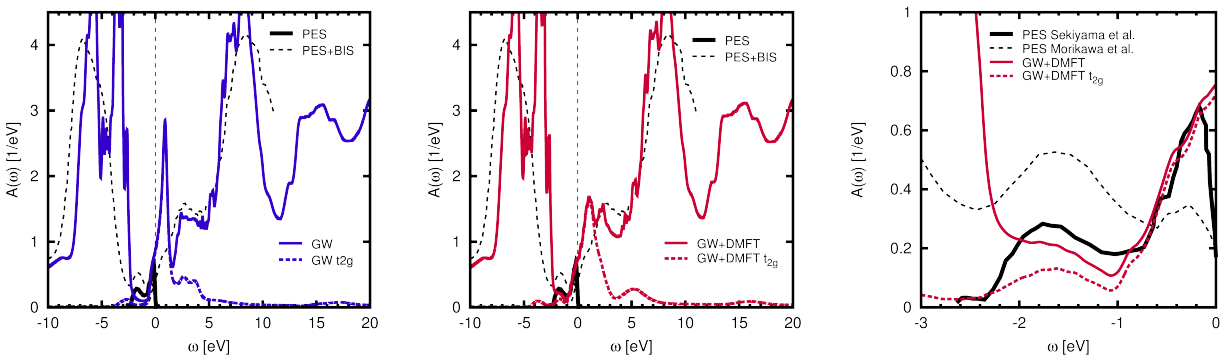


FIG. 23: GW (left panel) and GW+DMFT (middle panel) spectral functions of $SrVO_3$ in comparison to photoemission and inverse photoemission spectra. Right panel: Zoom of the middle panel around the lower Hubbard band region. (From Ref. [108].)

larly large in the empty part of the spectrum. However, other calculations, such as the one-shot GW+DMFT scheme of Ref. [133], or the simplified SEX+DMFT [147], both using a CTQMC solver, show a quite sharp upper Hubbard band well separated from the quasiparticle peak. The missing Hubbard band could thus also be a consequence of an underestimation of the bandwidth reduction by DALA with respect to QMC (reported in Ref. [128]), or by non-local dynamical self-energy effects just above the Fermi liquid regime, which are neglected in Ref. [147] and treated non-selfconsistently in Ref. [133].

In any case, within the partially self-consistent GW+DMFT scheme of Refs. [108, 109] the upper Hubbard band should be located around 2 eV, as its separation from the lower one must be the *static* value of U (here 3.3 eV). This implies that the BIS signal detected at 2.7 eV is *not* the upper Hubbard band of the t_{2g} manifold, as previously identified. Overlapping the GW+DMFT spectrum with the BIS data shows that the peak just above the Fermi level has an e_g origin, instead, as seen in Fig. 23.

VIII. CONCLUSIONS AND OUTLOOK

We have discussed the effect of dynamical screening in strongly correlated lattice systems and materials, and detailed some recently developed or implemented techniques based on extensions of the DMFT framework. At this point, the most advanced scheme which allows a self-consistent treatment of screening and correlation effects in materials is the combination of the GW *ab initio* method and DMFT [10]. A fully self-consistent GW+DMFT

calculation yields retarded interaction parameters for the DMFT impurity problem, which incorporate the effect of local and nonlocal screening processes in the correlated system. This method also captures the momentum dependence of the self-energy (at the GW level), and hence the competition between the band-narrowing effect of the frequency-dependent interaction and the band-widening effect of the non-local self-energy components. Self-consistent GW+DMFT calculations of multi-band systems and realistic materials have only been implemented very recently. While these results demonstrate prominent non-local screening effects, more work on a broad range of materials is needed to judge the reliability and predictive power of the scheme. Also, it should be emphasized that in current implementations, the self-consistent calculation is performed within a low-energy window containing just a few bands, after a cRPA downfolding or one-shot GW calculation. In the near future, this scheme should be extended to a multi-scale approach with three energy windows, a large energy window for the initial cRPA calculation, an intermediate-energy window for self-consistent GW calculations, and a low-energy window for the GW+DMFT calculations. In such a scheme, the GW+DMFT estimate of the self-energy of the low-energy space has to be merged with the GW self-energy for the remaining orbitals in the intermediate-energy window, and the calculations within the intermediate and low-energy space should be iterated until a self-consistent solution for G, W, and the auxiliary impurity problem is obtained.

Apart from the implementation of these hopefully accurate, but numerically demanding schemes, the further exploration of simplified versions of the GW+DMFT framework will produce useful insights into the effects of screening and nonlocal correlations. We have discussed the partially self-consistent formulation of Tomczak *et al.*, which performs a self-consistency loop on Σ and G, while approximating the effective interaction by the cRPA estimate [108]. If the self-energy is furthermore approximated as local, one ends up with the LDA+DMFT+$U(\omega)$ method, which has been used in recent years by several groups to study plasmon satellites in strongly correlated materials [110, 128, 129, 133]. Another recently proposed variant, which has been applied to correlated materials with promising results, is SEX+DMFT+$U(\omega)$, which takes into account the band-widening effect of the nonlocal screened exchange [112]. Further applications and comparisons of these different simplified schemes will provide valuable insights into the roles played by the different ingredients of the GW+DMFT formalism, and the importance of self-consistency.

It is also essential to clarify the accuracy and limitations of the cRPA method, or related

RPA schemes, which underpin the material simulations discussed in this review. The RPA polarization lacks vertex corrections, and in principle, a downfolding onto a low-energy subspace should generate higher-order interaction terms which are not contained in an effective Hubbard model description. Some of these issues have recently been addressed in simple model set-ups containing a small number of screening bands [47, 48], but more work is needed to properly judge the realistic situation with a large number of high-energy screening bands.

It should be kept in mind that GW+DMFT and related methods, which combine the local self-energy from an effective impurity model with the nonlocal self-energy of some weak-coupling perturbation theory, cannot be expected to capture the strong nonlocal correlation effects in low dimensional systems. This has been explicitly demonstrated for the two-dimensional Hubbard model in the weak-coupling regime [22], while at intermediate coupling, there are obvious inconsistencies between the weakly momentum-dependent GW+DMFT results, and the strong momentum-variation predicted by cluster DMFT simulations [18, 150]. Hence, we should view GW+DMFT primarily as a method which is suitable for capturing dynamical screening effects in three dimensional compounds. For two-dimensional systems, the combination of (extended) cluster DMFT and many-body perturbation theory may be a promising strategy. However, efficient impurity solvers capable of handling dynamically screened interactions in cluster impurity problems have yet to be developed.

In fact, progress in this field is intricately linked to futher improvements of the available impurity solvers and analytical continuation techniques. The methods reviewed in this paper enable an efficient simulation of single-site, multi-orbital impurity problems with dynamically screened monopole interactions. Retarded spin-flip terms cannot be handled efficiently with methods based on a Lang-Firsov decoupling of the electron-boson interaction and must be dealt with in a double-expansion approach [97, 151], which may suffer from a sign problem. The analytical continuation procedure explained in Sec. V is also based on a Lang-Firsov picture, and works reliably only in systems with a clear energy separation between low-energy and satellite features. More flexible and powerful methods will be essential in particular for the eventual application of more advanced schemes, such as TRILEX [152], dual bosons [105], or extended cluster methods to realistic materials.

Another new and interesting research direction is the extension of the methods described here to nonequilibrium systems [124, 125]. A proper description of dynamical screening

effects should be very important in materials perturbed by intense laser fields, especially if the laser pulse produces inter-band transitions. GW+DMFT is a promising starting point for the development of a formalism, which enables *ab initio* predictions of nonequilibrium phenomena in strongly correlated materials.

Acknowledgements

We would like to thank F. Aryasetiawan, T. Ayral, S. Biermann, L. Boehnke, V. Brouet, M. Eckstein, D. Golez, J. Gukelberger, L. Huang, A. J. Millis, F. Nilsson, T. Miyake, Y. Nomura, R. Sakuma, A. van Roekeghem, H. Shinaoka, J. Tomczak, and L. Vaugier for helpful discussions and close collaborations on the topics covered in this review. PW acknowledges support from ERC starting grant 278023. Some of the results presented in this review were obtained using HPC resources from GENCI 096493 allocation.

---

[1] L. Hedin, Phys. Rev. **139**, A796 (1965).

[2] F. Aryasetiawan and O. Gunnarsson, Rep. Prog. Phys. **61**, 237 (1998).

[3] L. Hedin, J. Phys.: Condens. Matter **11**, R489 (1999).

[4] G. Onida, L. Reining, and A. Rubio, Rev. Mod. Phys. **74**, 601 (2002).

[5] S.-P. Jeng, R. J. Lad, and V. E. Henrich, Phys. Rev. B **43**, 11971 (1991).

[6] L. Marton, J. A. Simpson, H. A. Fowler, and N. Swanson, Phys. Rev. **126**, 182 (1962).

[7] F. Aryasetiawan, L. Hedin, and K. Karlsson, Phys. Rev. Lett. **77**, 2268 (1996).

[8] M. Guzzo, G. Lani, F. Sottile, P. Romaniello, M. Gatti, J. J. Kas, J. J. Rehr, M. G. Silly, F. Sirotti, and L. Reining, Phys. Rev. Lett. **107**, 166401 (2011).

[9] E. Gull, A. J. Millis, A. I. Lichtenstein, A. N. Rubtsov, M. Troyer, and P. Werner, Rev. Mod. Phys. **83**, 349 (2011).

[10] S. Biermann, F. Aryasetiawan, and A. Georges, Phys. Rev. Lett. **90**, 086402 (2003).

[11] D. Zgid and G. K.-L. Chan, The Journal of Chemical Physics **134**, 094115 (2011).

[12] A. A. Kananenka, E. Gull, and D. Zgid, Phys. Rev. B **91**, 121111 (2015).

[13] T. N. Lan, A. A. Kananenka, and D. Zgid, The Journal of Chemical Physics **143**, 241102 (2015).

[14] D. Zgid, E. Gull, and G. K.-L. Chan, Phys. Rev. B **86**, 165128 (2012).

[15] A. Go and A. J. Millis, Phys. Rev. Lett. **114**, 016402 (2015).

[16] T. Maier, M. Jarrell, T. Pruschke, and M. H. Hettler, Rev. Mod. Phys. **77**, 1027 (2005).

[17] L. F. Tocchio, F. Becca, A. Parola, and S. Sorella, Phys. Rev. B **78**, 041101 (2008).

[18] P. Werner, E. Gull, O. Parcollet, and A. J. Millis, Phys. Rev. B **80**, 045120 (2009).

[19] E. Gull, O. Parcollet, P. Werner, and A. J. Millis, Phys. Rev. B **80**, 245102 (2009).

[20] C.-C. Chang and S. Zhang, Phys. Rev. Lett. **104**, 116402 (2010).

[21] H. Shi and S. Zhang, Phys. Rev. B **88**, 125132 (2013).

[22] J. Gukelberger, L. Huang, and P. Werner, Phys. Rev. B **91**, 235114 (2015).

[23] B.-X. Zheng and G. K.-L. Chan, arXiv:1504.01784 (2015).

[24] J. P. F. LeBlanc and et al., arXiv:1505.02290 (2015).

[25] M. Imada and T. Miyake, Journal of the Physical Society of Japan **79**, 112001 (2010).

[26] M. Hirayama, T. Miyake, and M. Imada, Phys. Rev. B **87**, 195144 (2013).

[27] P. Hohenberg and W. Kohn, Phys. Rev. **136**, B864 (1964).

[28] W. Kohn and L. J. Sham, Phys. Rev. **140**, A1133 (1965).

[29] R. O. Jones, Rev. Mod. Phys. **87**, 897 (2015).

[30] N. Marzari and D. Vanderbilt, Phys. Rev. B **56**, 12847 (1997).

[31] T. Miyake and F. Aryasetiawan, Phys. Rev. B **77**, 085122 (2008).

[32] F. Aryasetiawan, M. Imada, A. Georges, G. Kotliar, S. Biermann, and A. I. Lichtenstein, Phys. Rev. B **70**, 195104 (2004).

[33] F. Aryasetiawan, K. Karlsson, O. Jepsen, and U. Schönberger, Phys. Rev. B **74**, 125106 (2006).

[34] M. Springer and F. Aryasetiawan, Phys. Rev. B **57**, 4364 (1998).

[35] E. Şaşıoğlu, C. Friedrich, and S. Blügel, Phys. Rev. B **83**, 121101 (2011).

[36] R. Sakuma and F. Aryasetiawan, private communication (2013).

[37] T. Miyake, L. Pourovskii, V. Vildosola, S. Biermann, and A. Georges, Journal of the Physical Society of Japan **77**, 99 (2008).

[38] K. Nakamura, R. Arita, and M. Imada, Journal of the Physical Society of Japan **77**, 093711 (2008).

[39] J. M. Tomczak, T. Miyake, R. Sakuma, and F. Aryasetiawan, Phys. Rev. B **79**, 235133 (pages 8) (2009).

[40] T. Miyake, K. Nakamura, R. Arita, and M. Imada, Journal of the Physical Society of Japan **79**, 044705 (2010).

[41] J. M. Tomczak, T. Miyake, and F. Aryasetiawan, Phys. Rev. B **81**, 115116 (2010).

[42] Y. Nomura, K. Nakamura, and R. Arita, Phys. Rev. B **85**, 155452 (2012).

[43] L. Vaugier, H. Jiang, and S. Biermann, Phys. Rev. B **86**, 165105 (2012).

[44] R. Sakuma and F. Aryasetiawan, Phys. Rev. B **87**, 165118 (2013).

[45] I. Souza, N. Marzari, and D. Vanderbilt, Phys. Rev. B **65**, 035109 (2001).

[46] T. Miyake, F. Aryasetiawan, and M. Imada, Phys. Rev. B **80**, 155134 (2009).

[47] M. Kinza and C. Honerkamp, Phys. Rev. B **92**, 045113 (2015).

[48] H. Shinaoka, M. Troyer, and P. Werner, Phys. Rev. B **91**, 245156 (2015).

[49] M. Cococcioni and S. de Gironcoli, Phys. Rev. B **71**, 035105 (2005).

[50] H. Hsu, K. Umemoto, M. Cococcioni, and R. Wentzcovitch, Phys. Rev. B **79**, 125124 (2009).

[51] V. I. Anisimov and O. Gunnarsson, Phys. Rev. B **43**, 7570 (1991).

[52] V. I. Anisimov, D. M. Korotin, M. A. Korotin, A. V. Kozhevnikov, J. Kunes, A. O. Shorikov, S. L. Skornyakov, and S. V. Streltsov, Journal of Physics: Condensed Matter **21**, 075602 (2009).

[53] A. Kutepov, K. Haule, S. Y. Savrasov, and G. Kotliar, Phys. Rev. B **82**, 045105 (2010).

[54] Y. Nomura, M. Kaltak, K. Nakamura, C. Taranto, S. Sakai, A. Toschi, R. Arita, K. Held, G. Kresse, and M. Imada, Phys. Rev. B **86**, 085117 (2012).

[55] V. I. Anisimov, J. Zaanen, and O. K. Andersen, Phys. Rev. B **44**, 943 (1991).

[56] V. I. Anisimov, F. Aryasetiawan, and A. I. Lichtenstein, Journal of Physics: Condensed Matter **9**, 767 (1997).

[57] G. Kotliar, S. Y. Savrasov, K. Haule, V. S. Oudovenko, O. Parcollet, and C. A. Marianetti, Rev. Mod. Phys. **78**, 865 (2006).

[58] M. Aichhorn, L. Pourovskii, and A. Georges, Phys. Rev. B **84**, 054529 (2011).

[59] K. Haule, Phys. Rev. Lett. **115**, 196403 (2015).

[60] K. Haule, C.-H. Yee, and K. Kim, Phys. Rev. B **81**, 195107 (2010).

[61] P. Hansmann, T. Ayral, L. Vaugier, P. Werner, and S. Biermann, Phys. Rev. Lett. **110**, 166401 (2013).

[62] M. Imada and Y. Hatsugai, Journal of the Physical Society of Japan **58**, 3752 (1989).

[63] S. Zhang and H. Krakauer, Phys. Rev. Lett. **90**, 136401 (2003).

[64] S. Sorella, Phys. Rev. B **71**, 241103 (2005).

[65] D. Tahara and M. Imada, Journal of the Physical Society of Japan **77**, 114701 (2008).

[66] S. Sorella, Y. Otsuka, and S. Yunoki, Scientific Reports **2**, 992 (2012).

[67] J. Jordan, R. Orús, G. Vidal, F. Verstraete, and J. I. Cirac, Phys. Rev. Lett. **101**, 250602 (2008).

[68] P. Corboz, T. M. Rice, and M. Troyer, Phys. Rev. Lett. **113**, 046402 (2014).

[69] P. Corboz, arxiv:1508.04003 (2015).

[70] M. Potthoff, M. Aichhorn, and C. Dahnken, Phys. Rev. Lett. **91**, 206402 (2003).

[71] G. Kotliar, S. Y. Savrasov, G. Pálsson, and G. Biroli, Phys. Rev. Lett. **87**, 186401 (2001).

[72] M. H. Hettler, A. N. Tahvildar-Zadeh, M. Jarrell, T. Pruschke, and H. R. Krishnamurthy, Phys. Rev. B **58**, R7475 (1998).

[73] A. Georges, G. Kotliar, W. Krauth, and M. J. Rozenberg, Rev. Mod. Phys. **68**, 13 (1996).

[74] A. Georges and G. Kotliar, Phys. Rev. B **45**, 6479 (1992).

[75] W. Metzner and D. Vollhardt, Phys. Rev. Lett. **62**, 324 (1989).

[76] E. Müller-Hartmann, Zeitschrift für Physik B Condensed Matter **74**, 507 (1989).

[77] W. Koller, D. Meyer, Y. no, and A. C. Hewson, EPL **66**, 559 (2004).

[78] W. Koller, D. Meyer, and A. C. Hewson, Phys. Rev. B **70**, 155103 (2004).

[79] G. S. Jeon, T.-H. Park, J. H. Han, H. C. Lee, and H.-Y. Choi, Phys. Rev. B **70**, 125114 (2004).

[80] W. Koller, D. Meyer, A. Hewson, and Y. no, Physica B: Condensed Matter **359361**, 795 (2005), ISSN 0921-4526, proceedings of the International Conference on Strongly Correlated Electron Systems.

[81] P. Barone, R. Raimondi, M. Capone, and C. Castellani, Phys. Rev. B **73**, 085120 (2006).

[82] J. K. Freericks and M. Jarrell, Phys. Rev. B **50**, 6939 (1994).

[83] Y. Murakami, P. Werner, N. Tsuji, and H. Aoki, Phys. Rev. B **88**, 125126 (2013).

[84] Y. Murakami, P. Werner, N. Tsuji, and H. Aoki, Phys. Rev. Lett. **113**, 266404 (2014).

[85] M. Casula, A. Rubtsov, and S. Biermann, Phys. Rev. B **85**, 035115 (2012).

[86] I. G. Lang and Y. A. Firsov, Sov. Phys. JETP **16**, 1301 (1962).

[87] P. Werner, A. Comanac, L. de' Medici, M. Troyer, and A. J. Millis, Phys. Rev. Lett. **97**, 076405 (2006).

[88] P. Werner and A. J. Millis, Phys. Rev. B **74**, 155107 (2006).

[89] P. Werner and A. J. Millis, Phys. Rev. Lett. **99**, 146404 (2007).

[90] G. D. Mahan, *Many-particle Physics* (Plenum Press, 1990).

[91] H. Hafermann, K. R. Patton, and P. Werner, Phys. Rev. B **85**, 205106 (2012).

[92] H. Hafermann, Phys. Rev. B **89**, 235128 (2014).

[93] P. Werner and A. J. Millis, Phys. Rev. Lett. **104**, 146401 (2010).

[94] T. Ayral, S. Biermann, and P. Werner, Phys. Rev. B **87**, 125149 (2013).

[95] M. Casula, P. Werner, L. Vaugier, F. Aryasetiawan, T. Miyake, A. J. Millis, and S. Biermann, Phys. Rev. Lett. **109**, 126408 (2012).

[96] M. Capone, M. Fabrizio, C. Castellani, and E. Tosatti, Rev. Mod. Phys. **81**, 943 (2009).

[97] K. Steiner, Y. Nomura, and P. Werner, Phys. Rev. B **92**, 115123 (2015).

[98] A. M. Sengupta and A. Georges, Phys. Rev. B **52**, 10295 (1995).

[99] Q. Si and J. L. Smith, Phys. Rev. Lett. **77**, 3391 (1996).

[100] P. Sun and G. Kotliar, Phys. Rev. B **66**, 085120 (2002).

[101] J. W. Negele and H. Orland, *Quantum Many-Particle Systems* (Westview Press, 1988).

[102] T. Ayral, P. Werner, and S. Biermann, Phys. Rev. Lett. **109**, 226401 (2012).

[103] L. Huang, T. Ayral, S. Biermann, and P. Werner, Phys. Rev. B **90**, 195114 (2014).

[104] N. Prokof'ev and B. Svistunov, Phys. Rev. Lett. **99**, 250201 (2007).

[105] A. Rubtsov, M. Katsnelson, and A. Lichtenstein, Annals of Physics **327**, 1320 (2012).

[106] E. Stepanov, E. van Loon, A. Katanin, A. Lichtenstein, M. Katsnelson, and A. Rubtsov, arxiv:1508.07237 (2015).

[107] A. N. Rubtsov, M. I. Katsnelson, and A. I. Lichtenstein, Phys. Rev. B **77**, 033101 (2008).

[108] J. M. Tomczak, M. Casula, T. Miyake, and S. Biermann, Phys. Rev. B **90**, 165138 (2014).

[109] J. M. Tomczak, M. Casula, T. Miyake, F. Aryasetiawan, and S. Biermann, EPL **100**, 67001 (2012).

[110] P. Werner, M. Casula, T. Miyake, F. Aryasetiawan, A. J. Millis, and S. Biermann, Nat. Phys. pp. 1745–2481 (2012).

[111] S. Biermann, Journal of Physics: Condensed Matter **26**, 173202 (2014).

[112] A. van Roekeghem, T. Ayral, J. M. Tomczak, M. Casula, N. Xu, H. Ding, M. Ferrero, O. Parcollet, H. Jiang, and S. Biermann, Phys. Rev. Lett. **113**, 266403 (2014).

[113] T. Miyake, C. Martins, R. Sakuma, and F. Aryasetiawan, Phys. Rev. B **87**, 115110 (2013).

[114] R. Sakuma, C. Martins, T. Miyake, and F. Aryasetiawan, Phys. Rev. B **89**, 235119 (2014).

[115] T. Schäfer, A. Toschi, and J. M. Tomczak, Phys. Rev. B **91**, 121107 (2015).

[116] J. M. Tomczak, M. van Schilfgaarde, and G. Kotliar, Phys. Rev. Lett. **109**, 237010 (2012).

[117] C. Taranto, M. Kaltak, N. Parragh, G. Sangiovanni, G. Kresse, A. Toschi, and K. Held, Phys. Rev. B **88**, 165119 (2013).

[118] M. van Schilfgaarde, T. Kotani, and S. Faleev, Phys. Rev. Lett. **96**, 226402 (2006).

[119] T. Kotani, M. van Schilfgaarde, and S. V. Faleev, Phys. Rev. B **76**, 165106 (2007).

[120] S. Choi, A. Kutepov, K. Haule, M. van Schilfgaarde, and G. Kotliar, arXiv:1504.07569v1 (2015).

[121] F. Gygi and A. Baldereschi, Phys. Rev. Lett. **62**, 2160 (1989).

[122] H. Vidberg and J. Serene, J. Low Temp. Phys. **29**, 179 (1977).

[123] M. Jarrell and J. E. Gubernatis, Physics Reports **269**, 133 (1996).

[124] D. Golež, M. Eckstein, and P. Werner, Phys. Rev. B **92**, 195123 (2015).

[125] H. Aoki, N. Tsuji, M. Eckstein, M. Kollar, T. Oka, and P. Werner, Rev. Mod. Phys. **86**, 779 (2014).

[126] M. Eckstein and P. Werner, Phys. Rev. Lett. **110**, 126401 (2013).

[127] E. Tosatti and P. W. Anderson, Jpn. J. Appl. Phys. **13**, 381 (1974).

[128] L. Huang and Y. Wang, EPL **99**, 67003 (2012).

[129] P. Werner, R. Sakuma, F. Nilsson, and F. Aryasetiawan, Phys. Rev. B **91**, 125142 (2015).

[130] T. Yoshida, M. Hashimoto, T. Takizawa, A. Fujimori, M. Kubota, K. Ono, and H. Eisaki, Phys. Rev. B **82**, 085119 (2010).

[131] E. Pavarini, S. Biermann, A. Poteryaev, A. I. Lichtenstein, A. Georges, and O. K. Andersen, Phys. Rev. Lett. **92**, 176403 (2004).

[132] I. A. Nekrasov, K. Held, G. Keller, D. E. Kondakov, T. Pruschke, M. Kollar, O. K. Andersen, V. I. Anisimov, and D. Vollhardt, Phys. Rev. B **73**, 155112 (2006).

[133] R. Sakuma, P. Werner, and F. Aryasetiawan, Phys. Rev. B **88**, 235110 (2013).

[134] M. Rotter, M. Tegel, and D. Johrendt, Phys. Rev. Lett. **101**, 107006 (2008).

[135] M. Yi, D. H. Lu, J. G. Analytis, J.-H. Chu, S.-K. Mo, R.-H. He, R. G. Moore, X. J. Zhou, G. F. Chen, J. L. Luo, et al., Phys. Rev. B **80**, 024515 (2009).

[136] V. Brouet, P.-H. Lin, Y. Texier, J. Bobroff, A. Taleb-Ibrahimi, P. Le Fèvre, F. Bertran, M. Casula, P. Werner, S. Biermann, et al., Phys. Rev. Lett. **110**, 167002 (2013).

[137] P. Werner, E. Gull, M. Troyer, and A. J. Millis, Phys. Rev. Lett. **101**, 166405 (2008).

[138] A. Georges, L. de' Medici, and J. Mravlje, Annual Review of Condensed Matter Physics **4**, 137 (2013).

[139] H. Ding, K. Nakayama, P. Richard, S. Souma, T. Sato, T. Takahashi, M. Neupane, Y.-M. Xu, Z.-H. Pan, A. V. Fedorov, et al., Journal of Physics: Condensed Matter **23**, 135701 (2011).

[140] S. de Jong, Y. Huang, R. Huisman, F. Massee, S. Thirupathaiah, M. Gorgoi, F. Schaefers, R. Follath, J. B. Goedkoop, and M. S. Golden, Phys. Rev. B **79**, 115125 (2009).

[141] J. M. Ginder, M. G. Roe, Y. Song, R. P. McCall, J. R. Gaines, E. Ehrenfreund, and A. J. Epstein, Phys. Rev. B **37**, 7506 (1988).

[142] P. Hansmann, N. Parragh, A. Toschi, G. Sangiovanni, and K. Held, New Journal of Physics **16**, 033009 (2014).

[143] L. de' Medici, X. Wang, M. Capone, and A. J. Millis, Phys. Rev. B **80**, 054501 (2009).

[144] Z.-X. Shen, J. W. Allen, J. J. Yeh, J. S. Kang, W. Ellis, W. Spicer, I. Lindau, M. B. Maple, Y. D. Dalichaouch, M. S. Torikachvili, et al., Phys. Rev. B **36**, 8414 (1987).

[145] A. S. Sefat, D. J. Singh, R. Jin, M. A. McGuire, B. C. Sales, and D. Mandrus, Phys. Rev. B **79**, 024512 (2009).

[146] N. Xu, P. Richard, A. van Roekeghem, P. Zhang, H. Miao, W.-L. Zhang, T. Qian, M. Ferrero, A. S. Sefat, S. Biermann, et al., Phys. Rev. X **3**, 011006 (2013).

[147] van Roekeghem, Ambroise and Biermann, Silke, EPL **108**, 57003 (2014).

[148] A. Sekiyama, H. Fujiwara, S. Imada, S. Suga, H. Eisaki, S. I. Uchida, K. Takegahara, H. Harima, Y. Saitoh, I. A. Nekrasov, et al., Phys. Rev. Lett. **93**, 156402 (2004).

[149] K. Morikawa, T. Mizokawa, K. Kobayashi, A. Fujimori, H. Eisaki, S. Uchida, F. Iga, and Y. Nishihara, Phys. Rev. B **52**, 13711 (1995).

[150] O. Parcollet, G. Biroli, and G. Kotliar, Phys. Rev. Lett. **92**, 226402 (2004).

[151] J. Otsuki, Phys. Rev. B **87**, 125102 (2013).

[152] T. Ayral and O. Parcollet, Phys. Rev. B **92**, 115109 (2015).